JETP Letters, Vol. 72, No. 11, 2000, pp. 541–545. From Pis'ma v Zhurnal Éksperimental'noĭ i Teoreticheskoĭ Fiziki, Vol. 72, No. 11, 2000, pp. 785–791.

Quantum Particle Trajectories and Geometric Phase[1]

M. Dima

Department of Physics, University of Colorado, Boulder, CO-80309, USA

Received November 3, 2000

Particle trajectories are defined as integrable $dx_\mu dp^\mu = 0$ paths in projective space. Quantum states evolving on such trajectories, open or closed, do not delocalize in (x, p) projection, the phase associated with the trajectories related to the geometric (Berry) phase and the classical mechanics action. Properties at high energies of the states evolving on particle trajectories are discussed. © *2000 MAIK "Nauka/Interperiodica".*

PACS numbers: 03.65.Bz; 03.75.-b

Quantal wave-packet revival [1] is the periodic reassembly of a state's localized structure along a classically stable orbit. The phenomenon has been observed experimentally in Rydberg atoms [2], as well as in one-atom masers [3], and prompts the question whether such revival is also possible for states evolving on open trajectories [4], similarly to classical point particles. It is shown in this letter that integrable $dx_\mu dp^\mu = 0$ trajectories in projective space do provide such a context, the aspect being related to the differential geometry properties of manifolds [5], independent of the existence of a Hamiltonian.

The revival of quantal wave packets is connected to the concept of *geometric phase* [6] introduced by Berry. Berry [7] has shown that, in addition to a Hamiltonian-induced dynamic phase, a quantum state evolving in parameter space on a trajectory that returns to the initial state acquires an extra phase termed geometric phase. Subsequent analysis has generalized the context in which the phenomenon occurs, lifting the restriction of adiabaticity [8], cyclicity, and unitarity [9]. An important step was made by the kinematic approach [10], which demonstrated that the Hamiltonian is not needed in defining the geometric phase and underlined the native geometric nature of the quantity by relating it to the Bargman invariants [11, 12]. The acquirement of a geometric phase by quantum states evolving on closed trajectories in parameter space has been verified experimentally in neutron interference [13], in two-photon states produced in spontaneous parametric down-conversion [14], etc. The latter paper [14] also makes the important remark that experiments related to nonlocality vis-à-vis the Bell inequalities [15] and the Berry phase are connected, nonlocality in quantum mechanics being pointed out as a consequence of completeness as early as 1948 by Einstein [16].

The sole assumptions of this letter are that quantum systems are described by a linear representation space over $\mathbf{C}$[2] and that the coordinate operator $\mathbf{x}_\mu$ has a *conjugate operator* $[\mathbf{x}^\mu, \mathbf{k}^\nu]_- = -ig^{\mu\nu}\cdot\mathbf{1}$. The latter operators act as tangent space vectors on the manifold, and the action is revealed by the (Weyl) translation operators $\mathbf{U}_{\Delta x} \stackrel{\text{def}}{=} e^{+i\Delta x_\mu \mathbf{k}^\mu}$ and $\mathbf{U}_{\Delta k} \stackrel{\text{def}}{=} e^{-i\Delta k_\mu \mathbf{x}^\mu}$:

$$\mathbf{U}^\dagger_{\Delta x}\mathrm{x}^\mu\mathbf{U}_{\Delta x} = \mathbf{x}^\mu + \Delta x^\mu, \quad \mathbf{U}^\dagger_{\Delta k}\mathbf{k}^\mu\mathbf{U}_{\Delta k} = \mathbf{k}^\mu + \Delta k^\mu, \quad (1)$$

respectively, $|x\rangle \stackrel{\mathbf{U}_{\Delta x}}{\rightarrow} |x + \Delta x\rangle$ and $|k\rangle \stackrel{\mathbf{U}_{\Delta k}}{\rightarrow} |k + \Delta k\rangle$. Given an arbitrary reference state $|\psi_{\text{ref}}\rangle$, a set of translated image states can be defined as [17]

$$|\psi(\xi, \kappa)\rangle \stackrel{\text{def}}{=} \mathbf{U}_{\Delta k}\mathbf{U}_{\Delta x}|\psi_{\text{ref}}\rangle, \quad (2)$$

with correspondingly translated state averages

$$\begin{aligned}\langle\mathbf{x}^\mu\rangle_{\psi(\xi,\kappa)} &= \langle\mathbf{x}^\mu\rangle_{\text{ref}} + \Delta x^\mu = \xi^\mu,\\ \langle\mathbf{k}^\mu\rangle_{\psi(\xi,\kappa)} &= \langle\mathbf{k}^\mu\rangle_{\text{ref}} + \Delta k^\mu = \kappa^\mu.\end{aligned} \quad (3)$$

The spread of the image states is identical to that of the reference state, regardless the $(\Delta x, \Delta k)$ translation:

$$\begin{aligned}\delta x^\mu_{\psi(\xi,\kappa)} &= \delta x^\mu_{\text{ref}} = \text{const},\\ \delta k^\mu_{\psi(\xi,\kappa)} &= \delta k^\mu_{\text{ref}} = \text{const}.\end{aligned} \quad (4)$$

The interchange of $\mathbf{U}_{\Delta x}$ and $\mathbf{U}_{\Delta k}$ in the definition of the image state $|\psi(\xi, \kappa)\rangle$ leads to a state corresponding in

[1] This article was submitted by the author in English.

[2] To be published. In essence, it is possible to arrive at the $\mathbf{x}_\mu$ and $\mathbf{k}_\mu$ operators and their commutation relation solely on grounds related to separability of states and differential geometry properties of manifolds without prior knowledge of the physical equations.

projective space [8, 12] to the same point, the difference between the two being just a phase factor:

$$\mathbf{U}_{\Delta x}\mathbf{U}_{\Delta k} = e^{+i\Delta x_\mu \Delta k^\mu}\mathbf{U}_{\Delta k}\mathbf{U}_{\Delta x}. \quad (5)$$

The situation is revealed better by the comparison of $|\psi_{\text{ref}}\rangle$ with its transported image around the $\Delta x \longrightarrow \Delta k \longrightarrow -\Delta x \longrightarrow -\Delta k$ quantum loop

$$\mathbf{U}_{\text{loop}} = \mathbf{U}^\dagger_{\Delta k}\mathbf{U}^\dagger_{\Delta x}\mathbf{U}_{\Delta k}\mathbf{U}_{\Delta x} = e^{-i\Delta x_\mu \Delta k^\mu}\cdot\mathbf{1}, \quad (6)$$

respectively, around an arbitrary quantum loop

$$\mathbf{U}_{\text{loop}} = \prod_{\text{loop}}\mathbf{U}_{dk}\mathbf{U}_{dx} = e^{-i\oint k_\mu dx^\mu}\cdot\mathbf{1} = e^{-i\oint x_\mu dk^\mu}\cdot\mathbf{1}. \quad (7)$$

In both cases, the state acquires a geometric phase proportional to the (x, k) area enclosed by the loop in projective space. Should this phase be zero, the anholonomy [9] hold preventing the realization of a proper (x, k) coordinate system on the representation space disappears, as will be shown in the next paragraph. Generalizing Eq. (5) to continuous open paths

$$\mathbf{U}_{open} = \prod_{initial}^{final}\mathbf{U}_{dk}\mathbf{U}_{dx} = e^{-i\int_i^f k_\mu dx^\mu}\cdot\mathbf{U}_{\Delta k}\mathbf{U}_{\Delta x} \quad (8)$$

and holding the initial and final states apart at fixed displacements $(\Delta x, \Delta k)$, a path-dependent geometric phase for *open paths* can be defined, arbitrary up to a path-independent gauge [18] field $\Phi(x, k)$:

$$S \stackrel{\text{def}}{=} -\int_i^f k_\mu dx^\mu = +\int_i^f x_\mu dk^\mu. \quad (9)$$

The above relation supports a class of canonical transformations (such as $Q = k$, $K = -x$) consistent with $[\mathbf{x}^\mu, \mathbf{k}^\nu]_- = -ig^{\mu\nu}\cdot\mathbf{1}$ and $\langle x|k\rangle = (2\pi)^{-2}e^{-ix_\mu k^\mu}$ that identifies geometric phase as the classical mechanics *action* [19]. Assuming that $|\psi_{\text{ref}}\rangle$ can evolve on two neighboring paths via a beam-splitter-like mechanism, the interference in the final state is destructive unless $\delta S = 0$ (for remote trajectories $\delta S = 2n\pi$), respectively, the *extremal action condition*. Paths satisfying the extremal action condition at each point or, equivalently, in Eq. (6) $dx_\mu dk^\mu = 0$, preserve constructive interference along the path and are termed "*particle trajectories*." This is not an exclusive category, however, nonparticle *infodynamics* being equally possible[3] [20]. The early attempts to formulate quantum mechanics in terms of (x, p) coordinates failed due to the nonzero commutator of the coordinate and momentum operators $[\mathbf{x}^\mu, \mathbf{p}^\nu]_- = -i\hbar g^{\mu\nu}\cdot\mathbf{1}$ and are best summarized by the Heisenberg inequality $\delta x^\mu \cdot \delta p^\nu \geq \frac{1}{2}\hbar g^{\mu\nu}$. Nonetheless, free propagation of quantum systems can be approximated by classical mechanics, as hinted at by the extremal geometric phase relation above.

Establishing an (x, k) coordinate system on a manifold requires that a translation with a Δx leg followed by one with a Δk leg reach the same point as it would with those operations interchanged:

$$[\mathbf{U}_{\Delta x}, \mathbf{U}_{\Delta k}]_- = (1 - e^{-i\Delta x_\mu \Delta k^\mu})\mathbf{U}_{\Delta x}\mathbf{U}_{\Delta k} = 0. \quad (10)$$

This is possible nontrivially only for spaces at least 2D in dimension, by requiring $\Delta x_\mu \Delta k^\mu = 0$. The problem of establishing an (x, k) grid on a 1D manifold is that a translation around a quantum loop of area $dx \cdot dk = \frac{1}{2}$ accumulates a phase factor π, as seen from Eq. (7). For manifolds of greater dimension, this phase may vanish by *reciprocal phase compensation* among dimensions of opposite metric sign. For a Euclidian metric, it can be shown that the condition is met only by trajectories on the sphere, while for the Minkowski metric nontrivial solutions of the $n + 1$ pairs of canonically conjugate variables, (Q, K) plus the *temporal* dimension (T, H), are allowed. To have thus a proper (x, k) coordinate system on the manifold, two conditions must be met:

1. Necessary condition: $dx_\mu dk^\mu = 0|_{PATH}$.

This relation *locally* defines a coordinate system, and it is better known in physics than apparent at first glance. For example, in the case of wave-packet propagation, requiring the constituent waves to move in sync yields the condition $\mathbf{v}_g = \nabla_k\omega$, which, rewritten as $\mathbf{v}_g \cdot d\mathbf{k} = \nabla_k\omega \cdot d\mathbf{k} = d\omega$, becomes

$$dt \cdot d\omega - d\mathbf{x} \cdot d\mathbf{k} = 0. \quad (11)$$

For point particles, the work–energy relation $dE = \mathbf{F}d\mathbf{x} = d\mathbf{x} \cdot d\mathbf{p}/dt$ can likewise be rewritten as

$$dt \cdot dE - d\mathbf{x} \cdot d\mathbf{p} = 0. \quad (12)$$

2. Sufficient condition: $d^2x = 0$ and $d^2k = 0|_{PATH}$.

This relation conditions path integrability, necessary for the path-independent definition of an (x, k) coordinate system on the manifold. It is a *global* condi-

[3] An interesting discussion on the conditions to make semiclassical expansions of path integrals describe quantum systems may be found.

tion, the standard solution[4] being, up to a canonical transformation [19],

$$k_\mu k^\mu = \pm k_C^2, \quad dx^\mu/\|dx\| = k^\mu/k_C. \tag{13}$$

The traditional "dynamic" character of $\mathbf{k}_\mu$ stems precisely from this solution, and less so from its more distantly related differential geometry properties on the manifold. The inertia of the differential equations rules out "crossover" trajectories from $k_\mu k^\mu > 0$ to $k_\mu k^\mu < 0$ paths, $\pm k_C^2$ being a characteristic of the trajectory. Likewise, trajectories on the light cone cannot "fall" onto $k_\mu k^\mu > 0$ or $k_\mu k^\mu < 0$ solutions either, due to the gradient of the differential equation parallel to the sheet of the light cone. The $k_\mu k^\mu = \pm k_C^2$ relation is also well known in physics in the form of $E = c\sqrt{m_0^2 c^2 + \mathbf{p}^2}$, respectively:

$$(E/c)^2 - \mathbf{p}^2 = (m_0 c)^2. \tag{14}$$

[4] For $\|dx\| \neq 0$, the $dx_\mu dk^\mu = 0$ relation requires that dk be "perpendicular" to dx, respectively, $dk^\mu = \mathbf{C}_\perp^{\mu\nu}\omega_\nu$, where ω is an arbitrary *1-form* not "parallel" to the "unit" vector $n^\mu \stackrel{\text{def}}{=} dx^\mu/\|dx\|$ and $\mathbf{C}_\perp^{\mu\nu} = g^{\mu\nu} - n^\mu n^\nu$ is a tensor that selects the "perpendicular" component to dx^μ. To be integrable, dx and dk must be closed forms: $d^2x^\mu = 0$ and $d^2k^\mu = d\mathbf{C}_{\perp\wedge}^{\mu\nu}\omega_\nu + \mathbf{C}_\perp^{\mu\nu}d\omega_\nu = 0$, where $d\mathbf{C}_\perp^{\mu\nu} = -\mathbf{C}_\perp^{\mu\rho}dn_p n^\nu - n^\mu dn_\rho \mathbf{C}_\perp^{\rho\nu}$. The $d^2k = 0$ condition can be rewritten as

$$n^\mu(dn_{\rho\wedge}\mathbf{C}_\perp^{\rho\nu}\omega_\nu) = \mathbf{C}_\perp^{\mu\nu}(d\omega_\nu - n^p\omega_{\rho\wedge}dn_\nu). \tag{A}$$

The left-hand side proportional to n and the right-hand side "perpendicular" to n imply $\mathbf{C}_\perp^{\mu\nu}dn_{\mu\wedge}\omega_\nu = 0$, a condition that has the following solutions: (i) $\mathbf{C}_\perp^{\mu\nu}\omega_\nu = 0$, (ii) $\mathbf{C}_\perp^{\mu\nu}dn_\mu = 0$, and (iii) $dn_{\mu\wedge}\omega_\nu$ = *antisymmetric*. Solution (i) is equivalent to $dk = 0$, solution (ii) restricts dn "parallel" to n—impossible in view of $n_\mu n^\mu = \pm 1$; thus, the only viable solution is (iii), $\omega_\nu = k_C \cdot dn_\nu$ where k_C is a scalar field. From the right-hand side of Eq. (A) equal to zero and the arbitrary orientation of dn with respect to n, the scalar field $\Lambda_C = 2\pi/k_C$ must be a constant (known as the "Compton wavelength"). Therefore, $dk^\mu = k_C \cdot \mathbf{C}_\perp^{\mu\nu}dn_\nu$, or in view of $n_\mu n^\mu = \pm 1$, $dk^\mu = k_C dn^\mu$ and $k^\mu = k_C n^\mu + (\text{const})^\mu$. In the eigensystem of reference of the trajectory, the $dx_\mu dk^\mu = 0$ condition is simply $dk'_0 = 0$. Requiring Lorentz invariance, the constant in the solution above must be zero and

$$k^\mu = k_C \cdot n^\mu = k_C \cdot \frac{dx^\mu}{d(c\tau)},$$

where τ is the invariant proper time, $(cd\tau)^2 = \pm dx_\mu dx^\mu$. In the track's eigensystem of reference $k'_\mu = \pm(k_C, 0)$, and in the laboratory system of reference $k_\mu k^\mu = \pm k_C^2$. The "photonic" case $\|dx\| = 0$ yields $k_\mu k^\mu = 0$. Both in this and in the $\|dx\| \neq 0$ case, the solution holds up to a canonical transformation [19].

In summary, up to a canonical transformation [19], particle trajectories provide a ruling of the manifold that satisfies the

translational properties of state averages

$$\begin{aligned}\langle \mathbf{x}^\mu\rangle_{\psi(\xi,\kappa)} &= \langle \mathbf{x}^\mu\rangle_{\text{ref}} + \Delta x^\mu,\\ \langle \mathbf{k}^\mu\rangle_{\psi(\xi,\kappa)} &= \langle \mathbf{k}^\mu\rangle_{\text{ref}} + \Delta k^\mu;\end{aligned} \tag{15}$$

spreadless transport of states:

$$\begin{aligned}\delta x^\mu_{\psi(\xi,\kappa)} &= \delta x^\mu_{\text{ref}} = \text{const},\\ \delta k^\mu_{\psi(\xi,\kappa)} &= \delta k^\mu_{\text{ref}} = \text{const};\end{aligned} \tag{16}$$

x–k evolution[5] equations

$$\begin{aligned} d\langle \mathbf{x}^\mu\rangle/\|d\langle \mathbf{x}\rangle\| &= \langle \mathbf{k}^\mu\rangle/k_C,\\ d\langle \mathbf{x}^\mu\rangle d\langle \mathbf{k}_\mu\rangle &= 0,\\ \int_{path}\langle \mathbf{k}_\mu\rangle d\langle \mathbf{x}^\mu\rangle &= extremal;\end{aligned} \tag{17}$$

path-type constraints

$$\begin{aligned}\langle \mathbf{k}_\mu\rangle\langle \mathbf{k}^\mu\rangle &= \pm k_C^2,\\ \langle \mathbf{k}_\mu \mathbf{k}^\mu\rangle &= \pm k_C^2 - \delta k_\mu \delta k^\mu;\end{aligned} \tag{18}$$

contact condition between the physically meaningful state averages and the particle trajectory ruling of the manifold

$$\begin{aligned}\langle \mathbf{x}^\mu\rangle_{\psi(\xi,\kappa)} &= \xi^\mu,\\ \langle \mathbf{k}^\mu\rangle_{\psi(\xi,\kappa)} &= \kappa^\mu.\end{aligned} \tag{19}$$

Although no physical interpretation has been assumed so far for $\mathbf{k}$, it is evident that it corresponds to what is more traditionally known as 4-momentum, $\mathbf{p}_\mu = \hbar\mathbf{k}_\mu$.

Since geometric-phase properties have been discussed mostly in the context of low-energy phenomena, the following will refer to high-energy aspects. Quantum states traveling on particle trajectories $\langle \mathbf{k}_\mu\rangle\langle \mathbf{k}^\mu\rangle$ = const have two constants of motion:

$$\begin{aligned} m_0^2 &\stackrel{\text{def}}{=} \frac{\hbar^2}{c^2}\langle \mathbf{k}_\mu\rangle\langle \mathbf{k}^\mu\rangle,\\ m_{bare}^2 &\stackrel{\text{def}}{=} \frac{\hbar^2}{c^2}\langle \mathbf{k}_\mu \mathbf{k}^\mu\rangle,\end{aligned} \tag{20}$$

[5] Similar to the Ehrenfest theorems, based, however, on differential geometry properties of manifolds, rather than being a consequence of evolution equations (i.e., Schrödinger).

the *rest* and *bare* mass of the state, related to each other by the spread of the state in k space,

$$m_{bare}^2 - m_0^2 = \frac{\hbar^2}{c^2}\delta k_\mu \delta k^\mu, \tag{21}$$

a difference that for most stable systems is negative. The spread of m_{bare}^2 for an evolving quantum state is

$$\begin{aligned}\langle \delta^2(\mathbf{k}_\mu \mathbf{k}^\mu)\rangle_{\psi(\xi,\kappa)} &= \langle \delta^2(\mathbf{k}_\mu \mathbf{k}^\mu)\rangle_{\mathrm{ref}} \\ &+ 4\|\Delta k\| \cdot \langle \delta(\mathbf{k}_\mu \mathbf{k}^\mu)\delta(n_\mu \mathbf{k}^\mu)\rangle_{\mathrm{ref}} \\ &+ 4\|\Delta k\|^2 \cdot \langle \delta^2(n_\mu \mathbf{k}^\mu)\rangle_{\mathrm{ref}},\end{aligned} \tag{22}$$

where $\|\Delta k\| \stackrel{\mathrm{def}}{=} |\Delta k_\mu \Delta k^\mu|^{1/2}$ and $n_\mu = \Delta k_\mu / \|\Delta k\|$. Due to the minimum of the expression in the vicinity of $(\pm m_0 c^2, 0)$ for subluminous and $(0, \pm m_0 c)$ for supraluminous trajectories, the linear term in $\|\Delta k\|$ vanishes and the Klein–Gordon equation holds with good approximation:

$$\mathbf{k}_\mu \mathbf{k}^\mu \simeq \mathrm{const} \cdot \mathbf{1}. \tag{23}$$

For high boost factors $\gamma \longrightarrow \infty$, however, the spread in m_{bare}^2 diverges even if $\Delta m_{bare}^{ref} = 0$, the Klein–Gordon equation losing accuracy:

$$\frac{\Delta m_{bare}}{m_{bare}} \simeq \frac{\hbar\sqrt{2\gamma}}{m_{bare} c}\sqrt{\langle \delta^2(\mathbf{k}_0 - \mathbf{k}_\parallel)\rangle_{\min}} \tag{24}$$

as the state approaches the light cone and overlaps with the densely bunched m_{bare}^2 paths in this region of k space, as well as with the supraluminous states across the light cone. This should be distinguished from seeing the state from a different system of reference (Lorentz boost). The $\Delta m_{bare}/m_{bare}$ magnitude of the effect is on the order of 0.2% for a 1 eV/c-wide e^- state accelerated to LEP2 energies, respectively, 4% for a 1 MeV/c-wide p state accelerated to TEVatron energies. At $E \simeq 300$ GeV, a generic 1 eV/c-wide e^- state overlaps with hypothetical supraluminous[6] components of m_{bare} as high as 0.7 GeV/c^2.

In summary, $dx_\mu dk^\mu = 0$ integrable trajectories have been shown to transport quantum states nondispersively in (x, k) projective space. The geometric phase associated with the trajectories is extremal, its expression being that of the classical mechanics action. The trajectories are described by a constant of motion $k_\mu k^\mu = k_C^2$, more traditionally known as the "rest mass" m_0^2. Highly boosted quantum states overlap both with higher m_{bare}^2 and negative m_{bare}^2 states.

I am thankful for the hospitality during completion of this work to the High Energy Physics group of the Wuppertal University under an Alexander von Humboldt Foundation grant, and to the Physics Department of the University of Colorado at Boulder.

REFERENCES

1. C. Jarzynski, Phys. Rev. Lett. **74**, 1264 (1995); G. G. de Polavieja, Phys. Rev. Lett. **81**, 1 (1998).
2. M. Nauenberg, C. Stroud, and J. Yeazell, Sci. Am. **270**, 44 (1994).
3. G. Rempe, H. Walther, and N. Klein, Phys. Rev. Lett. **58**, 353 (1987).
4. D. C. Brody and L. P. Hughston, quant-ph/9906086; A. K. Pati, Ann. Phys. **270**, 178 (1998).
5. S. Kobayashi and K. Nomizu, *Foundations of Differential Geometry* (Wiley, New York, 1963).
6. *Geometric Phases in Physics*, Ed. by A. Shapere and F. Wilczek (World Scientific, Singapore, 1989); S. I. Vinitsky, V. L. Dubovik, B. L. Markovski, and Yu. P. Stepanaski, Usp. Fiz. Nauk **160** (6), 1 (1990) [Sov. Phys. Usp. **33**, 403 (1990)].
7. M. V. Berry, Proc. R. Soc. London, Ser. A **392**, 45 (1984); L. van Hove, Bull. Cl. Sci., Acad. R. Belg. **37**, 610 (1951).
8. Y. Aharonov and J. Anandan, Phys. Rev. Lett. **58**, 1593 (1987).
9. J. Samuel and R. Bhandari, Phys. Rev. Lett. **60**, 2339 (1988).
10. N. Mukunda and R. Simon, Ann. Phys. (N.Y.) **228**, 205 (1993); **228**, 269 (1993).
11. V. Bargman, J. Math. Phys. **5**, 862 (1964).
12. E. M. Rabei, Arvind, N. Mukunda, and R. Simon, Phys. Rev. A **60**, 3397 (1999).
13. B. E. Allman, H. Kaiser, S. A. Werner, A. G. Wagh, V. C. Rakhecha, and J. Summhammer, Phys. Rev. A **56**, 4420 (1997).
14. D. V. Strekalov and Y. H. Shih, Phys. Rev. A **56**, 3129 (1997).
15. S. F. Huelga, T. W. Marshall, and E. Santos, Europhys. Lett. **38**, 249 (1997); S. L. Braunstein, A. Mann, and M. Revzen, Phys. Rev. Lett. **68**, 3259 (1992).
16. A. Einstein, Dialectica **2**, 320 (1948).

[6] Hypothetical supraluminous transformations connect transformations across the light cone, changing the sign of the pseudonorm. This type of action interchanges temporal with spatial information parallel to the direction of boost, while rendering arbitrary information perpendicular to it. Supraluminous transformations would hence obey $\Lambda^\dagger G \Lambda = -C_\parallel G$ and have the form

$$\Lambda_\nu^{\cdot\mu} = \gamma' \begin{pmatrix} 1 & \boldsymbol{\beta} \\ \boldsymbol{\beta} & \mathbf{C}_\parallel \end{pmatrix},$$

where $\gamma' = 1/\sqrt{\beta^2 - 1}$ and $C_\parallel$ is a tensor selecting the parallel component to the boost.

17. J. R. Klauder, J. Math. Phys. **4**, 1055 (1963); **4**, 1058 (1963); A. Premolov, Commun. Math. Phys. **26**, 22 (1972); A. Premolov, *Generalized Coherent States* (Springer-Verlag, Berlin, 1986); A. A. Kirilov, *Elements of the Theory of Representations* (Springer-Verlag, Berlin, 1976); B. Konstant, in *Lectures in Modern Analysis and Applications III*, Ed. by C. T. Taam (Springer-Verlag, Berlin, 1970), Lect. Notes Math. **170** (1970); B. Konstant, in *Group Representations in Mathematics and Physics*, Ed. by V. Bargmann (Springer-Verlag, Berlin, 1970), Lect. Notes Phys. **6** (1970).
18. Ta-Pei Cheng and Ling-Fong Li, *Gauge Theory of Elementary Particle Physics* (Oxford Univ. Press, Oxford, 1988).
19. V. I. Arnold, *Mathematical Methods of Classical Mechanics* (Springer-Verlag, New York, 1978).
20. M. Stone, quant-ph/0006020; cond-mat/0004247; J. Wei and E. Norman, J. Math. Phys. **4**, 575 (1963).

JETP Letters, Vol. 72, No. 11, 2000, pp. 546–549. Translated from Pis'ma v Zhurnal Éksperimental'noĭ i Teoreticheskoĭ Fiziki, Vol. 72, No. 11, 2000, pp. 792–796.

Near-Field Effect in Thermal Radio-Frequency Radiation

K. P. Gaĭkovich and A. N. Reznik

Institute for Physics of Microstructures, Russian Academy of Sciences, Nizhni Novgorod, 603600 Russia

Received August 24, 2000; in final form, October 31, 2000

The near-field effect was experimentally observed in the thermal radiation of an absorbing medium in the rf range. The radiation from a temperature-stratified aqueous medium was measured at a wavelength of 31 cm using specially developed electrically small antennas. The effect manifests itself as a decrease in the effective thickness of a layer in which the received radiation is formed and in the dependence of this thickness on the receiving antenna's size and its height above the medium surface. © *2000 MAIK "Nauka/Interperiodica".*

PACS numbers: 44.40.+a; 41.20.Jb

The near (quasistationary) field of thermal electromagnetic radiation from heated media was predicted by S.M. Rytov as a consequence of his electrodynamic theory of equilibrium thermal fluctuations as early as the 1950s [1]. This field is characterized by the absence of energy flux and by a sharp drop in the volume energy density with distance from the surface of the radiating medium. It was theoretically proved in [2] that the near-field component of thermal radiation tangibly affects the signal intensity measured by a receiver only if the receiving antenna has small electric size $D \ll \lambda$ (λ is the wavelength) and is situated at height $h \ll \lambda$ above the radiating surface. These features hamper experimental investigations, for which reason the near-field component of thermal radiation has not been experimentally detected so far.

As a result of the near-field effect, the effective thickness of a layer forming the received radiation decreases compared to the skin layer. The decrease in the effective thickness can be observed experimentally as a function of either the antenna's size (near the surface) or its height (for a small antenna). This was precisely the way in which the near-field component of thermal radiation was detected in this study by the measurements at a fixed wavelength.

Investigations were carried out in the decimeter wavelength range (λ = 31 cm). The obvious advantage of decimeter waves over the shorter radio and infrared waves is that they place substantially less stringent requirements on the antenna's size and its height above the surface, because these parameters are specified by the wavelength scale and lie in the interval D/λ, $h/\lambda <$ 0.1 [2]. The thermal radiation was detected by a radiometer with operating frequency f_0 = 950 GHz, frequency band Δf = 250 MHz, and fluctuation sensitivity threshold $\delta_T \approx 0.05$ K at the integration constant τ = 1 s.

The key element of the receiving system was an electrically small antenna of size D = 1 cm ($D/\lambda \approx$ 0.03). It consisted of two in-phase dipoles connected to a symmetric strip line operating as a matching cavity (a prototype of this system is described in [3]). When the antenna was in contact with the medium (h = 0), it was matched to the radiometer input so that the reflection coefficient averaged over the radiometer band Δf did not exceed 0.03. The radiation efficiency was determined from a comparison of the data of calibration measurements at two different temperatures of a uniformly heated medium with the response to the radiation of a matched load and was found to be η = 0.85 at h = 0. An increase in height led to both antenna mismatch (increase in the reflection coefficient) and decrease in the radiation efficiency. The sensitivity threshold to the temperature variations increased from 0.06 K at h = 0 to 1 K at the maximum height of measurements h_{max} = 2.5 mm. Further decrease in sensitivity at $h > h_{max}$ rendered the measurements at greater heights impossible. Thus, the presence of a matched high-efficiency antenna is a fundamental requirement for a near-field radiometric system, in contrast to similar active-location systems, which are usually referred to as near-field microscopes (see, e.g., [4]). Besides the antenna described above, the measurements were also carried out using a standard contact antenna with aperture D = 4 cm, which was developed for medico-biological radiometric investigations [5].

Water was chosen as a medium for investigation because its complex dielectric constant $\epsilon = \epsilon_1 + i\epsilon_2$ and, hence, the skin depth $d = 1/\gamma$ [$\gamma = (4\pi/\lambda)\mathrm{Im}(\sqrt{\epsilon})$ is the absorption coefficient] can be calculated with a high accuracy, e.g., from data [6], if the temperature T and the salinity S are known. Strong dependence of the skin depth on the salinity enables one to model the conditions in various media by varying the d value in the interval from 1 mm to 10 cm. In addition, it is comparatively easy to carry out contact measurements of the

0021-3640/00/7211-0546$20.00

temperature depth profile $T(z)$ in a fluid. For measurements, a stable quasi-linear profile $T(z)$ was formed with the use of a heater near the surface and a cooler near the bottom of a cylindrical vessel. The stationary temperature gradient was as large as $dT/dz \approx 2.5$ K/cm. The radiometer measured the effective temperature (antenna temperature) of the radiation received from the medium filling the $z \le 0$ half-space:

$$T_a(h, D) = \int_{-\infty}^{0} T(z)K(h, D, z)dz, \quad (1)$$

i.e., the measured antenna temperature was a certain weighted mean temperature of the medium. The kernel of integral Eq. (1) is normalized and includes two components:

$$K(z, h, D) = \frac{(K_1(z, D) + K_2(z, h, D))}{\int_{-\infty}^{0} [K_1(z, D) + K_2(z, h, D)]dz}, \quad (2)$$

where K_1 and K_2 are the contributions of the wave and quasistationary field components, respectively. The functions $K_{1,2}$ for a medium with a dielectric constant uniform in depth, i.e., $\epsilon(z) = \epsilon = \text{const}$, are given in [2]. For a uniformly heated medium [$T(z) = T_0 = \text{const}$], Eqs. (1) and (2) yield $T_a = T_0$ independently of the form of kernel K. If the distribution $T(z)$ is nonuniform in depth, the T_a value is determined by the effective thickness d_{eff} of a layer in which the received radiation is formed and which is of interest to us. This thickness is expressed through the kernel K as

$$d_{\text{eff}} = \int_{-\infty}^{0} zK(h, D, z)dz. \quad (3)$$

The wave component of radiation in free space is formed by plane nonuniform waves propagating under the surface of an absorbing medium within a certain cone with axis directed along z. If the dielectric constant satisfies the conditions $\epsilon_1 \approx \epsilon_2$ and $|\epsilon| \gg 1$ (as is the case of the aqueous medium under consideration), the apex angle of this cone is small. One then has $d_{\text{eff}} \approx d$ for the wave component of the field. Since the waves propagating in an absorbing medium at angles beyond this cone make a contribution in free space only to the near-field component of the received radiation, one has $d_{\text{eff}} < d$ for this component. Thus, for the received radiation including both field components, the condition $d_{\text{eff}} < d$ will also be fulfilled and the effective thickness will be a function of the antenna height and size, i.e., $d_{\text{eff}} = d_{\text{eff}}(h, D)$. In the case that the near-field effect on the received radiation is negligible, i.e., with an increase in the height or size of the antenna, the kernel of Eq. (1) tends to its limiting form $K(z, h, D) \longrightarrow K = \gamma\exp(z/d)$, which is independent of h and D, and one has $d_{\text{eff}} \longrightarrow d$.

According to definition (3), Eq. (1) leads to a simple exact expression for a linear profile $T(z)$,

$$T_a = T(z = -d_{\text{eff}}), \quad (4)$$

which was used in this work for determining the d_{eff} value from the data of T_a measurements.

The antenna temperature T_a was measured for each height h and antenna size D using two calibrations against the thermal radiation of two identical vessels with water uniformly heated to temperatures T_1 and T_2. In this case,

$$T_a = T_1 + \frac{(n_a - n_1)}{(n_2 - n_1)}(T_2 - T_1), \quad (5)$$

where the readings n_a and $n_{1,2}$ of a radiometer detecting device correspond to the basic and calibration measurements, respectively. The error in determining the antenna temperature with inclusion of all factors (fluctuation sensitivity, time of averaging, and errors of measuring the temperature of the standards) was equal to 0.2 K at $h = 0$ and 0.5 K at $h = 2.5$ mm. For the temperature gradient of 2.5 K/cm, the corresponding error in determining d_{eff} varied approximately from 1 to 2 mm in this height interval.

Experiments were carried out at three different values of S: 0, 1.8×10^{-3}, and 5.0×10^{-3} g/cm^3 of water salinity. The $d_{\text{eff}}(h)$ dependences measured at $S = 1.8 \times 10^{-3}$ g/cm^3 for antennas with $D = 1$ and 4 cm are shown in Fig.1 together with the results calculated by theory [2]. For this S value, the dielectric constant ϵ of water is virtually independent of temperature and it was then that the agreement between the calculations and measurements was the best. The fact is that the real part of the complex dielectric constant of water depends only slightly on temperature, so that the temperature dependence of the skin depth is primarily determined by the imaginary part of ϵ. As the ion conductivity increases with increasing salinity, the temperature dependence typical of dielectrics is transformed to the dependence typical of conductors; i.e., a decrease in $\text{Im}(\epsilon)$ with increasing temperature is transformed to its increase. At the transition point corresponding to a salinity of about $S = 1.8 \times 10^{-3}$ g/cm^3, the temperature dependence is virtually absent. In this case, the approximation of a dielectrically uniform medium [2] provides the best description of the actual situation. For other S values, the temperature dependence of the dielectric constant ϵ of water becomes appreciable. Nevertheless, even in these cases, the agreement between the calculations and the experiment is quite satisfactory if one assumes $\epsilon = \epsilon(T = T_a)$ in the theory of radiation of a dielectrically uniform medium. It is seen that the data of measurements presented in Fig. 1 agree well with the calculations by Eq. (3), while the theoretically predicted dependences of d_{eff} on antenna's height and size actually take place.

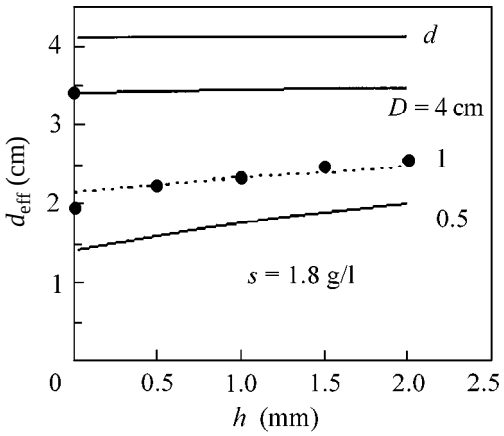

Fig. 1. Effective thickness of the radiating layer vs. antenna height for different aperture sizes. The circles and lines are the measurements and the calculations, respectively.

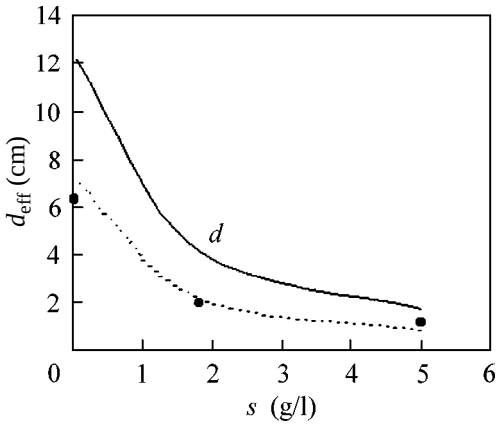

Fig. 2. (Circles) experimental and (dotted line) theoretical effective thicknesses of the formation of received radiation vs. water salinity. Solid line is the calculated skin depth as a function of *S*.

The dependences of the effective thickness d_{eff} on the water salinity *S*, as calculated and measured at $h = 0$ with the antenna of diameter $D = 1$ cm, are shown in Fig. 2 together with the calculated $d(S)$ dependence. The observed difference between d_{eff} and d (the effective thickness is about half the skin depth), proved to be very close to the theoretical value and clearly demonstrates the near-field effect, because, as mentioned above, $d_{eff} \approx d$ for the field wave component. It is also seen that the difference between d_{eff} and d is maximum for fresh water. For this reason, the dependence $d_{eff}(h)$ at $S = 0$ is more pronounced than in Fig. 1. In particular, the maximum increase in d_{eff} for fresh water exceeds 7 mm in the height interval considered.

Thus, the results presented in Figs. 1 and 2 testify to the presence of the near-field component in the thermal radiation of medium.

In conclusion, note that further development of these investigations may be associated with increasing the sensitivity of the radiometric system at heights $h > h_{max}$ (in this study, $h_{max} = 2.5$ mm) and decreasing the antenna's size (in the range $D < 1$ cm). To this end, the antenna should be matched for each height, which is not a difficult problem. At the same time, the efficiency of the electrically small antennas inevitably decreases with increasing *h*. Indeed, high radiation efficiency near the surface was ensured by the influence of the absorbing medium on the antenna characteristics, but this influence weakens with increasing *h*. A decrease in the efficiency with decreasing D/λ is a property of electrically small antennas and is caused by the influence of the ohmic losses in matching circuits.

A possible solution to this problem might be the use of materials with extremely low ohmic losses such as high-temperature superconductors. The effectiveness of using these materials in the miniaturization of antenna devices was examined in [7–9]. Our preliminary calculations show that the near-field radiometric measurements can be accomplished, at least in the height interval $0 \le h \le 0.1\lambda$ and for the antenna sizes $D/\lambda \ge 0.01$. In this case, the effective depth of the radiating layer will vary in the range $0.2d \le d_{eff} \le d$. The effect considered in this study can then be used to develop new methods of the radiothermal diagnostics of media. In particular, the single-wave methods proposed in [2, 10] for determining the subsurface temperature profile $T(z)$ by solving integral Eq. (1) with the use of the measured dependence of the antenna temperature T_a on the antenna's size and height above the surface may be realized. These methods may become simpler in implementation than the known multifrequency methods [11–15].

In summary, the presence of a near electromagnetic field in the thermal radiation of an absorbing medium is experimentally demonstrated in this work. The development of near-field radiometry will allow one to devise new methods for medium diagnostics.

We are grateful to V.L. Vaks for assistance. This work was supported by the Russian State Scientific–Engineering Program "Physics of Condensed Matter," state contract no. 107-3 (00-II).

REFERENCES

1. S. M. Rytov, *Theory of Electrical Fluctuations and Heat Emission* (Akad. Nauk SSSR, Moscow, 1953).
2. A. N. Reznik, Izv. Vyssh. Uchebn. Zaved., Radiofiz. **34**, 512 (1991).
3. V. I. Abramov and A. N. Reznik, Izv. Vyssh. Uchebn. Zaved., Radiofiz. **42**, 158 (1999).
4. E. A. Ash and G. Nicholls, Nature **237**, 510 (1972).
5. V. S. Troitskiĭ, I. F. Belov, and V. P. Gorbachev, Usp. Fiz. Nauk **134**, 155 (1981) [Sov. Phys. Usp. **24**, 430 (1981)].

6. L. A. Klein and C. T. Swift, IEEE Trans. Antennas Propag. **25**, 104 (1977).
7. H. Chaloupka, N. Klein, M. Peiniger, *et al.*, IEEE Trans. Microwave Theory Tech. **39**, 1513 (1991).
8. A. Yu. Klimov, Z. F. Krasil'nik, A. N. Reznik, *et al.*, Sverkhprovodimost: Fiz., Khim., Tekh. **6**, 2150 (1993).
9. V. I. Abramov, A. Yu. Klimov, A. N. Reznik, and B. B. Tagunov, Pis'ma Zh. Tekh. Fiz. **20** (19), 60 (1994) [Tech. Phys. Lett. **20**, 792 (1994)].
10. K. P. Gaikovich and A. N. Reznik, in *Proceedings of 8th International Conference on Microwave and Telecommunication Technology, Crimea, Ukraine, 1998* (Veber, Sevastopol, 1998), Vol. 2, p. 629.
11. F. Bardaty and D. Solimini, Radio Sci. **18**, 1393 (1983).
12. I. Leroy, B. Bocquet, and A. Mamouni, Physiol. Meas. **19**, 127 (1998).
13. K. P. Gaĭkovich, A. N. Reznik, M. I. Sumin, and R. V. Troitskiĭ, Izv. Akad. Nauk SSSR, Fiz. Atmos. Okeana **23**, 761 (1987).
14. K. P. Gaĭkovich, M. I. Sumin, and R. V. Troitskiĭ, Izv. Vyssh. Uchebn. Zaved., Radiofiz. **31**, 1104 (1988).
15. K. P. Gaĭkovich, A. N. Reznik, and R. V. Troitskiĭ, Izv. Vyssh. Uchebn. Zaved., Radiofiz. **33**, 1467 (1989).

Translated by R. Tyapaev

JETP Letters, Vol. 72, No. 11, 2000, pp. 550–552. Translated from Pis'ma v Zhurnal Éksperimental'noĭ i Teoreticheskoĭ Fiziki, Vol. 72, No. 11, 2000, pp. 797–801.

Anomalous Magnetism of La_2CuO_{4+x} Single Crystals

A. A. Nikonov and O. E. Parfenov

Russian Research Center Kurchatov Institute, pl. Kurchatova 1, Moscow, 123182 Russia

e-mail: nikonov@isssph.kiae.ru

Received October 19, 2000

Measurements of the differential magnetic susceptibility are performed to study the changes in the magnetic properties of La_2CuO_{4+x} due to oxygen doping in the concentration interval $0 < x < 0.011$. For crystals with $0.005 < x < 0.011$, a ferromagnetic-type phase transition is observed at $T_c > T_N$, and it occurs even in crystals with $T_N \sim 0$. The concentration dependence of the transition temperature $T_c(x)$ is obtained. © *2000 MAIK "Nauka/Interperiodica".*

PACS numbers: 75.30.Cr; 74.72.Dn; 75.25.+z

Among the unsolved problems of high-T_c superconductivity, the following issues attract particular attention of researchers: the mechanism of destruction of the antiferromagnetic (AFM) order with an increase in hole concentration, the nature of strong magnetic fluctuations in the region of phase diagram where the insulator–metal transition takes place, and the role of these fluctuations in the initiation of superconductivity.

To investigate these problems, we earlier carried out comprehensive studies of weakly oxygen-doped La_2CuO_{4+x} single crystals [1, 2]. A new result consisted in the observation of an unusual divergence in the temperature dependence of the differential magnetic susceptibility $\chi_c(T)$ in the critical region of the antiferromagnetic transition. The divergence was observed only for the transverse magnetic susceptibility χ_c and only in low magnetic fields. As the magnetic field increased to $H_c \sim 100$ Oe, the divergence gradually disappeared. Such behavior of the magnetic susceptibility is characteristic of the magnetic phase transition in an antiferromagnet with weak ferromagnetism (WFM) [3]. However, the unit cell of the *Bmab* orthorhombic crystal lattice of La_2CuO_4 does not coincide with the magnetic unit cell of the AFM lattice. In such a situation, the theory of symmetry forbids the existence of WFM in zero magnetic field [4]. At the same time, the appearance of a WFM becomes possible in a strong magnetic field $H \sim 2$ T applied along the crystal *c* axis [5] because of the spin flip in a part of the AFM lattice. In this case, owing to the field-induced change in the symmetry of the magnetic lattice, the WFM becomes allowed.

In studying the possible correlation between the magnetic and structural properties of La_2CuO_{4+x} [2], we showed that the anomalous divergence appeared only after the introduction of excess oxygen. In addition, the height of the ferromagnetic anomaly of susceptibility was found to correlate with the degree of orthorhombic distortion of the crystal lattice and with the kinetics of the oxygen ordering processes. The height of the ferromagnetic peak was related to the average magnetic moment and the magnetic correlation length. The ordering contributed to the increase in the divergence. It should be noted that we revealed the traces of the superstructure in the crystal lattice. The symmetry of the crystal lattice of our oxygen-doped crystals presumably differed from the symmetry of a simple *Bmab* orthorhombic lattice of stoichiometric La_2CuO_4.

It is possible that the appearance of the ferromagnetic moment in the AFM state of La_2CuO_{4+x} was a result of the symmetry change caused by the distortion of the crystal, rather than magnetic, lattice. At the same time, to change the crystal symmetry, the distortion of the crystal lattice must be coherent of the superstructure type, rather than of a local character. This situation is of special interest, because the introduction of the impurity leads not only to the appearance of a new magnetic state, but also to rapid destruction of the AFM lattice. Therefore, as the three-dimensional AFM order breaks, the roles of the magnetic order and the crystal distortions in the mechanism of formation of the new magnetic state can change.

The aim of the experiments described in this paper was to study the behavior of the previously observed [2] unusual weak ferromagnetism of La_2CuO_4 single crystals in the course of a gradual destruction of the antiferromagnetic order that occurs with an increase in the level of oxygen doping.

We studied single crystals grown by the molten solution method [6]. The characteristic feature of these crystals is the low mobility of the excess oxygen [2], which ensures the absence of a "macroscopic" phase separation into phases with different oxygen concentrations in the interval $0 < x < 0.03$ [1, 7]. The structure of the phase diagram of these crystals [1] is analogous to that of the $La_{2-y}Sr_yCuO_4$ system. The temperature and concentration dependences of the AFM and SG mag-

0021-3640/00/7211-0550$20.00

netic phase transitions, which were obtained in this study using the magnetic field H = 450 Oe, correlate well with the data for the $La_{2-y}Sr_yCuO_4$ crystals [8] in which the magnetism was studied using the magnetic field H = 5 kOe.

The grown crystals had the AFM ordering temperature $T_N \sim 245$ K. To avoid the inclusion of excess oxygen lattice vacancies, annealing at a partial oxygen pressure < 100 Torr was carried out at a temperature not exceeding 700°C. Oxygen was introduced at a temperature of 900°C under excess oxygen pressure of up to 10 atm. The magnetic properties were studied by measuring the differential magnetic susceptibility in a weak alternating field $h = h_0\sin(wt)$, where h_0 = 1 Oe and f = 1 kHz. A detailed description of the measuring technique can be found in [9]. Using the Vegard law for small deviations from the stoichiometry [10], we determined the excess oxygen concentration x by the formula $c = 13.137 + 1.065x$, where c is the lattice parameter measured by X-ray structural analysis.

Figure 1 shows the changes that occur in the $\chi_c(T)$ dependence with varying oxygen concentration. The dependences $\chi_c(T)$ were measured in both zero constant external field and a field H = 450 Oe applied along the c axis of the crystal. In the concentration interval $0 < x < 0.011$, the formation of a new magnetic state has the form of a phase transition with a pronounced anisotropy, and the ferromagnetic anomaly is observed only for the transverse susceptibility $\chi_c(T)$ and only in the fields H < 100 Oe. Although an increase in the excess oxygen concentration is accompanied by a decrease in both critical temperature T_c and divergence intensity, the critical region of the revealed magnetic transition spreads insignificantly. The width of the temperature interval corresponding to the critical region does not exceed 20 K, indicating a good spatial homogeneity of the magnetic system. Another specific feature of the susceptibility anomaly is the almost symmetric form of the peak. The values of the critical indices of the transition, which are determined by the formulas $\chi_c = \tau^{-\gamma}$ and $\chi_c = h^{-\alpha}$, are as follows (in the concentration interval $0.005 < x < 0.011$): $\gamma = 1.9 + 0.2$ and $\alpha = 0.8 + 0.2$. These values agree well with the critical indices of the two-dimensional Ising model [11].

One of the most important new results obtained from our study is that the long-range AFM order breaks with increasing x faster than T_c decreases (Fig. 2). Moreover, the new phase transition is observed in samples with $T_N \sim 0$ exhibiting a paramagnetic state or a two-dimensional spin liquid state at $T \gg T_N$ and a spin glass state at low temperatures, the latter state being detected by the characteristic behavior of the magnetic susceptibility $\chi(T)$. In the field H = 450 Oe, the dependences $\chi_c(T)$ and $\chi_{ab}(T)$ obtained for crystals with $T_N \sim 0$ exhibited no traces of the antiferromagnetic transition in the critical region of the ferromagnetic anomaly within the sensitivity of our measuring system. These

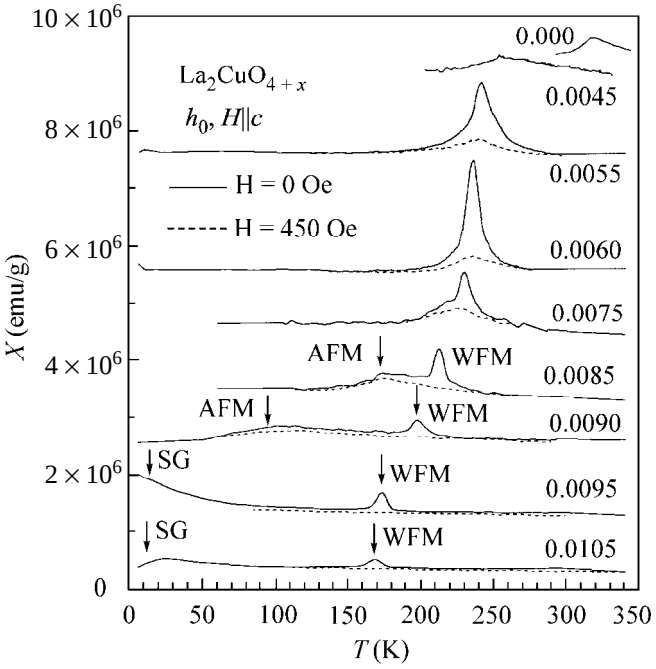

Fig. 1. Changes in the transverse magnetic susceptibility of La_2CuO_{4+x} single crystals upon oxygen doping. The numbers indicate the excess oxygen concentration x. For convenience, the curves are vertically shifted without changing scale. To obtain the true picture, one has to reduce the value of the susceptibility at 350 K to the value 3×10^{-7} CGSM/g.

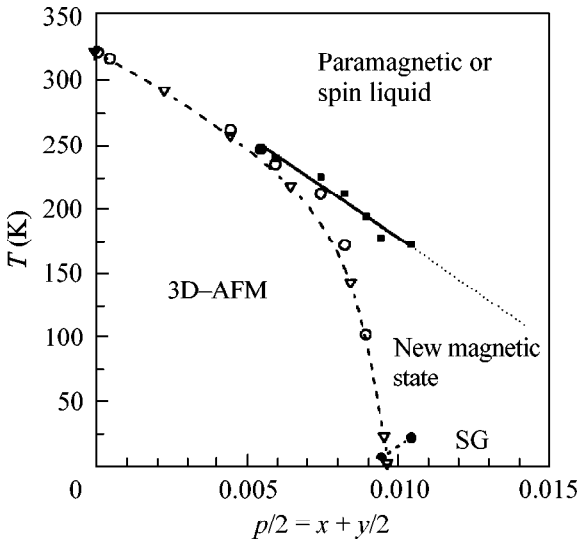

Fig. 2. Phase diagram of La_2CuO_{4+x} single crystals: T_c for the new magnetic transition is shown by the full squares, T_N for the AFM ordering is shown by the empty circles, and SG corresponds to the full circles. In addition, the data on the AFM transition reported in [8] for $La_{2-y}Sr_yCuO_4$ single crystals are presented (triangles).

data suggest that, at least in the concentration interval $0.008 < x < 0.011$, the presence of the long-range AFM order plays no crucial role in the magnetism revealed in La_2CuO_{4+x}. Hence, in the aforementioned concentra-

tion interval, the anomaly observed in $\chi_c(T)$ can be interpreted neither as the WFM resulting from weak noncollinearity of spins in the AFM lattice nor as the ferrimagnetism resulting from the decompensation of the magnetic sublattices. In view of the high value $T_c >$ 150 K, one should reject the variant with a ferromagnetic-type transition in the paramagnetic matrix because of the dipole–dipole interaction in the system of ferromagnetic clusters consisting of ordered copper spins. Otherwise, one must assume that these regions possess an unrealistically high magnetic moment.

Thus, we arrive at a number of questions, the answers to which are yet unknown.

What is the order parameter of the revealed magnetic phase transition? Namely, is the observed phase transition a proper magnetic transition or is it a manifestation of the structural phase transition whose order parameter is related to magnetization?

What is the microscopic nature of the magnetization? Is the revealed ferromagnetic anomaly a result of the correlation of ferromagnetically ordered clusters occurring in the paramagnetic matrix or is it caused by a change in the symmetry of the crystal lattice in a uniform state of the magnetic system?

Since T_c weakly depends on x, it is possible that the revealed ferromagnetism can persist at oxygen concentrations that are sufficient for the appearance of superconductivity. However, all these questions require further investigation.

We are grateful to S.N. Barilo for supplying us with high-quality samples grown by himself. We are also grateful to A.A. Zakharov, A.N. Bazhan, E.P. Krasnoperov, and A.A. Chernyshev for the interest taken in our study and for valuable comments expressed in discussing the experimental data. We acknowledge the support and assistance of M.B. Tsetlin, M.N. Khlopkin, A.A. Shikov, V.S. Kruglov, and P.V. Volkov.

This work was performed under the State Contract (project no. 107-1(00)-II) of the Ministry of Science of the Russian Federation; the Institute of Solid State Physics, Russian Academy of Sciences; and the Federal Scientific Engineering Program “Studies and Developments in the Priority Directions of Science and Engineering of Civil Significance” within the “Microlayering” theme.

REFERENCES

1. A. A. Zakharov, A. A. Nikonov, O. E. Parfionov, *et al.*, Physica C (Amsterdam) **223**, 157 (1994); A. A. Zakharov, S. N. Barilo, A. A. Nikonov, and O. E. Parfionov, Physica C (Amsterdam) **235–240**, 341 (1994); A. A. Zakharov and A. A. Nikonov, Pis’ma Zh. Éksp. Teor. Fiz. **60**, 340 (1994) [JETP Lett. **60**, 348 (1994)].
2. A. A. Zakharov, A. A. Nikonov, and O. E. Parfenov, Pis’ma Zh. Éksp. Teor. Fiz. **64**, 152 (1996) [JETP Lett. **64**, 162 (1996)]; A. A. Nikonov, O. E. Parfenov, and A. A. Zakharov, Pis’ma Zh. Éksp. Teor. Fiz. **66**, 159 (1997) [JETP Lett. **66**, 165 (1997)]; A. A. Zakharov, A. A. Nikonov, and O. E. Parfionov, Phys. Rev. B **57**, R3233 (1998).
3. A. S. Borovik-Romanov and N. M. Kreĭnes, Zh. Éksp. Teor. Fiz. **33**, 1119 (1957) [Sov. Phys. JETP **6**, 862 (1958)].
4. E. A. Turov, *Physical Properties of Magnetically Ordered Crystals* (Akad. Nauk SSSR, Moscow, 1963; Academic, New York, 1965).
5. A. N. Bazhan, V. N. Bevz, V. A. Merzhanov, *et al.*, Pis’ma Zh. Éksp. Teor. Fiz. **48**, 21 (1988) [JETP Lett. **48**, 21 (1988)]; Tineke Thio, T. R. Thurston, N. W. Preyer, *et al.*, Phys. Rev. B **38**, 905 (1988); K. Fukuda, M. Sato, S. Samato, *et al.*, Solid State Commun. **63**, 811 (1987); D. C. Jonston, S. K. Sinha, A. J. Jacobson, and J. M. Newsam, Physica C (Amsterdam) **153–155**, 572 (1988).
6. S. N. Barilo, A. P. Ges’, S. A. Guretskii, *et al.*, in *Proceedings of the International Conference on HTSC Material Aspect, Garmiscl-Partenkirchen, 1990*, Vol. 1, p. 107.
7. V. Yu. Pomjakushin, A. A. Zakharov, A. Amato, *et al.*, Physica C (Amsterdam) **272**, 250 (1996); A. M. Balagurov, V. Yu. Pomjakushin, V. G. Simkin, and A. A. Zakharov, Physica C (Amsterdam) **272**, 277 (1996).
8. F. C. Chou, F. Borsa, J. H. Cho, *et al.*, Phys. Rev. Lett. **71**, 2323 (1993); D. C. Jonston, F. Borsa, J. H. Cho, *et al.*, J. Alloys Compd. **207/208**, 206 (1994).
9. A. A. Nikonov, Prib. Tekh. Éksp., No. 6, 168 (1995).
10. J. C. Grenier, N. Laqueyte, A. Wattiaux, *et al.*, Physica C (Amsterdam) **202** (3–4), 209 (1992).
11. R. J. Birgeneau, J. Als-Nielsen, and G. Shirane, Phys. Rev. B **16**, 280 (1977).

Translated by E. Golyamina

JETP Letters, Vol. 72, No. 11, 2000, pp. 553–556. Translated from Pis'ma v Zhurnal Éksperimental'noĭ i Teoreticheskoĭ Fiziki, Vol. 72, No. 11, 2000, pp. 802–806.

Conductance of a 2D Electron System at Low Frequencies

V. B. Shikin

Institute of Solid State Physics, Russian Academy of Sciences, Chernogolovka, Moscow region, 142432 Russia

Received November 2, 2000

Low-frequency features of the conductance of a 2D electron system are considered. It is shown that, in addition to the parameter $\omega\tau$ (ω is the external frequency and τ is the elastic relaxation time), which occurs in the frequency dependence of the 3D conductivity in the Drude approximation, the 2D conductance contains other dimensionless combinations that involve the external frequency and the 2D conductivity. The notion of the "mobility" of a 2D system as the quantity governing the deviation of the conductance of the 2D system with ac current from its conductance under stationary conditions is introduced. Experimental data testifying to the presence of the discussed features of the 2D conductance are presented. © *2000 MAIK "Nauka/Interperiodica".*

PACS numbers: 73.50.Bk

The frequency dependence of the conductivity of 3D samples is controlled (at least in the Drude approximation) by the parameter $\omega\tau$, where τ is the momentum relaxation time and ω is the frequency of the external signal. In 2D systems, the situation is different mainly because of the Coulomb effects. In particular, in 3D samples, a uniform electric field E does not cause any electron density perturbation δn, because $\delta n \propto dE/dx$, where $E(x)$ is the local electric field. By contrast, for a uniform electric field to persist in 2D systems, the uniformity of the electron density must be perturbed (some details of such a comparison can be found below). At finite frequencies, this gives rise to additional electron transport along the bias field. Hence, the definition of the transport current must contain new dimensionless combinations that involve the conductivity σ and compete with $\omega\tau$.

The statement concerning the necessary perturbation of the 2D electron density by a bias electric field has some exceptions which are worth mentioning. One of them (the Dolgopolov remark) is related to the fact that lead terminals have the form of two conducting plates of finite area normal to the surface of the 2D system (a parallel-plate capacitor shortened by a 2D conductor). In this example, a bias field applied along the 2D system does not affect the spatial uniformity of its density. However, at finite frequencies, a substantial part of the conductance of the system under discussion is represented by the capacity of a parallel-plate capacitor formed by the terminals. The behavior of such systems requires special consideration and will be discussed elsewhere.

The purpose of this paper is the calculation of the conductance Σ for typical 2D charged systems with flat terminals in the low-frequency regime. As will be shown below, this conductance contains additional (i.e., in addition to $\omega\tau$) frequency-dependent parameters of the 2D transport

$$I_x = \Sigma_{xx} V, \tag{1}$$

where I is the total current and V is the voltage between two fixed points of the 2D system. The conventional local Ohm's law

$$j = \sigma E, \tag{1a}$$

where σ is the conductivity of the 2D system, holds at finite frequencies, but the bias electric field is nonuniform over the sample: $E = E(x)$. Therefore, it is more convenient to use Ohm's law in the form of Eq. (1).

In addition to the conductance, it is worthwhile to introduce the "mobility" M of the 2D system at finite frequencies. This parameter shows how effectively the 2D system adjusts to its stationary current state. For a 2D system without capacity in the dc regime, the mobility M can be represented by the ratio

$$M = I_x(\omega)/I_x(0), \tag{2}$$

where $I_x(0)$ is the transport current at zero frequency.

1. We begin with a Corbino disk with a given uniform 2D electron density n_s (the control electrode is absent). The magnetic field is zero, and the external frequency is finite but low [the upper limit for this parameter is specified below, see inequality (7)]. The terminals lie in the same plane as the 2D system and have zero thickness.

In this case, the combination of three equations, namely, the equations of motion and continuity and the

Poisson equation, yields the following equation for the electric potential $\varphi(x)$:

$$\varphi''(x) = \frac{i\omega\kappa m_*(i\omega + \tau^{-1})}{2\pi^2 e^2 n_s}\int_{-w}^{+w}\frac{\varphi'(s)ds}{x-s}, \quad (3)$$

$$\varphi(x) = \begin{cases} 0, & -\infty \le x \le -w \\ V(t) & +w \le x \le +\infty. \end{cases} \quad (3a)$$

Here, m_* is the effective mass of a charge carrier in the 2D system, κ is the dielectric constant of the medium, and $2w$ is the size of the 2D system along the current.

Equation (3) was obtained for a quasi-one-dimensional Corbino disk, i.e., for the case

$$\frac{R_1 - R_2}{R_1 + R_2} \equiv \frac{2w}{R_1 + R_2} \ll 1. \quad (3b)$$

In addition, the metal terminals contacting the 2D system are equipotential, lie in the plane of the 2D system, and extend to $\pm\infty$.

Equation (3) taken with the zero boundary conditions for the electric field at the ends of the $\pm w$ strip,

$$\varphi'(\pm w) = 0,$$

determines the natural plasma frequencies of a 2D strip of width $2w$ [1]. The same equation written for an unbounded medium with the initial excess charge distribution in the form of a δ function describes the specific "spread" of charge in 2D systems [2, 3]. The object of interest is the conductance of the Corbino disk at a fixed, sufficiently low frequency corresponding to the oscillation of the bias voltage $V(t)$ [Eq. (3a)] between the metal terminals.

In this case, the stationary state with $I_x(0)$ is described as follows:

$$I_x(0) = \sigma_{xx}(0)V/2w, \quad \delta n(x) \propto Vx/\sqrt{w^2 - x^2}. \quad (4)$$

Here, $\delta n(x)$ is the surface perturbation of the electron density because of the current along the 2D system and $\sigma_{xx}(0)$ is the conductivity in the Drude approximation at zero frequency [the explicit form of $\sigma_{xx}(\omega)$ is given below, see Eq. (10)].

Evidently, Eqs. (4) are also valid for a thin (in the sense $w \gg d$, where d is the sample thickness) 3D conducting plate. In both 2D and 3D cases, the external electric potential distribution, which causes the perturbation $\delta n(x)$ given by Eq. (4), is the same. However, for a 3D plate of finite thickness $d \gg d_{screen}$, this perturbation affects only the surface layer up to the vertical screening depth d_{screen} (recall that the presence of a constant electric field does not perturb the electron density in the bulk of a 3D system). Therefore, the perturbation $\delta n(x)$ [Eq. (4)] is insignificant for describing the stationary bias current state of a 3D system in the case

$$d \gg d_{screen}. \quad (5)$$

By contrast, the vertical screening in 2D systems is totally absent and, hence, inequality (5) never holds.

Turning to Eq. (3) with the low-frequency region in mind, we represent solution (2) in the form of a series

$$\varphi(x, t) = E(t)(x + w) + \varphi_1(x, t) + \ldots,$$
$$E(t) = V(t)/2w, \quad V(t) = V\exp(i\omega t), \quad (6)$$

for the frequencies

$$\omega \ll \omega_p^{\min}, \quad (7)$$

where $\omega_p^{\min}$ is the minimum transverse plasma frequency in a 2D strip of width $2w$.

Substituting Eq. (6) in Eq. (3) and combining the terms of the same order of magnitude in $\omega\tau_\sigma$, we obtain the following chain of equations [the definition of τ_σ is given below, see Eq. (11)]:

$$\varphi_1''(x) = \frac{i\omega\kappa E}{2\pi^2\sigma_{xx}}\ln\frac{w+x}{w-x},$$
$$\varphi_1(\pm w) = 0, \quad E = V/2w, \quad (8)$$

$$\varphi_2''(x) = \frac{i\omega\kappa}{2\pi^2\sigma_{xx}}\int_{-w}^{+w}\frac{\varphi_1'(s)ds}{x-s}, \quad \varphi_2(\pm w) = 0, \quad (9)$$

$$\varphi_3''(x) = \frac{i\omega\kappa}{2\pi^2\sigma_{xx}}\int_{-w}^{+w}\frac{\varphi_2'(s)ds}{x-s}, \quad \varphi_3(\pm w) = 0, \quad (10)$$

$$\sigma_{xx}(\omega) = \frac{n_s e^2}{m_*(i\omega + \tau^{-1})}$$

and so on.

According to Eqs. (8)–(10), series (6) converges when

$$\omega\tau_\sigma \ll 1, \quad \tau_\sigma = \kappa w/2\pi^2\sigma_{xx}. \quad (11)$$

Combination (11) (along with $\omega\tau$) determines the properties of the low-frequency 2D conductance.

The appearance of the additional relaxation time τ_σ given by Eq. (11) is quite natural from the dimensional point of view. However, dimensional considerations are not always sufficient for the realization of one or another effect. For example, the 3D conductivity σ_3 is expressed in inverse seconds, whereas the frequency dependence $\sigma_3(\omega)$ does not contain the parameter $\omega\sigma_3^{-1}$. In our case, combination (11) automatically appears in solving Eq. (4) and determines, to a great extent, the properties of the low-frequency conductance.

Indications of the existence of time τ_σ can be found among the results [2] on the "spreading" of a local perturbation of the electron density. In [2], it was shown that, in a cylindrically symmetric problem, the initial δ perturbation of electron density is spread in the radial direction with the linear velocity $\propto\sigma$. It is clear that, within the time R/σ, the density perturbation propagates to the distance R. This fact can serve as a basis for the introduction of the time τ_σ. However, e.g., in the absence of cylindrical symmetry, the spreading of an electron fluctuation is a more complicated process [3]. One should also mention paper [4] on the conductance of a screened Hall sample at finite frequencies in a magnetic field normal to its surface in the quantum Hall effect (QHE) regime. The QHE is a rather specific phenomenon. Hence, there are no reasons to draw the analogy between the cited publication [4] and this paper, although certain evidence of the existence of time τ_σ can be found in [4] (as well as in [2, 3]).

Thus, we can conclude that result (11) correlates well with the preceding statements and offers sufficiently general grounds for its appearance among the main parameters of the conductance.

Returning to the calculations and restricting ourselves to the determination of the correction $\varphi_1(x)$, we integrate Eq. (8):

$$\varphi_1'(x) = \frac{i\omega\kappa E}{2\pi^2\sigma_{xx}(\omega)}\left[\int_{-w}^{+x} ds \ln\frac{w+s}{w-s} + A\right], \qquad (12)$$

$$\varphi_1(x) = \frac{i\omega\kappa E}{2\pi^2\sigma_{xx}(\omega)}\left[\int_{-w}^{+x} ds \int_{-w}^{+s} dt \ln\frac{w+t}{w-t} + Ax + B\right]. \qquad (13)$$

The constants A and B in Eq. (13) are chosen to satisfy the boundary conditions for Eq. (8),

$$\varphi_1(\pm w) = 0,$$

which yields

$$Aw = B, \quad 2B = -\frac{i\omega\kappa E}{2\pi^2\sigma_{xx}(\omega)}\int_{-w}^{+w} ds \int_{-w}^{+s} dt \ln\frac{w+t}{w-t}. \qquad (14)$$

Using Eqs. (8), (12), and (14), we determine the current–voltage characteristic in the linear approximation with respect to $\omega\tau_\sigma$:

$$I_x = \sigma_{xx}(\omega)[E + \varphi_1'(w)]. \qquad (15)$$

Then, we obtain the conductance

$$\Sigma_{xx} = \sigma_{xx}(\omega)[1 + i(a-b)\omega\tau_\sigma + \ldots]/2w,$$
$$a = \int_{-1}^{+1} ds \ln\frac{1+s}{1-s}, \quad b = 0.5\int_{-1}^{+1} ds \int_{-1}^{+s} dt \ln\frac{1+t}{1-t}. \qquad (16)$$

The constants a and b are of the order of unity.

The mobility of a 2D Corbino disk without a screen is determined by the expression

$$M = \sigma_{xx}(\omega)[1 + i(a-b)\omega\tau_\sigma + \ldots]/\sigma_{xx}(0). \qquad (17)$$

Evidently, the value of M is close to unity as long as the conditions

$$\omega\tau \ll 1, \quad \omega\tau_\sigma \ll 1 \qquad (18)$$

are satisfied. As σ_{xx} decreases, the second of inequalities (18) ensuring good mobility becomes governing.

2. Results (16) and (17) are sufficiently reliable in the region of their validity (3b) and (18). As for the experimental verifications, the author of this paper, unfortunately, is not aware of any publications concerned with the conductance of the Corbino disk in the conditions discussed above. However, there are various indirect indications of the existence of time τ_σ. First of all, in paper [5] demonstrating the complex relaxation behavior of a 2D Hall sample under the action of sharp isolated spikes of the bias field, one of the characteristic times (the longest) was found to be inversely proportional to the conductivity of the 2D system. This observation correlates with the properties of τ_σ from Eq. (11). One should also note the series of works [6–10] with electrons at a helium surface in a magnetic field normal to this surface. The cited papers report considerable deviations of the magnetic-field dependence of electron-gas conductivity from the theoretical dependence $\sigma_{xx}(H) \propto H^{-2}$ obtained in the classical Drude approximation. With increasing H, the dependence $\sigma_{xx}(H)$ becomes smoother. The existing explanation of this phenomenon is based on the change of priorities: the interband transitions, yielding $\sigma_{xx}(H) \propto H^{-2}$, are replaced by the intraband transitions at the lowest Landau level, which are more probable at high cyclotron energies. It seems quite possible that, by introducing the conductance in the form of Eq. (16) in the problems with electrons above helium, one will arrive at an alternative explanation for the magnetic anomalies from [6–10], because, in this case, a decrease in the conductivity must be accompanied by a partial self-compensation of its magnetic field dependence. Finally, definition (17) of the mobility offers an explanation for the frequency range within which the negative compressibility of the 2D electron (hole) gas was observed in the experiments [11–13]. The interpretation of these experiments assumes a good mobility of the 2D channel: $M \leq 1$. A decrease in the 2D electron density, which is involved in the technique [11–13], inevitably violates this inequality. The competition of the aforementioned factors determines the frequency range of their coexistence.

To summarize, one can say that, at low frequencies, the conductance of 2D charge systems exhibits interesting qualitative features that deserve special consideration. These features indirectly manifest themselves in the known experiments. However, it is desirable to per-

form direct measurements of the conductance under the conditions close to those studied in calculation.

I am grateful to V.T. Dolgopolov for discussing the results of this study and for valuable comments. This work was supported in part by the Russian Foundation for Basic Research (project no. 98-02-16640) and the INTAS Network (project no. 97 1643).

REFERENCES

1. V. Shikin, T. Demel, and D. Heitman, Phys. Rev. B **46**, 3971 (1992).
2. A. Govorov and A. Chaplik, Poverkhnost, No. 12, 5 (1987).
3. M. D'yakonov and A. Furman, Zh. Éksp. Teor. Fiz. **92**, 1012 (1987) [Sov. Phys. JETP **65**, 574 (1987)].
4. I. Dolgopolov and S. Dorozhkin, Poverkhnost, No. 2, 5 (1985).
5. N. Zhitenev, Pis'ma Zh. Éksp. Teor. Fiz. **55**, 722 (1992) [JETP Lett. **55**, 756 (1992)].
6. R. van der Heijden *et al.*, Europhys. Lett. **6**, 75 (1988).
7. J. Frost, P. Fozooni, M. J. Lea, and M. I. Dykman, Europhys. Lett. **16**, 575 (1991).
8. P. Peters, P. Scheuzger, M. J. Lea, *et al.*, Phys. Rev. B **50**, 11570 (1994).
9. M. Dykman, C. Fang-Yen, and M. Lea, Phys. Rev. B **55**, 16249 (1997).
10. M. Lea *et al.*, Phys. Rev. B **55**, 16280 (1997).
11. J. Eisenstein, L. Pfeifer, and K. West, Phys. Rev. Lett. **68**, 674 (1992).
12. J. Eisenstein, L. Pfeifer, and K. West, Phys. Rev. B **50**, 1760 (1994).
13. S. Dultz and H. Jiang, Phys. Rev. Lett. **84**, 4689 (2000).

Translated by E. Golyamina

JETP Letters, Vol. 72, No. 11, 2000, pp. 557–560. Translated from Pis'ma v Zhurnal Éksperimental'noĭ i Teoreticheskoĭ Fiziki, Vol. 72, No. 11, 2000, pp. 807–812.

Pressure-Induced Dimerization Kinetics of Fullerene C_{60}

V. A. Davydov[1,2], L. S. Kashevarova[1], A. V. Rakhmanina[1], V. M. Senyavin[3], O. P. Pronina[3], N. N. Oleĭnikov[3], V. Agafonov[4], and H. Szwarc[5]

[1] *Institute of High-Pressure Physics, Russian Academy of Sciences, Troitsk, Moscow region, 142190 Russia*
[2] *e-mail: vdavydov@hppi.troitsk.ru*
[3] *Moscow State University, Vorob'evy gory, Moscow, 119899 Russia*
[4] *Laboratoire de Chimie Physique, Faculte de Pharmacie de l'Universite de Tours, 37200 Tours, France*
[5] *Laboratoire de Chimie Physique des Materiaux Amorphes, Universite Paris XI, 91405 Orsay, France*
Received November 9, 2000

Dimerization kinetics was studied for fullerene C_{60} by IR spectroscopy at a pressure of 1.5 GPa in the temperature range 373–473 K. The kinetic curves for the formation of a dimer $(C_{60})_2$ were obtained using its analytical IR band at 796 cm^{-1}. Under the assumption that pressure-induced C_{60} dimerization is a second-order irreversible reaction, the reaction rate constants were determined at different temperatures. The corresponding activation energy and preexponential factor were found to be 134 ± 6 kJ/mol and $(1.74 \pm 0.24) \times 10^{14}$ s^{-1}, respectively. The specific features of the solid-phase C_{60} dimerization in simple cubic and face-centered cubic fullerite phases are discussed. © *2000 MAIK "Nauka/Interperiodica".*

PACS numbers: 82.35.+t; 61.48.+c; 62.50.+p

The purpose of this work consisted in direct experimental determination of the kinetic parameters for the pressure-induced polymerization of fullerene C_{60} and, in particular, determination of the activation energy for the polymerization processes occurring through the [2+2] cycloaddition of C_{60} molecules [1]. The data on these processes are scarce and rather contradictory. At present, despite a considerable number of studies associated with the determination of activation energy for depolymerization of C_{60} polyfullerenes [2–7], we can cite only two works that are devoted to determination of the activation barrier to a direct polymerization reaction. In the first of them [8], the activation energy for the pressure-induced polymerization of C_{60} was found to be 38.6 kJ/mol, although it was derived from the gross characteristic of the material—its thermal conductivity. In the second work [9], the molecular dynamics method was used to estimate the activation energy for dimerization ($E_{a(dim)}$) of the C_{60} molecules to arrive at the 400.4 kJ/mol value. A comparison of these theoretical and experimental activation energies demonstrates that the discrepancy is too great. It should be noted that the authors of [8], when discussing the obtained activation energy, pointed out with surprise that it proved to be several times lower than the experimentally measured activation barriers to depolymerization of polyfullerenes. The latter are equal to 120.6, 168.8, and 183.3 kJ/mol for the C_{60} photopolymers [2], dimers, and chain and linear polymers [3], respectively. The theoretical estimates of the activation energies for depolymerization of, say, $(C_{60})_2$ dimer yield, on the whole, even higher values: 154.7 [4], 193–386 [5], 232 [6], 338 [7], and 273 kJ/mol [9].

In this work, an attempt is also undertaken to study the influence of a crystal phase of fullerite on the kinetics of pressure-induced polymerization. The revelation of a "temperature threshold of photopolymerizability" [10, 11] near the point of phase transition between the orientationally disordered face-centered cubic (FCC) and orientationally ordered simple cubic (SC) fullerite phases (260 K at 1 atm [12–15]), which is indicative of the inhibition of photopolymerization in the SC phase because of the prevalence of C_{60} orientations unfavorable for the [2+2] cycloaddition in this phase, forced us to carry out closer inspection of this problem from the viewpoint of pressure-induced transformations in the SC phase.

The pressure-induced C_{60} dimerization [16] was chosen as the object of investigation, because it holds particular interest as the elementary event of the fullerene polymerization process. The dimerization was studied at a pressure of 1.5 GPa. According to the portion of the (p, T) diagram of C_{60} (Fig. 1) constructed using the data of works [12–15, 17–21], one can assume that the temperature of transition between the fullerite SC and FCC phases at 1.5 GPa is ~423 K. Following this estimate, the kinetic measurements were performed over the temperature range of 373–473 K extending to 50 K into the domain of existence of both SC and FCC phases. The experimental part of the work

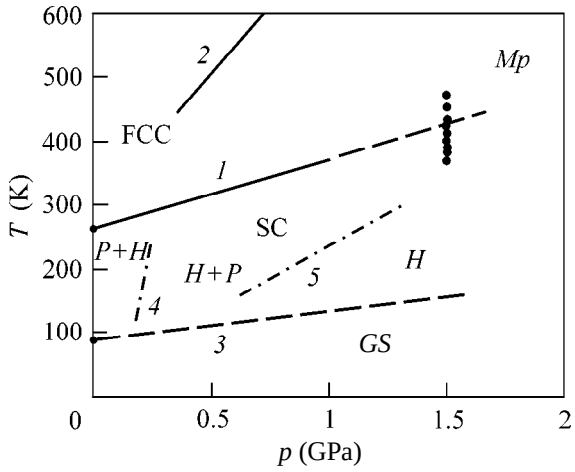

Fig. 1. Phase diagram of C_{60}. Phase boundaries between the monomeric FCC phase and the monomeric SC phase [13, 14] and the polymerized (*Mp*) states of the system [17] are labeled *1* and *2*. Line *3* is the phase boundary between the orientationally ordered (*P*, *H*) and glassy (*GS*) states [18–20]. Line *4* corresponds to the *p*, *T* parameters for which the fraction ratio of the *P* and *H* orientations of C_{60} is unity ([*P*]/[*H*] = 1) [20, 28]. Line *5* is the boundary between the domains of existence of mixed (*H*, *P*) and *H* orientations [20, 21].

consisted in the synthesis of dimerized states of the system at 1.5 GPa at temperatures 373, 383, 393, 403, 413, 423, 433, 453, and 473 K (indicated by black circles in Fig. 1) and for times from 1 to 50 000 s; the isolation of high-pressure states under normal conditions by pressure quenching; and the analysis of these states by the IR spectroscopic method. A fullerite powder with a C_{60} content of 99.9% was taken as a starting material. Synthesis was conducted on high-pressure "Maxim" (of the "piston–cylinder" type) and "Toroid" apparatus equipped with a temperature controller allowing one to control a predetermined heating rate (15 K/s) and maintain the isothermal annealing temperature with an accuracy of ±2 K. Other synthesis details are described in [22]. The IR spectra of the samples as powders with potassium bromide were recorded on a Specord M80 (Carl Zeiss) spectrometer.

A typical evolution of the IR spectra as functions of annealing time is shown in Fig. 2 for the samples prepared at 1.5 GPa and 393 K. These spectra clearly demonstrate the changes in the IR intensities of the $(C_{60})_2$ molecules at 796, 478 cm^{-1}, etc. [16, 23, 24], allowing the kinetic curves to be constructed for the dimerization reaction. The time-dependent optical density at the maximum of the 796 cm^{-1} band, chosen as an analytical band of the dimer molecule, is shown in Fig. 3 for different temperatures. These curves indicate that the mechanisms of C_{60} dimerization at temperatures above and below 423 K are different. The curves at temperatures below 423 K correspond, according to Fig. 1, to

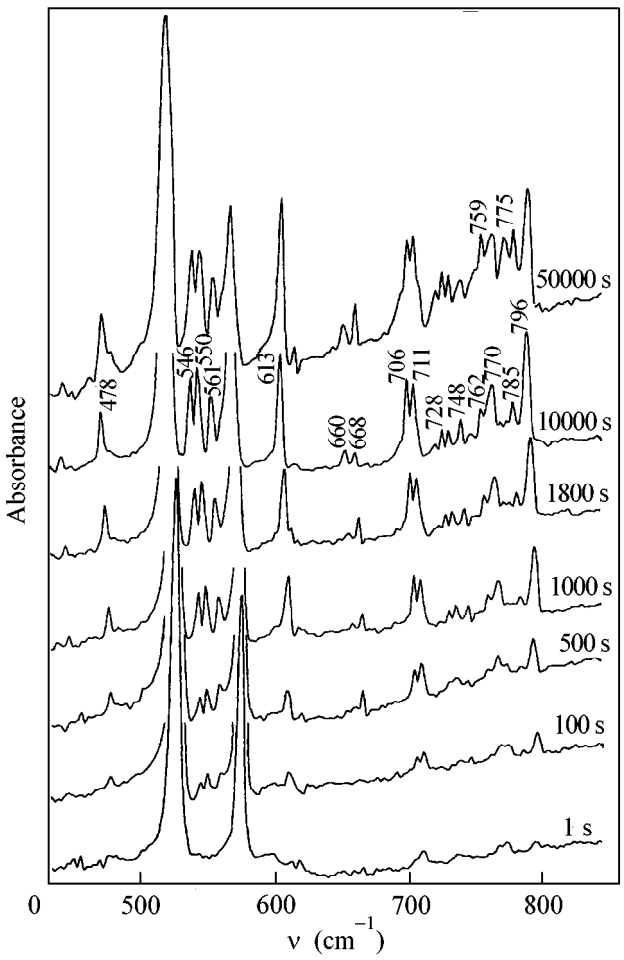

Fig. 2. IR spectra of the samples prepared by treating fullerite C_{60} at 1.5 GPa, 393 K, and by isothermal annealing for 1 to 50000 s.

the SC phase. They are characterized by a well-defined induction period and are S-shaped, typical of autocatalytic reactions. At temperatures above 423 K corresponding to the fullerite FCC phase, the induction period is absent and $(C_{60})_2$ is formed in a considerable amount even within the first seconds of isothermal annealing. The presence of maxima in the kinetic curves is also noteworthy because they are evidence that, at the indicated *p*, *T* parameters of fullerite annealing, the dimer is not a final product of transformation on the way to the linear C_{60} polymers but is an intermediate product. The presence of linear polymers in the samples prepared by prolonged annealing is evident from the appearance of the IR bands at 778 and 759 cm^{-1} (Fig. 2) that are typical of the orthorhombic polymerized C_{60} phase [16, 24].

Considering these kinetic features, the rate constants were determined from the curve portions excluding the induction periods and the domains with a detectable content of linear C_{60} polymers. For this rea-

son, the data obtained at a temperature of 473 K were fully excluded from the analysis.

The content of dimeric molecules in the samples was determined by measuring the optical density at the maximum of the analytical band, correcting it for the concentration of the sample in the KBr pellet and its thickness, and normalizing to the optical density measured for the corresponding band in a pellet containing a known amount of pure $(C_{60})_2$ dimer. The latter sample was prepared through mechanochemical synthesis [23] and kindly provided by Prof. K. Komatsu.

This procedure was used to determine the extent of transformation (α) for the reaction

$$2C_{60} = (C_{60})_2 \quad (1)$$

at different temperatures and for different times of isothermal annealing. Further data processing was carried out under the assumption that the pressure-induced dimerization is a second-order irreversible reaction. In this case, the integral form of the kinetic equation is

$$kt = \alpha/(1-\alpha), \quad (2)$$

where k is the reaction rate constant and t is the annealing time.

The logarithmic rate constant calculated by Eq. (2) for different temperatures is shown in Fig. 4 as a function of the inverse temperature. The black squares are the experimental data and the straight lines are the result of their least-squares processing. The preexponential factor and the activation energy for the C_{60} dimerization were determined using the Arrhenius equation

$$k = A\exp(-E_a/RT). \quad (3)$$

In the variant when the experimental data were processed over the entire temperature range (dashed line in Fig. 4), these values were found to be $A = (1.74 \pm 0.24) \times 10^{14}$ s^{-1} and $E_{a(dim)} = 134 \pm 6$ kJ/mol.

Although the experimental data in Fig. 4 do not give explicit evidence of a change in the transformation mechanism upon the transition from the SC to the FCC phase, they were also processed separately in two temperature ranges, 373–413 and 423–453 K (solid lines in Fig. 4). The resulting activation energies for C_{60} dimerization in the fullerite SC and FCC phases were estimated at 137 ± 16 and 121 ± 22 kJ/mol, respectively. Although the accuracy of these estimates is low because of the narrow temperature ranges and small number of experimental points, one can notice that, having regard to errors of measurement, the difference between the $E_{a(SC)}$ and $E_{a(FCC)}$ values is consistent with the enthalpy of phase transition between the SC and FCC phases at atmospheric pressure (~9 kJ/mol [25]).

A comparison with the literature data indicates that the activation energy obtained in this work for reaction (1) far exceeds the value of 38.6 kJ/mol found by Soldatov *et al.* in [8] for E_a of the pressure-induced C_{60} polymerization. Although our $E_{a(dim)}$ value is still appreciably lower than its theoretical estimate 400.4 kJ/mol obtained by Ozaki *et al.* in [9], it agrees satisfactorily with the above-mentioned experimental and some theoretical estimates of the activation energies for the dissociation of the dimeric molecule [2–4].

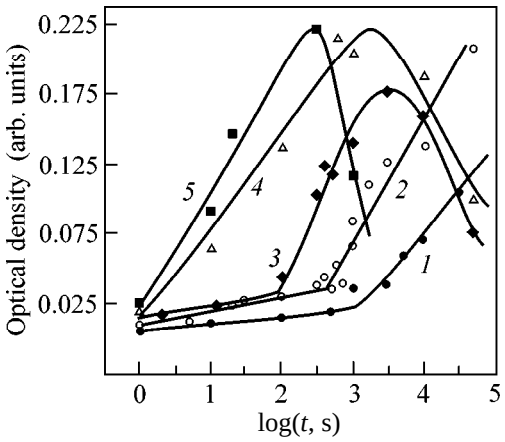

Fig. 3. Optical density at the maximum of analytical band of the $(C_{60})_2$ molecule vs. logarithm of isothermal annealing time for the samples prepared by treating fullerite C_{60} at 1.5 GPa and temperatures (*1*) 373, (*2*) 393, (*3*) 413, (*4*) 423, and (*5*) 453 K.

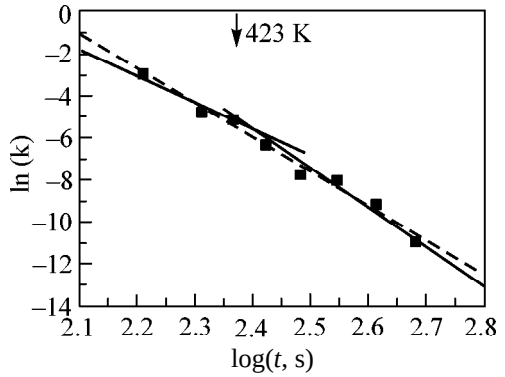

Fig. 4. Logarithmic rate constant for dimerization of C_{60} at 1.5 GPa vs. inverse temperature. The dashed line corresponds to the variant in which the experimental data were processed over the entire temperature range, and the solid lines correspond to the variants in which two temperature ranges 373–413 and 423– 453 K were processed separately.

The qualitative distinctions between the dimerization curves in the SC and FCC phases indicate that the molecular orientation and the mobility of C_{60} molecules in the fullerite lattice influence the pressure-induced polymerization of C_{60}, as well as its photopolymerization. However, whereas the transition from FCC to SC is accompanied by the inhibition of photopolymerization [10], the dimerization in the SC phase upon pressure-induced transformations proceeds in the autocatalytic regime. A plausible explanation for this

may be that the contents of two, the so-called *P* and *H*, orientational states [26, 27] in the fullerite SC phase are different under the conditions of pressure-induced polymerization and photopolymerization at 1 atm. Since the proximity and parallel arrangement of the double carbon bonds of the neighboring C_{60} molecules is the necessary topochemical condition for the [2+2] cycloaddition reaction, it is then clear that the *P* orientation, for which the double bond of one molecule faces the center of the pentagonal cycle of the other, is most unfavorable for the polymerization. The enhanced content of *P* orientations in the SC phase at atmospheric pressure (~60% near the upper temperature phase boundary and 84% near its lower boundary at 90 K [26]) is the possible reason for the existence of a temperature threshold of photopolymerizability [10, 11]. Pressure buildup increases the content of *H* orientations in the SC phase, and, at pressures of ~1.5 GPa, their content becomes close to 100% [19, 20, 28, 29] (Fig. 1). Although the *H* orientation is also not optimum for the reaction, the appearance of favorable mutual molecular orientations, owing to the random thermally activated events, becomes much more probable in this case. The appearance of dimeric molecules results in a local disorder in the SC phase and, thus, "catalyzes" the reaction. Starting at a certain moment, the process becomes similar to the dimerization in the FCC phase.

This work was supported by the Russian Foundation for Basic Research (project no. 00-03-32600) and the INTAS (grant no. IR-97-1015). We are grateful to K. Komatsu for providing a pure sample of $(C_{60})_2$ dimer.

REFERENCES

1. A. M. Rao, P. Zhou, K. A. Wang, *et al.*, Science **259**, 955 (1993).
2. Y. Wang, J. M. Holden, X. Bi, *et al.*, Chem. Phys. Lett. **217**, 413 (1994).
3. P. Nagel, V. Pasler, S. Lebedkin, *et al.*, Phys. Rev. B **60**, 16920 (1999).
4. D. Porezag, M. R. Pederson, Th. Frauenheim, *et al.*, Phys. Rev. B **52**, 14963 (1995).
5. M. Menon, K. R. Subbaswamy, and M. Sawtarie, Phys. Rev. B **49**, 13966 (1994).
6. G. B. Adams, J. B. Page, O. F. Sankey, *et al.*, Phys. Rev. B **50**, 17471 (1994).
7. J. Fagerstrom and S. Stafstrom, Phys. Rev. B **53**, 13150 (1996).
8. A. Soldatov, K. Prassides, O. Andersson, *et al.*, in *Proceedings of the 193st ECS Meeting on Recent Advances in the Chemistry and Physics of Fullerenes and Related Materials, San Diego, 1998*, Vol. 6, p. 769.
9. T. Ozaki, Y. Iwasa, and T. Mitani, Chem. Phys. Lett. **285**, 289 (1998).
10. P. Zhou, Z.-H. Dong, A. M. Rao, *et al.*, Chem. Phys. Lett. **211**, 337 (1993).
11. B. Burger, J. Winter, and H. Kuzmany, Z. Phys. B **101**, 227 (1996).
12. P. A. Heiney, J. E. Fisher, A. R. McGhie, *et al.*, Phys. Rev. Lett. **66**, 2911 (1991).
13. G. Kriza, J.-C. Ameline, D. Jerome, *et al.*, J. Phys. I (France) **1**, 1361 (1991).
14. G. A. Samara, J. E. Schirber, B. Morosin, *et al.*, Phys. Rev. Lett. **67**, 3136 (1991).
15. W. I. F. David, R. M. Ibberson, T. J. S. Dennis, *et al.*, Europhys. Lett. **18**, 219 (1992).
16. B. A. Davydov, L. S. Kashevarova, A. V. Rakhmanina, *et al.*, Pis'ma Zh. Éksp. Teor. Fiz. **68**, 881 (1998) [JETP Lett. **68**, 928 (1998)].
17. I. O. Bashkin, V. I. Rashchupkin, A. F. Gurov, *et al.*, J. Phys.: Condens. Matter **6**, 7491 (1994).
18. O. Andersson, A. Soldatov, and B. Sundqvist, Phys. Rev. B **54**, 3093 (1996).
19. J. A. Wolk, P. J. Horoyski, and M. L. W. Thewalt, Phys. Rev. Lett. **74**, 3483 (1995).
20. B. Sundqvist, Adv. Phys. **48**, 1 (1999).
21. B. Sundqvist, O. Andersson, A. Lundin, *et al.*, Solid State Commun. **93**, 109 (1995).
22. V. A. Davydov, L. S. Kashevarova, A. V. Rakhmanina, *et al.*, Pis'ma Zh. Éksp. Teor. Fiz. **63**, 778 (1996) [JETP Lett. **63**, 818 (1996)].
23. K. Komatsu, G. W. Wang, Y. Murata, *et al.*, J. Org. Chem. **63**, 9358 (1998).
24. V. A. Davydov, L. S. Kashevarova, A. V. Rakhmanina, *et al.*, Phys. Rev. B **61**, 11936 (2000).
25. J. de Bruijn, A. Dvorkin, H. Szwarc, *et al.*, Europhys. Lett. **24**, 551 (1993).
26. W. I. F. David, R. M. Ibberson, T. J. S. Dennis, *et al.*, Europhys. Lett. **18**, 219 (1992).
27. P. A. Heiney, J. E. Fisher, and A. R. McGhie, Phys. Rev. Lett. **66**, 2911 (1991).
28. W. I. F. David and R. M. Ibberson, J. Phys.: Condens. Matter **5**, 7923 (1993).
29. O. Blaschko, W. Rom, and I. N. Goncharenko, J. Phys.: Condens. Matter **8**, 4235 (1996).

Translated by V. Sakun

JETP Letters, Vol. 72, No. 11, 2000, pp. 561–564. Translated from Pis'ma v Zhurnal Éksperimental'noĭ i Teoreticheskoĭ Fiziki, Vol. 72, No. 11, 2000, pp. 813–818.

Normal Spinel $CuCr_{1.6}Sb_{0.4}S_4$, a New Material with a Giant Magnetoresistance

L. I. Koroleva[1], R. V. Demin[1], J. Warczewski[2], J. Krok-Kowalski[2], T. Mydlarz[3], A. Gilewski[3], and A. Pacyna[4]

[1] *Moscow State University, Vorob'evy gory, Moscow, 119899 Russia*

[2] *Silesian University, Institute of Physics, ul. Uniwersytecka 4, 40007 Katowice, Poland*

[3] *International Laboratory of High Magnetic Fields and Low Temperatures, Gajowicka 95, 53-529 Wroclaw, Poland*

[4] *The Henryk Niewodniczanski Institute of Nuclear Physics, ul. Radzikowskiego 152, 31-342 Krakow, Poland*

Received November 13, 2000

A giant magnetoresistance, reaching 74% in a magnetic field of 38 T at 3 K, was observed in the $CuCr_{1.6}Sb_{0.4}S_4$ semiconductor spinel. The magnetic properties point to the existence of a magnetic two-phase state in this compound. The giant magnetoresistance was explained by the existence of the magnetic two-phase state due to strong *s–d* exchange. © *2000 MAIK "Nauka/Interperiodica".*

PACS numbers: 75.50.Pp; 75.70.Pa

In the last decade, interest has sharply risen in materials with a giant magnetoresistance because of their possible application in various sensor devices. In this work, a giant magnetoresistance was found in the $CuCr_{1.6}Sb_{0.4}S_4$ compound semiconductor consisting of a solid solution of two compounds with the normal spinel structure: the $Cu^{1+}Cr^{3+}_{1.5}Sb^{5+}_{0.5}S^{2-}_4$ antiferromagnet with conduction of the semiconductor type [1, 2] and the $Cu^{2+}Cr^{3+}_2S^{2-}_4$ ferromagnet with conduction of the metallic type [3, 4]. This is surprising, because no magnetoresistance was observed to within the experimental error (0.01%) in either $CuCr_{1.5}Sb_{0.5}S_4$ or $CuCr_2S_4$.

In this work, the magnetoresistance $\Delta\rho/\rho = (\rho_H - \rho_{H=0})/\rho_{H=0}$, the resistivity ρ, and the magnetization M of the $CuCr_{1.6}Sb_{0.4}S_4$ compound were investigated. A polycrystalline sample was obtained by solid-phase synthesis. The single-phase character of the sample was determined by X-ray powder diffraction analysis. The sample had a spinel structure with lattice parameter a = 9.9680(1) Å and anion parameter u = 0.3820(1). The magnetization in a constant magnetic field $H \le 14$ T was measured by the induction method, and the resistivity was measured by the four-probe method. Both a stationary magnetic field $H \le 10$ T and a pulsed magnetic field $H \le 38$ T were used for measuring the magnetoresistance. The experimental results are presented in Figs. 1–5. Note that the experimental error is smaller than the size of the symbols representing experimental points.

The dependence of $\ln\rho$ on the inverse temperature T is shown in Fig. 1. It is evident that the conduction of the sample is of the semiconductor type. The temperature dependence of the magnetoresistance at H = 10 T and 38 T is shown in Fig. 2. The longitudinal and transverse values of the magnetoresistance for the same value of magnetic field are equal. It is apparent in Fig. 2 that the magnetoresistance is negative and its value is very large: $\Delta\rho/\rho$ = 74% at T = 3 K and H = 38 T. It should be noted that saturation in the magnetoresistance isotherms is still not attained in a field of 38 T. At H = 38 T, $\Delta\rho/\rho$ monotonically decreases with decreasing temperature and approaches a value of ~ 4% at 39 K (the highest temperature at which the magnetoresistance was higher than the experimental error at H = 10 T). The Néel point for this composition, T_N = 42.8 K, was determined in [5] as the temperature corresponding to a maximum in the curve for the temperature dependence of the initial magnetic susceptibility measured in an alternating magnetic field in the frequency range from 0.25 to 4 kHz and was virtually independent of the frequency. In a field of 10 T, the $\Delta\rho/\rho(T)$ dependence is nonmonotonic; however, as in a field of 38 T, the absolute value of $\Delta\rho/\rho$ decreases as T_N is approached and becomes close to zero at $35 \le T \le 39$ K.

Magnetization isotherms of the sample cooled to 4.2 K in the absence of a magnetic field are shown in Fig. 3. It is evident in the figure that the $M(H)$ curves both above and below T_N can be represented as a sum of two parts: the magnetization linear in field and a small spontaneous magnetization. The spontaneous magnetization is much smaller than the magnetization of the ferromagnetically ordered sample. It turned out that, at $T < T_N$, the $M(H)$ curves obtained upon increasing and decreasing the field were different. Namely, a curve obtained upon field decrease is located higher than the corresponding curve obtained upon field increase. This difference is clearly seen in the $M(H)$

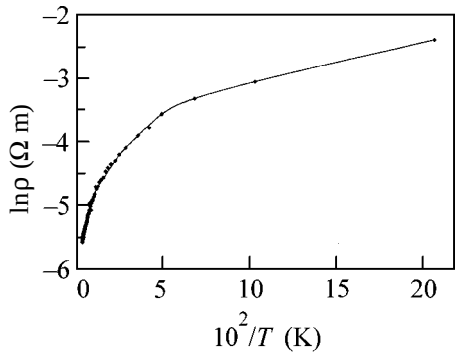

Fig. 1. Dependence of the natural logarithm of the resistivity lnρ on the inverse temperature.

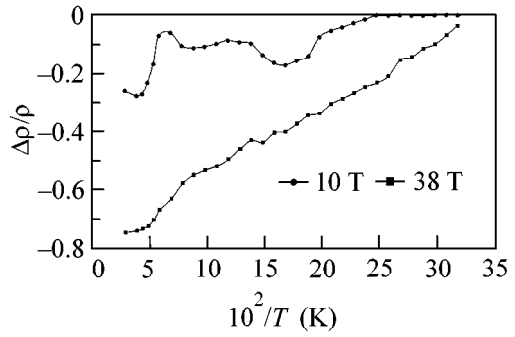

Fig. 2. Temperature dependence of the magnetoresistance $\Delta\rho/\rho(T)$ at two values of the magnetic field.

curve obtained at 4.2 K in fields below 4 T. At $T < T_N$, this distinction disappears. The $M(H)$ curves presented in Fig. 4 were obtained at the same temperatures as in Fig. 3; however, the sample was cooled before measurements from T = 300 K to T = 4.2 K in a field of 14 T. A comparison of Figs. 3 and 4 shows that the slope of the linear part of the $M(H)$ curves is the same for the same temperatures; however, the spontaneous magnetization is higher for the sample cooled in a field. Figure 5 demonstrates the temperature dependence of M in a field of 10 T obtained after cooling the sample from 300 to 4.2 K in the absence of a field (curve *1*) and in a field of 14 T (curve *2*). It is evident that curve *2* runs much higher than curve *1*; a broad maximum is observed in both curves in the region of T_N.

This behavior of magnetization can be ascribed to the existence of a magnetic two-phase state in the sample. At $T < T_N$, this state represents an antiferromagnetic (AFM) matrix with single-domain magnetic clusters with spontaneous magnetization canted. The magnetic moments of the clusters are coupled by exchange interaction with the antiferromagnetic matrix. Because of this interaction, the magnetic moments of the clusters are aligned with the antiferromagnetic vectors in the domains of the AFM matrix. At T close to T_N, when the magnetic anisotropy of the AFM matrix is small, the external magnetic field orients the antiferromagnetic vectors of the AFM domains along its own direction. This orientation persists on cooling down to $T \ll T_N$. On cooling without a field from $T > T_N$ to $T \ll T_N$, the antiferromagnetic vectors and the cluster magnetic moments coupled to these vectors are oriented along the light magnetization directions inside the domains. When a field is applied at $T < T_N$, the antiferromagnetic vectors and the cluster magnetic moments rigidly bound to these vectors are rotated together toward the field direction. Magnetic fields necessary for the cluster moments to be completely oriented are considerably higher than in the case of field cooling described above. Therefore, the spontaneous part of magnetization at the same temperature is higher for a sample cooled in a field than for one cooled without a field.

The fact that the moments and the number of magnetic clusters may depend on the temperature should also be taken into account. This is possible, for example, in the case of an AFM semiconductor with strong *s–d* exchange, in which magnetic clusters of the ferron or afmon type are arranged [6, 7]. Such a semiconductor is characterized by a giant magnetoresistance. Because of strong *s–d* exchange, it is energetically favorable for charge carriers in a semiconductor of this type to be localized near impurities and to maintain a ferromagnetic order around them. Such ferromagnetic clusters received the name ferrons. Not only ferromagnetic, but also some other phase can serve as a potential well for charge carriers. It can be, for example, an AFM phase but of a type other than that normally occurring in the crystal. The energy of charge carriers in this other phase must be lower than in the main AFM phase. This quasiparticle received the name afmon. As an example, an AFM semiconductor with a staggered AFM structure containing microregions with a layered AFM structure was considered in [7]. It is known that the energy of a charge carrier in a layered AFM phase is lower than in a staggered AFM phase, and their difference may reach several tenths of an electronvolt. Therefore, charge carriers in an AFM phase with staggered ordering may autolocalize in microregions with layered AFM ordering. Afmons can exist only in materials with sufficiently high T_N, where free ferrons cannot exist. The energy of such a quasiparticle (afmon) can be further lowered if the moments of the sublattices are canted; however, a large sublattice cant is excluded, because ferrons are energetically unfavorable.

The $CuCr_{1.6}Sb_{0.4}S_4$ compound considered in this work is a solid solution of two compounds: the $CuCr_2S_4$ compound, a ferromagnet with conduction of the metallic type [3, 4], and the AFM semiconductor $CuCr_{1.5}Sb_{0.5}S_4$ with the negative paramagnetic Curie point Θ = –156 K [1, 2]. Additions of $Cu^{2+}Cr_2^{3+}S_4$ in $Cu^{1+}Cr_{1.5}^{3+}Sb_{0.5}^{5+}S_4^{2-}$ may be considered as doping with divalent copper (acceptor) and the simultaneous substitution of Cr^{3+} ions for part of the Sb^{5+} ions. In this case, the compound considered in this work has the following dis-

tribution of valences: $Cu^{1+}_{0.8}Cu^{2+}_{0.2}Cr^{3+}_{1.6}Sb^{5+}_{0.4}S^{2-}_4$. It is evident from Figs. 3 and 4 that its magnetization isotherms are sums of the part linear in field and a small spontaneous magnetization. The paramagnetic susceptibility obeys the Curie–Weiss law. The paramagnetic Curie temperature is equal to 130 K and is much higher than the value $\Theta = -156$ K for $CuCr_{1.5}Sb_{0.5}S_4$ [5].

It is known that the value of Θ is determined by the sum of exchange interactions in the crystal. Because the paramagnetic Curie point in $CuCr_{1.5}Sb_{0.5}S_4$ is negative and large in absolute value, this antiferromagnet possibly possesses a staggered structure. It is not improbable that this compound is characterized by a more complicated magnetic structure in which AFM interactions predominate. The sharp increase in Θ for the $Cu^{1+}_{0.8}Cu^{2+}_{0.2}Cr^{3+}_{1.6}Sb^{5+}_{0.4}S^{2-}_4$ composition indicates that ferromagnetic exchange interactions originating, possibly, from microregions in the vicinity of Cu^{2+} impurity ions make a significant contribution to Θ.

Clusters of the ferron or afmon type are undeniably present in the given compound, because it exhibits a giant magnetoresistance. However, it is not clear which of the two types of clusters indicated above is present in the sample. It should be noted that the values of spontaneous magnetization determined by extrapolating the rectilinear portions of the $M(H)$ curves in Figs. 3 and 4 to the intersection with the M axis are small. The maximum value of the spontaneous magnetic moment μ determined from the spontaneous magnetization equals 0.51 μ_B/(chem. unit) at 4.2 K for the sample cooled in a field of 14 T from 300 to 4.2 K. At higher temperatures or at 4.2 K, but upon cooling the sample without a field, the value of μ decreases several times. The maximum value of μ indicated above is approximately one order of magnitude smaller than the value of the magnetic moment that would be observed for the $Cu^{1+}_{0.8}Cu^{2+}_{0.2}Cr^{3+}_{1.6}Sb^{5+}_{0.4}S^{2-}_4$ compound on complete ferromagnetic ordering of the moments of the Cr^{3+} and Cu^{2+} ions. The small value of μ is in agreement with the conclusions drawn in [6], where it was shown that the volume of the ferromagnetic phase in an impurity AFM semiconductor composed of ferromagnetic drops (ferrons) arranged in an AFM matrix comprises several percent of the entire sample volume. It is evident that the volume of the phase with a magnetic moment will be of the same order of magnitude or smaller in the case when the magnetic clusters in an AFM semiconductor are of the afmon type.

As was indicated in [7], afmons can exist in AFM semiconductors in which free ferrons (not associated with impurities) are energetically unfavorable. The value $T_N = 42.8$ K for $CuCr_{1.6}Sb_{0.4}S_4$ is higher than the limiting value $T_N = 15$ K for the existence of free ferrons. However, the ferrons in the compound under consideration are impure. Their formation in an impurity AFM semiconductor is significantly facilitated, because, in addition to *s–d* exchange, Coulomb attraction favors the localization of charge carriers near impurities. Therefore, ferrons can exist in impurity AFM semiconductors with Néel temperatures higher than 15 K. Because of the aforesaid, it is not clear at present which quasiparticles, ferrons or afmons, are responsible for the giant magnetoresistance in the compound under consideration.

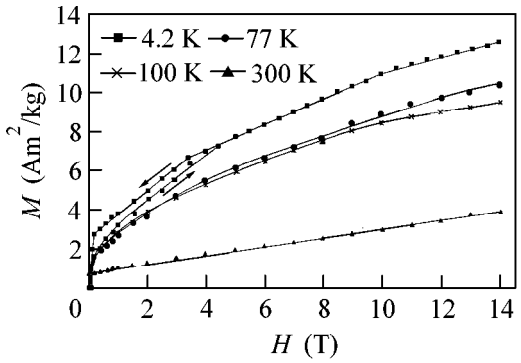

Fig. 3. Magnetization isotherms at several temperatures obtained after cooling the sample from 300 to 4.2 K in the absence of a magnetic field.

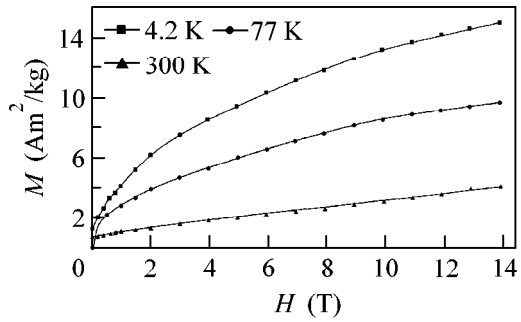

Fig. 4. Magnetization isotherms at several temperatures obtained after cooling the sample from 300 to 4.2 K in the presence of a magnetic field of 14 T.

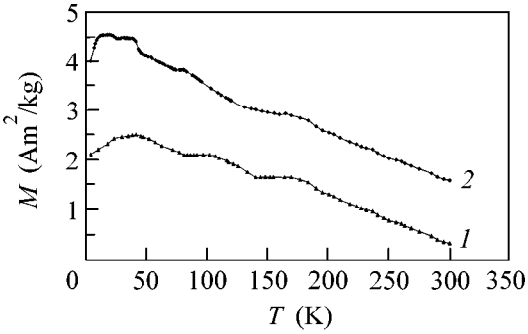

Fig. 5. Temperature dependence of the magnetization in a magnetic field of 10 T obtained (curve *1*) after cooling the sample to 4.2 K in the absence of a magnetic field and (curve *2*) after cooling the sample in a field of 14 T from 300 to 4.2 K.

It is seen in Figs. 3–5 that the spontaneous magnetic moment is observed in the sample even at $T > T_N$, but its magnitude is small. For example, it does not exceed 0.33 μ_B/(chem. unit) at $T = 77$ K for the sample cooled in a field of 14 T and decreases with increasing temperature. Steps are observed in the curves $M(T)$ in the temperature ranges 80–100 K and 140–170 K for the sample cooled in the absence of a field. These steps are smoothed at the same value $H = 10$ T in the curve obtained after cooling the sample from 300 to 4.2 K in a field of 14 T. It is quite possible that, as the temperature increases, the short-range AFM order is disturbed in a region of 100 K. This results in breaking of the exchange coupling between the magnetic clusters described above and the AFM microregions that can quite probably exist above T_N. This in turn facilitates the thermal disordering of the cluster magnetic moments. One can assume that the process of thermal destruction of the ferron or afmon clusters starts at the end of the second step at $T \geq 170$ K. It is seen in Fig. 1 that the magnitude of ρ in this temperature region is small. It is smaller than 10^{-3} Ω m; that is, the material actually becomes a good conductor because of the destruction of magnetic clusters.

This work was supported by the Russian Foundation for Basic Research (project no. 00-15-96695), the Jozef Mianowski Foundation (Poland), and the Committee for Scientific Research (Poland). The authors are grateful to Ya.A. Kessler and D.S. Filimonov for the preparation of the sample and its analysis.

REFERENCES

1. Ya. A. Kesler, L. I. Koroleva, M. G. Mikheev, *et al.*, Neorg. Mater. **29**, 115 (1993).
2. J. Warczewski, J. Kusz, D. S. Filimonov, *et al.*, J. Magn. Magn. Mater. **175**, 299 (1997).
3. S. Methfessel and D. C. Mattis, *Magnetic Semiconductors* (Springer-Verlag, Berlin, 1968; Mir, Moscow, 1972).
4. F. K. Lotgering, Solid State Commun. **2**, 55 (1964).
5. L. I. Koroleva, Ja. A. Kessler, A. G. Odintsov, *et al.*, J. Magn. Magn. Mater. **140–144**, 2015 (1995).
6. É. L. Nagaev, *Physics of Magnetic Semiconductors* (Nauka, Moscow, 1979).
7. É. L. Nagaev, Pis'ma Zh. Éksp. Teor. Fiz. **55**, 646 (1992) [JETP Lett. **55**, 675 (1992)].

Translated by A. Bagatur'yants

JETP Letters, Vol. 72, No. 11, 2000, pp. 565–568. Translated from Pis'ma v Zhurnal Éksperimental'noĭ i Teoreticheskoĭ Fiziki, Vol. 72, No. 11, 2000, pp. 819–824.

Scanning Tunneling Microscopy of the Nonequilibrium Interaction of Impurity States at Semiconductor Surfaces

P. I. Arseev, N. S. Maslova, S. I. Oreshkin, V. I. Panov, and S. V. Savinov*

Moscow State University, Vorob'evy gory, Moscow, 119899 Russia

** e-mail: spm@spmlab.phys.msu.su*

Received November 14, 2000

Interaction of two localized impurity states of Si atoms at a GaAs surface was studied by scanning tunneling microscopy and spectroscopy. The effects of a twofold "switching" on and off of the states of each of the interacting atoms, the tunneling-interaction-induced mutual level pulling of these states, and the level stabilization near E_F were observed. These effects are explained in terms of the extended Anderson model. © *2000 MAIK "Nauka/Interperiodica".*

PACS numbers: 71.55.Eq; 61.16.Ch; 68.65.+g; 68.35.Bs; 73.20.Dx

With a decrease in size and dimensionality of semiconductor electronic systems, impurity states and their interaction start to play the key part in electronic processes. Such states exert a particularly strong effect on the electronic structure of surfaces. The interaction of the impurity states at surfaces or interfaces have been poorly studied to date, while the effects of nonequilibrium interaction of such states have not been examined at all. At the same time, modern trends in the development of semiconductor electronics need a detailed analysis of processes of this kind, because they may become the basis for realizing the elements of semiconductor nanometer-scale electronics in the future.

In this work, the interaction of the localized impurity states formed by a pair of identical impurity Si atoms 3 nm apart at the (110) GaAs surface are studied by scanning tunneling microscopy and spectroscopy (STM/STS) [1]. The sample under investigation was a GaAs single crystal doped with mutually compensating Si and Zn impurities with concentrations 5×10^{18} and 2×10^{19} cm^{-3}, respectively.

Measurements were made at a temperature of 4.2 K on a scanning tunneling microscope allowing the preparation of a clean surface for an *in situ* sample using a cleavage mechanism [2].

The interaction of the impurity states was studied by measuring the tunnel conductance $(dI/dV)/(I/V)$ across a surface area of 10×10 nm with a step of 0.25 nm. In Fig. 1, the measured spatial distribution of local electron density in the vicinity of the interacting impurities *a* and *b* is shown as a function of energies of the key states of these interacting impurity atoms.

Figure 1.1 is the STM image of the interacting Si atoms. The remaining panels show the spatial distribution of the normalized tunnel conductance near the atoms vs. the tunnel bias applied to the STM tip. It should be noted that the contribution from other dopands situated near the chosen interacting Si atoms was observed only in the form of a distributed nonuniform Coulomb potential in the crystal. Due to this potential, the initial state of the interacting Si pair became asymmetric, which showed itself in the distinctions between the STM/STS images of these atoms at zero bias $V_t \approx 0$ on the transition.

In the experimentally observed spatial distribution of the local tunnel conductance, one can recognize a twofold "switching" on and off of each of the atomic *a* and *b* states upon changing the tunnel bias. After switching on, the excess tunnel conductance occurs in the vicinity of each of these atoms in a bias range of ≈0.75 V, which is much greater than the level width of the localized state. At the same time, the transition from one state to the other occurs upon changing bias in the range on the order of 0.15 V, which is comparable to the energy level width of the localized state.

The behavior of the spatial distribution of tunnel conductance in the vicinity of the two impurity atoms was explained using a model that is analogous to the Anderson model [3–5] but takes into account the Coulomb interaction of the localized electrons and the influence of the tunnel bias on the positions of energy levels of the impurity atoms.

A change in the applied bias can induce the transition of an impurity atom from the state corresponding to the "paramagnetic" regime to the state corresponding to the "magnetic" regime (the energy of electrons with different spins and their occupation numbers are different). The interaction of the impurity states with the continuum spectrum is assumed to be not too weak; namely, a change in the energy of impurity states under the action of the Coulomb interaction of the localized charges is determined by the mean occupation numbers at a fixed applied bias. This situation is different from

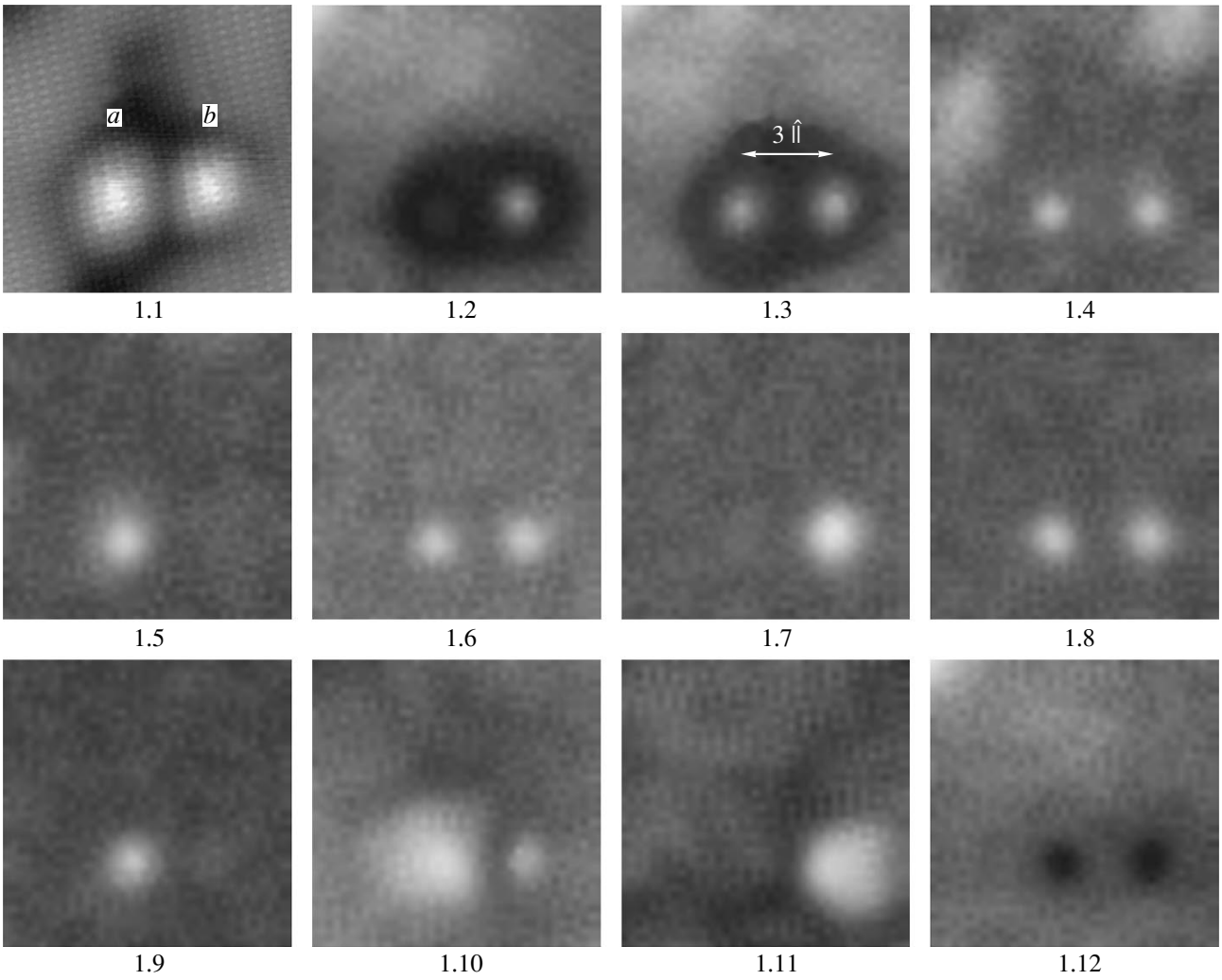

Fig. 1. STM images and image of the normalized tunnel conductance near the interacting impurity silicon atoms *a* and *b*. (1) STM image of atoms at V_t = 1.5 V; (2)–(12) images of the tunnel conductance $\frac{\partial I/\partial V}{I/V}$ at V_t = (2) 2.0, (3) 1.55, (4) 1.4, (5) 1.1, (6) 0.8, (7) 0.55, (8) 0.2, (9) ≈0.0, (10) –0.2, (11) –0.4, and (12) –1.5 V.

the effects caused by a Coulomb blockade associated with the discreteness of the occupation numbers of localized states [7].

Indeed, in the presence of both intra-atomic and interatomic Coulomb interactions, Coulomb blockade [7] gives rise to the peaks in the tunnel conductance as a function of bias on the contact, with the peak widths being on the order of the level width of the localized state (and no larger than 0.1 eV).

In our model, the tunneling interaction between the impurity atoms can redistribute the localized charge between the atoms and lead to mutual energy-level pulling between the localized states in a certain range of applied bias. As a result, the following factors should be taken into account in the analysis of the experimental data:

(1) The excess local tunnel conductance appears in the vicinity of the impurity atom if $|\varepsilon_{a(b)}(V) - E_F| < \Gamma$ (Γ is the width of the atomic localized level). If the applied bias exceeds the level width, $|eV| > \Gamma$, then the local tunnel conductance may increase both when the energy of localized state passes through the Fermi level E_F^S of the sample and when it passes through the Fermi level $E_F^T = E_F^S - eV$ of the tip.

(2) The Coulomb interaction of the localized electrons can be described in the self-consistent mean-field approximation of the Anderson model. This approximation applies when the energy $U_{a(b)}$ of Coulomb interaction of the localized electrons does not strongly exceed its critical value U_{cr}.

As the bias on the contact changes, i.e., as the position of a seed level $\varepsilon_{a(b)}^0(V)$ of an impurity atom changes, the transition from the paramagnetic to the magnetic regime can occur. Thus, the Coulomb interaction of localized electrons in a certain range of applied bias can give rise to two energetically different states for electrons with opposite spins at one of the impurity atoms. On further increase in applied bias, the reverse transition to the paramagnetic state can occur for the impurity atom.

(3) Due to the atomic interaction, the distribution law for the localized charges in the area of STM contact becomes more complex. A sizable redistribution of the localized charge occurs between the atoms, so that the energy levels of one of the atoms can stabilize near the Fermi level of the sample or the tip and the mutual energy-level pulling can take place. For example, in the nonequilibrium situation at nonzero bias V, when the $\varepsilon_a^{-\sigma}(V)$ level is in the vicinity of E_F^S and lies higher than $\varepsilon_b^{\pm\sigma}(V)$, the interaction between atoms a and b brings about charge redistribution between them and strengthening of the magnetic regime for the a atom and, hence, an increase in the separation between the ε_a^{σ} and $\varepsilon_a^{-\sigma}$ levels. If $V_t = 0$, then the interaction between the atoms results in weakening of the magnetic regime for the a atom and equalization of the ε_a^{σ} and $\varepsilon_a^{-\sigma}$ energies.

Let us analyze the experimental results using the suggested model.

At $V \approx 0$, the energy $\varepsilon_a(0)$ of the localized state of atom a is close to the Fermi level E_F^S of the sample. The a atom manifests itself as an enhanced tunnel conductance, i.e., as a light spot in the STS image (Fig. 1.9). In this case, the Coulomb interaction U_a of the localized electrons does not strongly exceed the critical value U_{cr} introduced in the Anderson model and the a atom is in the paramagnetic regime, $\varepsilon_a^{\sigma} = \varepsilon_a^{-\sigma}$ and $\langle n_a^{\sigma} \rangle = \langle n_a^{-\sigma} \rangle$. Under these conditions, the energy $\varepsilon_b(0)$ of the localized state of atom b lies lower than the Fermi level so that the b atom is not seen in the STS image of tunnel conductance. It is assumed that the energy U_b of Coulomb interaction of localized electrons is lower than U_{cr} so that the b atom also occurs in the paramagnetic regime.

As the positive tip voltage rises, the energy of atoms a and b becomes lower due to the external field (applied bias) and, at $V_t \approx 0.15$ V, the energy $\varepsilon_b(V)$ of atom b becomes close to the tip Fermi level E_F^T. As a result, the b atom is switched on and also becomes visible as a light spot in the STS image, while the excess tunnel conductance is retained in the region of atom a (Fig. 1.8). This is due to the fact that a small decrease in the energy of atom a causes transition from the paramagnetic to the magnetic regime at an Anderson impurity, because the energy of on-site Coulomb repulsion does not differ strongly from the critical value. The energies of electrons with opposite spins and their occupation numbers become different:

$$\varepsilon_a^{\pm\sigma} = \varepsilon_a^0 - \alpha V + U_a \langle n_{\mp\sigma}(V) \rangle.$$

As a result of such a transition, one of the occupation numbers $n_{\mp\sigma}(V)$ [$n_{\sigma}(V)$ for definiteness] increases while the other, $n_{-\sigma}(V)$, decreases. This results in a faster decrease of $\varepsilon_a^{\sigma}(V)$, as compared to the case where the dependence of energy on the occupation numbers is not taken into account. Accordingly, $\varepsilon_a^{-\sigma}(V)$ increases while the $\varepsilon_a^{\sigma}(V)$ level stabilizes in the vicinity of the tip Fermi energy. In addition, the difference in the $\varepsilon_a^{\sigma}(V)$ and $\varepsilon_b^{\sigma}(V)$ energies of atoms a and b does not exceed the summarized width of these levels and, hence, the charge redistribution between the atoms becomes appreciable. As the occupation numbers $n_b^{\sigma}(V)$ at the b atom decrease and the $n_a^{\sigma}(V)$ numbers at the a atom simultaneously increase, the energy of the $\varepsilon_a^{-\sigma}(V, n_a^{\sigma})$ state increases and the energy of the $\varepsilon_a^{\sigma}(V, n_a^{-\sigma})$ state further decreases; i.e., the $\varepsilon_a^{\sigma}(V)$ and $\varepsilon_b^{\sigma}(V)$ levels come even closer together. It appears as if the $\varepsilon_a^{\sigma}(V)$ level is pulled into the $\varepsilon_b^{\sigma}(V)$ energy range, while the difference between the energies $\varepsilon_a^{\sigma}(V)$ and $\varepsilon_a^{-\sigma}(V)$ of electrons with opposite spins increases. Thus, excess tunnel conductance occurs in the vicinity of both atoms a and b, as is indeed observed experimentally at biases ranging from ≈0.15 to ≈0.5 V.

On further increase in V_t, the position of the ε_a^{σ} level is mainly determined by the external field because of the smallness of $\langle n_a^{-\sigma} \rangle$. The level with energy $\varepsilon_a^{\sigma}(V)$ moves away from the Fermi level, and the a atom is switched off at $V_t \approx 0.55$ V (Fig. 1.7).

With a change in bias from $V_t \approx 0.55$ to $V_t \approx 0.75$ V, the excess tunnel conductance is seen only in the vicinity of the b atom. The energy of the localized b state is left in the vicinity of the tip Fermi level E_F^T up to $V_t \approx 1.1$ V (Fig. 1.5), where this atom is switched off. Thus, the excess tunnel conductance is retained near the b atom at biases ranging from $V_t \approx 0.2$ to $V_t \approx 1$ V (Figs. 1.5–1.8), because both the Coulomb interaction of localized electrons and the decrease in the mean occupation number upon an increase in the applied bias stabilize the energy of this level in the vicinity of E_F^T. At biases exceeding $V_t \approx 1$ V, a change in the energy of

the localized state of the *b* atom is mainly dictated by the external field.

The *a* atom is again switched on at $V_t \approx 0.8$ V (Fig. 1.6). This is due to a field-induced change in the energy $\varepsilon_a^{-\sigma} = \varepsilon_a^0(0) - \alpha V + U_a\langle n_\sigma\rangle$ of the electron with spin $-\sigma$. The excess tunnel conductance appears in the vicinity of the *a* atom when the level $\varepsilon_a^{-\sigma}(V\langle n_\sigma\rangle)$ falls within the range of width Γ in the vicinity of the Fermi level E_F^S of the sample [i.e., the $\varepsilon_a^{-\sigma}(V)$ level passes through the Fermi level of the sample]. The $\langle n_a^{-\sigma}\rangle$ value starts to increase, making possible a reverse transition of the *a* atom to the paramagnetic regime $\varepsilon_a^\sigma(V) = \varepsilon_a^{-\sigma}(V)$. The dependence of the energy of this localized state on the occupation number results in the stabilization of the $\varepsilon_a^{-\sigma}$ level in the vicinity of the Fermi level of the sample at biases on the contact up to $V_t \approx 1.5$ V. Note that, at biases exceeding $V_t \approx 1.4$ V (Fig. 1.4), the spatial distribution of the tunnel conductance strongly depends on the modification of the band structure of the semiconductor in the vicinity of the impurity atoms (Figs. 1.2, 1.3) [7, 8].

At negative tip voltages, the energies $\varepsilon_a^{\pm\sigma}$ and $\varepsilon_b^{\pm\sigma}$ of atoms *a* and *b* increase. Both atoms *a* and *b* are in the paramagnetic state. At $V_t \approx -0.2$ V, the energy level of the *b* atom passes through the Fermi level E_F^S of the sample, resulting in switching on of the *b* atom (Fig. 1.10). The Coulomb interaction of the localized electrons brings about stabilization of this level in the vicinity of E_F^S at biases up to $V_t \approx -1$ V, as in the case of a positive bias. At $V_t \approx -0.4$ V, the difference between the energy level of the localized state of *a* and the Fermi energy exceeds the width of this level. The *a* atom is switched off (Fig. 1.11). As a result, the excess density of states in the vicinity of the *a* atom disappears.

At negative tip voltages, the excess tunnel conductance is simultaneously seen near both atoms only in the bias range from $V_t \approx -0.2$ to $V_t \approx -0.3$ V. Note that the expansion of the area of electron-density localization in the vicinity of the impurity state with increasing negative bias on the contact is caused by the fact that the energy of the localized state approaches the band edge.

At high negative tip voltages, $V_t < -1$ V, the tunnel conductance is minimum in the vicinity of the *a* and *b* atoms (Fig. 1.12). This is probably due to the fact that, at contact voltages close to the conduction band edge, the local band bending at the semiconductor surface in the vicinity of impurity atoms substantially modifies the tunnel characteristics of the STM transition.

This work was supported in part by the PTN (project no. 97-1086), the SAS (project no. 1.2.99), the MNE (project no. 40.É49), and the Russian Foundation for Basic Research (project nos. 00-02-17759 and 00-15-96555).

REFERENCES

1. N. S. Maslova, V. I. Panov, and S. V. Savinov, Usp. Fiz. Nauk **170** (5), 575 (2000).
2. S. I. Vasil'ev, S. I. Oreshkin, V. I. Panov, *et al.*, Prib. Tekh. Éksp., No. 4, 140 (1997).
3. I. M. Lifshits, S. A. Gredeskul, and L. A. Pastur, *Introduction to the Theory of Disordered Systems* (Nauka, Moscow, 1982; Wiley, New York, 1988).
4. P. W. Andersson, Phys. Rev. **124**, 41 (1961).
5. P. I. Arseev, N. S. Maslova, and S. V. Savinov, Pis'ma Zh. Éksp. Teor. Fiz. **68** (4), 299 (1998) [JETP Lett. **68** (4), 320 (1998)].
6. N. S. Maslova, S. I. Oreshkin, V. I. Panov, *et al.*, Pis'ma Zh. Éksp. Teor. Fiz. **67**, 130 (1998) [JETP Lett. **67**, 146 (1998)].
7. I. H. Ruzin, V. Chandrasekhar, E. I. Levin, *et al.*, Phys. Rev. B **45**, 13469 (1992).
8. A. Depuydt, C. van Haesendonck, N. S. Maslova, *et al.*, Phys. Rev. B **60**, 2619 (1999).

Translated by V. Sakun

JETP Letters, Vol. 72, No. 11, 2000, pp. 569–573. From Pis'ma v Zhurnal Éksperimental'noĭ i Teoreticheskoĭ Fiziki, Vol. 72, No. 11, 2000, pp. 825–831.

Strings in Charge-Transfer Mott Insulators: Effects of Lattice Vibrations and the Coulomb Interaction[1]

A. S. Alexandrov[1] and V. V. Kabanov[2]

[1] *Department of Physics, Loughborough University, Loughborough LE11 3TU, United Kingdom*

[2] *Josef Stefan Institute, 1001 Ljubljana, Slovenia*

Received October 13, 2000

Applying the canonical transformation with the $1/\lambda$ perturbation expansion in the nonadiabatic and intermediate regime and the discrete generalization of Pekar's continuous nonlinear equation in the extreme adiabatic regime, we show that there are no strings in narrow-band ionic insulators due to the Fröhlich electron–phonon interaction alone. The multipolaron system is a homogeneous state in a wide range of physically interesting parameters, no matter how strong the correlations are. At the same time, the Fröhlich interaction allows the antiferromagnetic interactions and/or short-range electron–phonon interactions to form short strings in doped antiferromagnetic insulators if the static dielectric constant is large enough. © *2000 MAIK "Nauka/Interperiodica".*

PACS numbers: 71.38.+i

The electron–phonon interaction is strong in ionic cuprates and manganites, as is established both experimentally [1–4] and theoretically [5–8]. The carriers, doped into the Mott insulator, are coupled with the antiferromagnetic background as well. The antiferromagnetic interactions are thought to give rise to spin and charge segregation (stripes) [9, 10]. There is growing experimental evidence [11–13] that stripes occur in slightly doped insulators. Their theoretical studies have been restricted so far to the repulsive strongly correlated models [9, 10], or to an extreme adiabatic limit of the electron–phonon interaction in narrow- [14, 15] and wide-band [16, 17] polar semiconductors and polymers. On the other hand, there is strong evidence that the nonadiabatic electron–phonon interaction and small polarons are involved in the physics of stripes [3, 12]. Also the role of the long-range Coulomb and Fröhlich interactions remains to be properly addressed.

In this letter, we prove that the Fröhlich electron–phonon interaction, combined with the direct Coulomb repulsion, does not lead to charge segregation like strings in doped narrow-band insulators, both in the nonadiabatic and adiabatic regimes. However, this interaction significantly reduces the Coulomb repulsion, which might allow much weaker antiferromagnetic and/or short-range electron–phonon interactions to segregate charges in the doped insulators, as suggested by previous studies [9, 10, 14].

To begin with, we consider a generic Hamiltonian, including, respectively, the kinetic energy of carriers, the Fröhlich electron–phonon interaction, phonon energy, and the Coulomb repulsion as

$$H = \sum_{i \neq j} t(\mathbf{m}-\mathbf{n})\delta_{s,s'} c_i^\dagger c_j + \sum_{\mathbf{q},i} \omega_{\mathbf{q}} n_i [u_i(\mathbf{q}) d_{\mathbf{q}} + \text{h.c.}] + \sum_{\mathbf{q}} \omega_{\mathbf{q}} (d_{\mathbf{q}}^\dagger d_{\mathbf{q}} + 1/2) + \frac{1}{2}\sum_{i \neq j} V(\mathbf{m}-\mathbf{n}) n_i n_j, \quad (1)$$

with bare hopping integral $t(\mathbf{m})$, and matrix element of the electron–phonon interaction

$$u_i(\mathbf{q}) = \frac{1}{\sqrt{2N}} \gamma(\mathbf{q}) e^{i\mathbf{q}\cdot\mathbf{m}}. \quad (2)$$

Here, $i = (\mathbf{m}, s)$ and $j = (\mathbf{n}, s')$ include the site $\mathbf{m}$, $\mathbf{n}$ and the spin s, s' quantum numbers; $n_i = c_i^\dagger c_i$; c_i and $d_{\mathbf{q}}$ are the electron (hole) and phonon operators, respectively; and N is the number of sites. At large distances (or small q), one finds

$$\gamma(\mathbf{q})^2 \omega_{\mathbf{q}} = 4\pi e^2/\kappa q^2, \quad (3)$$

and

$$V(\mathbf{m}-\mathbf{n}) = e^2/\epsilon_\infty |\mathbf{m}-\mathbf{n}|. \quad (4)$$

The phonon frequency $\omega_{\mathbf{q}}$ and the static and high-frequency dielectric constants in $\kappa^{-1} = \epsilon_\infty^{-1} - \epsilon_0^{-1}$ are those of the host insulator ($\hbar = c = 1$).

[1] This article was submitted by the authors in English.

One can apply the canonical transformation [18] and the $1/\lambda$ multipolaron perturbation theory [5] to integrate out phonons:

$$S = \sum_{\mathbf{q},i} n_i[u_i(\mathbf{q})d_{\mathbf{q}} - \text{h.c.}]. \quad (5)$$

The result is [5, 18]

$$\tilde{H} = e^S H e^{-S} = \sum_{i\neq j} \hat{\sigma}_{ij} c_i^\dagger c_j - E_p \sum_i n_i + \sum_{\mathbf{q}} \omega_{\mathbf{q}}(d_{\mathbf{q}}^\dagger d_{\mathbf{q}} + 1/2) + \frac{1}{2}\sum_{i\neq j} v_{ij} n_i n_j, \quad (6)$$

where

$$\hat{\sigma}_{ij} = t(\mathbf{m}-\mathbf{n})\delta_{s,s'}\exp\left(\sum_{\mathbf{q}}[u_i(\mathbf{q}) - u_j(\mathbf{q})]d_{\mathbf{q}} - \text{h.c.}\right) \quad (7)$$

is the renormalized hopping integral depending on the phonon variables, $E_p = zt\lambda$ is the polaron level shift, and

$$v_{ij} = V(\mathbf{m}-\mathbf{n}) - \frac{1}{N}\sum_{\mathbf{q}} \gamma(\mathbf{q})^2 \omega_{\mathbf{q}} \cos[\mathbf{q}\cdot(\mathbf{m}-\mathbf{n})] \quad (8)$$

is the net interaction of polarons comprising the long-range Coulomb repulsion and the long-range attraction due to ionic lattice deformations. Here, $\lambda = \sum_{\mathbf{q}} \gamma(\mathbf{q})^2\omega_{\mathbf{q}}/2Nzt$ is the dimensionless coupling constant, t is the nearest neighbor hopping integral and z is the coordination lattice number.

The extension of the deformation surrounding (Fröhlich) polarons is large, so their deformation fields overlap at finite density. However, taking into account both the long-range attraction of polarons due to the lattice deformations *and* the direct Coulomb repulsion, the net long-range interaction is repulsive [5]. At distances larger than the lattice constant, $|\mathbf{m}-\mathbf{n}| \geq a \equiv 1$, this interaction is significantly reduced to

$$v_{ij} = e^2/\epsilon_0|\mathbf{m}-\mathbf{n}|. \quad (9)$$

Optical phonons nearly nullify the bare Coulomb repulsion in ionic solids if $\epsilon_0 \gg 1$, which is normally the case in oxides. The kinetic energy term in exact Hamiltonian (6) involves multiphonon events generating a residual *polaron*–phonon interaction [5]. Below, we show that in the two opposite limits, the nonadiabatic ($\omega_{\mathbf{q}} \geq t$) and the extreme adiabatic ($\omega_{\mathbf{q}} \longrightarrow 0$) regimes, there is no charge segregation or any other instability of the polaronic liquid due to the Fröhlich interaction in doped insulators, but only Wigner crystallization at very low densities.

First we consider the nonadiabatic and intermediate regime. The properties of a single small polaron with the Fröhlich electron–phonon interaction were discussed a long time ago [19, 20]. Exact quantum Monte Carlo simulations [21] showed that the first-order $1/\lambda$ perturbation theory is numerically accurate for *any* coupling if the phonon frequency is sufficiently large, $\omega_{\mathbf{q}} > t/2$. The characteristic frequency of phonons strongly coupled with carriers is about $\omega_{\mathbf{q}} = 75$ meV [2] in cuprates, so that cuprates are in this regime. Hence, one can replace the hopping operator in Eq. (6) by its phonon average, reducing the problem to narrow-band fermions with weak repulsive interaction, i.e., Eq. (9). Next-order corrections in $1/\lambda$ increase the polaron binding energy with little effect on the bandwidth [22]. Because the net long-range repulsion is relatively weak, the relevant dimensionless parameter $r_s = m^*e^2/\epsilon_0(4\pi n/3)^{1/3}$ is not very large in doped cuprates. Wigner crystallization appears around $r_s \simeq 100$ or larger, which corresponds to the atomic density of polarons $n \leq 10^{-6}$ with $\epsilon_0 = 30$ and the polaronic mass $m^* = 5m_e$ typical for cuprates and manganites. This estimate shows that small polarons in cuprates and manganites are in the homogeneous state at physically interesting densities.

In the opposite adiabatic limit, one can apply a discrete version of the continuous nonlinear equation [23] proposed in [24] for the Holstein (molecular) model of the electron–phonon interaction and extended to the case of the deformation and Fröhlich interactions in [14, 15]. Applying the Hartree approximation for the Coulomb repulsion, the single-particle wave function $\psi_{\mathbf{n}}$ (the amplitude of the Wannier state $|\mathbf{n}\rangle$) obeys the following equation:

$$-\sum_{\mathbf{m}\neq 0} t(\mathbf{m})[\psi_{\mathbf{n}} - \psi_{\mathbf{n}+\mathbf{m}}] - e\phi_{\mathbf{n}}\psi_{\mathbf{n}} = E\psi_{\mathbf{n}}. \quad (10)$$

The potential $\phi_{\mathbf{n},k}$ acting on a fermion k at the site $\mathbf{n}$ is created by the polarization of the lattice $\phi^l_{\mathbf{n},k}$ and by the Coulomb repulsion with the other $M-1$ fermions, $\phi^c_{\mathbf{n},k}$,

$$\phi_{\mathbf{n},k} = \phi^l_{\mathbf{n},k} + \phi^c_{\mathbf{n},k}. \quad (11)$$

Both potentials satisfy the discrete Poisson equation as

$$\kappa\Delta\phi^l_{\mathbf{n},k} = 4\pi e\sum_{p=1}^{M}|\psi_{\mathbf{n},p}|^2 \quad (12)$$

and

$$\epsilon_\infty\Delta\phi^c_{\mathbf{n},k} = -4\pi e\sum_{p=1,\,p\neq k}^{M}|\psi_{\mathbf{n},p}|^2, \quad (13)$$

with $\Delta\phi_{\mathbf{n}} = \sum_{\mathbf{m}}(\phi_{\mathbf{n}} - \phi_{\mathbf{n}+\mathbf{m}})$. Differently from [15] we include the Coulomb interaction in Pekar's functional J

[23], describing the total energy, in a self-consistent manner using the Hartree approximation, so that

$$J = -\sum_{\mathbf{n},p,\mathbf{m}\neq 0}\psi^*_{\mathbf{n},p}t(\mathbf{m})[\psi_{\mathbf{n},p}-\psi_{\mathbf{n}+\mathbf{m},p}] - \frac{2\pi e^2}{\kappa}\sum_{\mathbf{n},p,\mathbf{m},q}|\psi_{\mathbf{n},p}|^2\Delta^{-1}|\psi_{\mathbf{m},q}|^2 + \frac{2\pi e^2}{\epsilon_\infty}\sum_{\mathbf{n},p,\mathbf{m},q\neq p}|\psi_{\mathbf{n},p}|^2\Delta^{-1}|\psi_{\mathbf{m},q}|^2. \quad (14)$$

If we assume, following [14], that the single-particle function of a fermion trapped in a string of length N is a simple exponent $\psi_n = N^{-1/2}\exp(ikn)$ with periodic boundary conditions, then the functional J is expressed as $J = T + U$, where $T = -2t(N-1)\sin(\pi M/N)/[N\sin(\pi/N)]$ is the kinetic energy (for an *odd* number M of spinless fermions)[2] proportional to t and

$$U = -\frac{e^2}{\kappa}M^2 I_N + \frac{e^2}{\epsilon_\infty}M(M-1)I_N \quad (15)$$

corresponds to the polarization and the Coulomb energies. Here, the integral I_N is given by

$$I_N = \frac{\pi}{(2\pi)^3}\int_{-\pi}^{\pi}dx\int_{-\pi}^{\pi}dy \times \int_{-\pi}^{\pi}dz\frac{\sin(Nx/2)^2}{N^2\sin(x/2)^2}(3-\cos x-\cos y-\cos z)^{-1}. \quad (16)$$

It has the following asymptotic form (figure):

$$I_N = \frac{1.31+\ln N}{N}, \quad (17)$$

which is also derived analytically at large N by the use of the fact that $\sin(Nx/2)^2/(2\pi N\sin(x/2)^2)$ can be replaced by a δ-function. If we split the first (attractive) term in Eq. (15) into two parts through replacing M^2 by $M + M(M-1)$, then it becomes clear that the net interaction between polarons remains repulsive in the adiabatic regime as well, because $\kappa > \epsilon_\infty$. Hence, there are no strings within the Hartree approximation for the Coulomb interaction. Strong correlations do not change this conclusion. Indeed, if we take the Coulomb energy of spinless one-dimensional fermions comprising both Hartree and exchange terms as[3]

$$E_C = \frac{e^2M(M-1)}{N\epsilon_\infty}[0.916+\ln M], \quad (18)$$

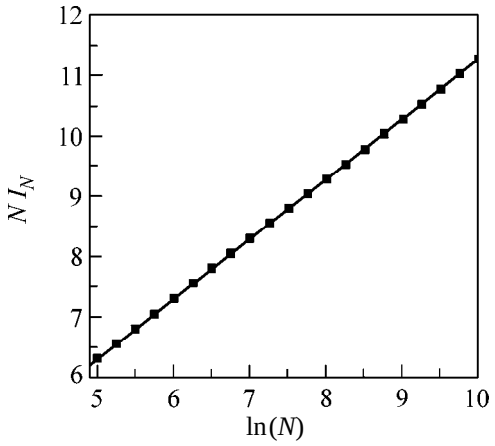

The polarization energy of small Fröhlich polarons trapped in a string depends on its length as $\ln(N)/N$.

the polarization and Coulomb energy per particle becomes (for large $M \gg 1$)

$$\frac{U}{M} = \frac{e^2M}{N\epsilon_\infty}[0.916+\ln M-\alpha(1.31+\ln N)], \quad (19)$$

where $\alpha = 1 - \epsilon_\infty/\epsilon_0 < 1$. Minimizing this energy with respect to the length of the string N, we find

$$N = M^{1/\alpha}\exp(-0.31+0.916/\alpha) \quad (20)$$

and

$$(U/M)_{\min} = -\frac{e^2}{\kappa}M^{1-1/\alpha}\exp(0.31-0.916/\alpha). \quad (21)$$

Hence, the potential energy per particle increases with the number of particles so that the energy of M well-separated polarons is lower than the energy of polarons trapped in a string, whether correlated or not. The opposite conclusion of [15] originates in an incorrect approximation of the integral $I_N \propto N^{0.15}/N$. The correct asymptotic result is $I_N = \ln(N)/N$.

One can argue [25] that a finite kinetic energy (t) can stabilize a string of finite length. Unfortunately, this is not correct either. We performed exact (numerical) calculations of the total energy $E(M, N)$ of M spinless fermions in a string of length N including both kinetic and potential energy with the typical values of $\epsilon_\infty = 5$ and $\epsilon_0 = 30$. The local energy minima (per particle) in a string of length $1 \le N \le 69$ containing $M \le N/2$ particles are presented in the table. Strings with the even fermion numbers carry a finite current and, hence, the local minima are found for odd M. In the extreme wide-band regime with t as large as 1 eV, the global string energy minimum is found at $M = 3$ and $N = 25$ ($E = -2.1167$ eV) and at $M = 3$ and $N = 13$ for $t = 0.5$ eV ($E = -1.2138$ eV). However, this is *not* the ground-state energy in both cases. The energy of well-separated $d \ge 2$-dimensional polarons is well below, less than $-2dt$ per particle (i.e.,

[2] For an *even* M, the kinetic energy $T = -2t(N-1)\sin(\pi M/N)\cos(\pi/N)/[N\sin(\pi/N)]$.

[3] This expression differs from [14, 15] by the numerical coefficients.

$E(M, N)$ for $t = 1$ eV and $t = 0.5$ eV

$t = 1$ eV			$t = 0.5$ eV	
M	N	$E(M, N)$	N	$E(M, N)$
1	11	–2.0328	3	–1.1919
3	25	–2.1167	13	–1.2138
5	42	–2.1166	25	–1.1840
7	61	–2.1127	40	–1.1661

–6 eV in the first case and –3 eV in the second one in the three-dimensional cubic lattice and –4 eV and –2 eV, respectively, in the two-dimensional square lattice). This argument is applied for any values of ϵ_0, ϵ_∞, and t. As a result, we have proved that strings are impossible with the Fröhlich interaction alone, contrary to the erroneous [15, 25].

The Fröhlich interaction is, of course, not the only electron–phonon interaction in ionic solids. As discussed in [5], any short-range electron–phonon interaction, like, e.g., the Jahn–Teller (JT) distortion, can overcome the residual weak repulsion of Fröhlich polarons to form small bipolarons. At large distances, small nonadiabatic bipolarons weakly repel each other due to the long-range Coulomb interaction, which is four times of that of polarons, Eq. (9). Hence, they form a liquid state [5], or bipolaronic–polaronic crystal-like structures [26], depending on their effective mass and density. The fact that the Fröhlich interaction almost nullifies the Coulomb repulsion in oxides justifies the use of the Holstein–Hubbard model [6, 27]. The ground state of the 1D Holstein–Hubbard model is a liquid of intersite bipolarons with a significantly reduced mass (compared with the on-site bipolaron), as shown recently [28]. The bound states of three or more polarons are not stable in this model, thus ruling out phase separation. However, the situation might be different if the antiferromagnetic [9, 10] and JT interaction [29] or any short (but finite)-range electron–phonon interactions are strong enough. Due to long-range nature of the Coulomb repulsion, the length of a string should be finite (see also [12, 14]). One can readily estimate its length by the use of Eq. (8) for any type of short-range electron–phonon interaction. If, e.g., we take dispersive phonons $\omega_{\mathbf{q}} = \omega + \delta\omega(\cos q_x + \cos q_y + \cos q_z)$ with a q-independent matrix element $\gamma(\mathbf{q}) = \gamma$, we obtain a short-range polaron–polaron attraction as

$$v_{att}(\mathbf{n} - \mathbf{m}) = -E_{att}(\delta\omega/\omega)\delta_{|\mathbf{n}-\mathbf{m}|,1}, \qquad (22)$$

where $E_{att} = \gamma^2\omega_0/2$. Taking into account the long-range repulsion as well, Eq. (9), the potential energy of the string with $M = N$ polarons becomes

$$U = \frac{e^2}{\epsilon_0}N^2 I_N - \frac{NE_{att}\delta\omega}{\omega}. \qquad (23)$$

Minimization of this energy yields the length of the string as

$$N = \exp\left(\frac{\epsilon_0 E_{att}\delta\omega}{e^2\omega} - 2.31\right). \qquad (24)$$

Actually, this expression provides a fair estimate of the string length for any kind of attraction (not only generated by phonon dispersion) and also for the antiferromagnetic exchange and/or JT-type of interactions.[4] Due to the numerical coefficient in the exponent in Eq. (24), one can expect only short strings (if any) with the realistic values of E_{att} (about a few hundred millivolts), and the static dielectric constant $\epsilon_0 \leq 100$.

We conclude that there are no strings in ionic doped insulators with the Fröhlich interaction alone. Depending on their density and mass, polarons remain in a liquid state or Wigner crystal. On the other hand, the short-range electron–phonon and/or antiferromagnetic interactions might provide a liquid bipolaronic state and/or charge segregation (strings of a finite length), because the long-range Fröhlich interaction significantly reduces the Coulomb repulsion in highly polarizable ionic insulators.

We greatly appreciate enlightening discussions with Antonio Bianconi, Janez Bonca, Alex Bratkovsky, David Eagles, Pavel Kornilovitch, Fedor Kusmartsev, Dragan Mihailovic, and Jan Zaanen. One of us (V.V.K.) acknowledges support of the work by INTAS grant no. 97-963.

REFERENCES

1. G. Zhao, M. B. Hunt, H. Keller, and K. A. Müller, Nature **385**, 236 (1997).
2. T. Timusk, in *Anharmonic Properties of High-T_c Cuprates*, Ed. by D. Mihailović *et al.* (World Scientific, Singapore, 1995), p. 171.
3. A. Lanzara *et al.*, J. Phys.: Condens. Matter **11**, L541 (1999).
4. D. R. Temprano *et al.*, Phys. Rev. Lett. **84**, 1990 (2000).
5. A. S. Alexandrov and N. F. Mott, Rep. Prog. Phys. **57**, 1197 (1994); *Polarons and Bipolarons* (World Scientific, Singapore, 1995).
6. A. R. Bishop and M. Salkola, in *Polarons and Bipolarons in High-T_c Superconductors and Related Materials*, Ed. by E. K. H. Salje, A. S. Alexandrov, and W. Y. Liang (Cambridge Univ. Press, Cambridge, 1995), p. 353.
7. A. J. Millis, P. B. Littlewood, and B. I. Shraiman, Phys. Rev. Lett. **74**, 5144 (1995).
8. A. S. Alexandrov and A. M. Bratkovsky, Phys. Rev. Lett. **82**, 141 (1999); **84**, 2043 (2000).
9. J. Zaanen and O. Gunnarsson, Phys. Rev. B **40**, 7391 (1989).

[4] $E_{att}\delta\omega/\omega \propto J$ in the case of the antiferromagnetic interaction J and $E_{att}\delta\omega/\omega \propto E_{JT}$ in the case of the JT distortion (E_{JT} is the JT energy).

10. V. J. Emery, S. A. Kivelson, and O. Zachar, Phys. Rev. B **56**, 6120 (1997) and references therein.
11. J. M. Tranquada *et al.*, Nature **375**, 561 (1995).
12. A. Bianconi, J. Phys. IV **9**, 325 (1999) and references therein.
13. V. J. Emery, S. A. Kivelson, and J. M. Tranquada, Proc. Natl. Acad. Sci. USA **96**, 8814 (1999); cond-mat/9907228.
14. F. V. Kusmartsev, J. Phys. IV **9**, 321 (1999).
15. F. V. Kusmartsev, Phys. Rev. Lett. **84**, 530 (2000).
16. L. N. Grigorov, Makromol. Chem., Macromol. Symp. **37**, 159 (1990).
17. L. N. Grigorov *et al.*, Makromol. Chem., Macromol. Symp. **37**, 177 (1990).
18. I. G. Lang and Yu. A. Firsov, Zh. Éksp. Teor. Fiz. **43**, 1843 (1962) [Sov. Phys. JETP **16**, 1301 (1963)].
19. J. Yamashita and T. Kurosawa, J. Phys. Chem. Solids **5**, 34 (1958).
20. D. M. Eagles, Phys. Rev. **181**, 1278 (1969) and references therein.
21. A. S. Alexandrov and P. E. Kornilovich, Phys. Rev. Lett. **82**, 807 (1999).
22. Yu. A. Firsov, V. V. Kabanov, *et al.*, Phys. Rev. B **59**, 12132 (1999).
23. S. I. Pekar, Zh. Éksp. Teor. Fiz. **16**, 335 (1946).
24. V. V. Kabanov and O. Yu. Mashtakov, Phys. Rev. B **47**, 6060 (1993).
25. F. V. Kusmartsev, Phys. Rev. Lett. **84**, 5026 (2000).
26. S. Aubry, in *Polarons and Bipolarons in High-T_c Superconductors and Related Materials*, Ed. by E. K. H. Salje, A. S. Alexandrov, and W. Y. Liang (Cambridge Univ. Press, Cambridge, 1995), p. 271.
27. H. Fehske *et al.*, Phys. Rev. B **51**, 16582 (1995).
28. J. Bonca, T. Katrašnik, and S. A. Trugman, Phys. Rev. Lett. **84**, 3153 (2000).
29. L. P. Gor'kov and A. V. Sokol, Pis'ma Zh. Éksp. Teor. Fiz. **46**, 333 (1987) [JETP Lett. **46**, 420 (1987)].

JETP Letters, Vol. 72, No. 11, 2000, pp. 574–577. Translated from Pis'ma v Zhurnal Éksperimental'noĭ i Teoreticheskoĭ Fiziki, Vol. 72, No. 11, 2000, pp. 832–837.

Rapidly Fluctuating Fields as a Source of Low-Frequency Conductivity Fluctuations and the Size Effects in Quantum Kinetics

Yu. E. Kuzovlev[1], Yu. V. Medvedev[1], and A. M. Grishin[2]

[1] *Donetsk Physicotechnical Institute, National Academy of Sciences of Ukraine, Donetsk, 340114 Ukraine*

[2] *Royal Institute of Technology, Stockholm, Sweden*

Received June 23, 2000; in final form, October 27, 2000

Tunneling contact was taken as an example to demonstrate that the interaction of electron quantum transitions can serve as a source of low-frequency flicker fluctuations of conductivity. Estimates are made for the fluctuations of tunnel conductance. The theory explains the effect of flicker noise sensitivity to the discreteness of the electronic spectrum, as it was observed in nanocomposites. © *2000 MAIK "Nauka/Interperiodica".*

PACS numbers: 72.70.+m

1. Low-frequency flicker noise ($1/f$ noise) is a topical problem of theoretical physics [1–5]. In electronics, it is usually ascribed to the thermally activated fluctuations, e.g., of structural disorder [1–11], while the $1/f$ spectrum is constructed from Lorentzians corresponding to "fluctuators" having different activation energies [1]. However, there is some evidence that does not fit in this theory [2, 4]. The fluctuators in hopping conduction and magnetoresistive oxides [8–12] may well be associated with Coulomb interactions, but the theory cannot explain the fact that the $1/f$ spectrum is not saturated at low frequencies [8]. It appears that "$1/f$ from Lorentzians" is a trouble of the theory [13].

A more universal source of the $1/f$ noise consists in the absence of a characteristic time scale rather than in the summation of times. The former is typical of the dissipative (resistive) kinetic events such as collisions of particles and quanta [4, 14–18]. The fact that the system forgets previous events signifies that there is no distinct "number (probability) of events per unit time," because the fluctuations of (term from [19]) event density (and, hence, dissipation rate) do not bring about the reverse reaction. As a result, the $1/f$ spectrum becomes unsaturated (see reviews [4, 18]). Kinetics throws out this "$1/f$ from memory loss" and postulates probabilities per unit time (collision integrals). However, when going from statistical mechanics to gas kinetics without adopting such an ansatz [15, 18], one arrives at the $1/f$ fluctuations of diffusion rate and molecular mobility. Flicker fluctuations of dissipation and light scattering in quartz are also described by their own statistics of kinetic events (phonon decay and fusion [16]) when it is taken into account that the latter are entangled in time and (phase) space.

It is shown below that the flicker noise in many-electron systems can also be realized through entangling the kinetic events—electron transitions. Theory can obtain it if it concerns a real duration of transitions and, in addition, the discreteness of electronic energy states.

Because of the finite duration of electron transition, it becomes a fragment of a many-body process. After cutting bosonic lines, the quantum transition amplitude is formed under the action of time-dependent fields associated with the other components of the process. For example, the electron transitions through the tunneling contact (along with the thermal motion of a charge at the contact edges) induce fast bias fluctuations on the contact. These fluctuations randomly shift the phases of amplitude increments for the forthcoming transition. This situation was studied in the theory of Coulomb blockade and low-temperature anomalies of current–voltage characteristics [20–22]. Mathematically, analogous problems arise in the theory of mobility of strongly coupled polarons [23].

Evidently, this implies that the transport characteristics, apart from their renormalization, possess specific fluctuations. To our knowledge, this effect has not been considered so far. Being due to the fast noise, it basically differs from the reproducible fluctuations caused by the static disorder in a tunneling microcontact [24]. For clearness, we concentrate on an "ideal" tunneling contact. Note that the $1/f$ noise in "material" contacts [7, 25] is ordinarily assigned to structural factors, so-called two-level systems. The possibilities of the corresponding theory are analyzed in [6].

2. For a bias $U < T/e$ (T is temperature) applied to the tunneling contact, the average charge carried in time Δt and the conductance can be written as

$$\Delta Q = e\frac{Ue}{\delta E}\frac{\Delta t}{\tau_t}, \quad G = \frac{\Delta Q}{U\Delta t}. \tag{1}$$

0021-3640/00/7211-0574$20.00

Here, δE is the distance between the energy levels of electrons in the edges, $Ue/\delta E$ is the effective number of "active" levels involved in the charge transport, and τ_t is the mean hopping time of electrons (time of accumulation of the hopping probability to a level close to unity). Every contact has a finite capacitance C and a finite correlation time $\tau_c = RC \equiv C/G$ of thermal charge fluctuations. Let us demonstrate that tunneling is a very long process; i.e.,

$$\frac{\tau_t}{\tau_c} = \frac{e^2}{C\delta E} \equiv \frac{E_c}{\delta E} \gg 1, \tag{2}$$

even if the Coulomb effects are weak in a trivial sense, $E_c \ll T$. For a flat contact with edge thicknesses w, barrier thickness d, dielectric constant ~20, and standard metallic electronic characteristics, one obtains $\tau_t/\tau_c \approx dw/a^2$, where a is the atomic scale length (on the order of three angstroms).

Therefore, while tunneling, an electron has time to virtually feel multiple changes $u(t)$ in the bias on the contact. In one-electron terms, this means that the transition probabilities are random variables. In a strict many-body theory, the description of the corresponding excess fluctuations of transport current would require four-particle Green's functions [4]. Inasmuch as the corresponding technique is as yet not developed, we attempt to gain insight into the problem using simple methods of tunneling theory.

3. Let $g_{kq} \approx g$ be the tunneling matrix elements, $p_{kq}(\Delta t, U)$ be the transition probabilities from the (left) state k to the (right) state q in time Δt, and $p_k(\Delta t, U) \equiv \sum_q p_{kq}$ be the probability of hopping from the left level k to any right level. According to the theory of quantum chaos, the stochastic behavior is typical of quantum systems, in spite of the fact that the spectrum is discrete [26, 27]. For this reason, we will treat $u(t)$ as a random process. For $\Delta t \sim \tau_t$, perturbation theory is no doubt valid and yields

$$p_{kq} \approx |A_{kq}|^2, \quad A_{kq} \equiv \frac{g_{kq}}{\hbar}\int_0^{\Delta t} \exp(iE_{kq}t/\hbar)Z(t)dt,$$
$$Z(t) = \exp[i\varphi(t)], \quad \varphi(t) = \frac{e}{\hbar}\int_0^t u(t')dt'. \tag{3}$$

Here, $E_{kq} \equiv E_q^+ - E_k + eU$ (plus sign relates to the right edge). Let us introduce the correlation function for the random phase incursion $\varphi(t)$, the coherence time, and the energy "coherence band":

$$K(t_1 - t_2) = \langle Z(t_1)Z^*(t_2)\rangle,$$
$$\tau_{coh} = \int_0^\infty |K(\tau)|d\tau, \quad \Delta E = 2\pi\hbar/\tau_{coh}, \tag{4}$$

where the angular brackets stand for averaging over $u(t)$. The coherence time can easily be estimated when it is considered that $K(t)$ is the phase characteristic function. It can straightforwardly be written at $E_c \ll T$, if $u(t)$ can be approximated by the Gaussian process, to give $\tau_{coh} \sim (\hbar/e)(C/T)^{1/2}$. At $E_c \sim T$, charge quantization is essential and $u(t)$ is approximated by a three-valued process $u = 0, \pm e/C$. An appropriate analysis gives $\tau_{coh} \sim \tau_c$.

Although shunting by an external circuit may increase τ_{coh}, it is clear that this time is much shorter than the observation time; i.e., the $Z(t)$ factor under the integral in Eq. (3) acts as complex fast ("white") noise. Accordingly, the A_{kq} amplitudes behave mainly as (complex) Brownian trajectories. One can thus write

$$\langle p_{kq}^2\rangle = \left\langle |A_{kq}|^4\right\rangle \approx 2\left\langle |A_{kq}|^2\right\rangle^2 = 2\langle p_{kq}\rangle^2,$$
$$\langle p_{kq}, p_{kq}\rangle \approx \langle p_{kq}\rangle^2 \tag{5}$$

(the Malakhov angular brackets with comma inside denote a correlator for the deviations from the mean). Therefore, in times longer than the coherence time, the transition probabilities become completely indeterminate.

Let us consider the summarized hopping probability. It can be presented in the form

$$p_k = \int_0^{\Delta t}\int \Gamma_k(t_1 - t_2)Z(t_1)Z^*(t_2)dt_1dt_2,$$
$$\Gamma_k(\tau) \equiv \sum_q \left(\frac{g_{kq}}{\hbar}\right)^2 \exp(i\tau E_{kq}/\hbar). \tag{6}$$

Omitting details, we emphasize the key role of analytic properties of the kernel $\Gamma_k(\tau)$ for the discrete spectrum. In the case of a continuum spectrum, it would become a function that rapidly and irreversibly tends to zero. In reality, it is highly nonlocal and never decays, returning from time to time to its value at zero time.

Due to discreteness, the hopping probabilities are also random variables. At $\Delta E > \delta E$, one has

$$\langle p_{k_1}, p_{k_2}\rangle \approx \frac{\delta E}{\Delta E}\langle p_{k_1}\rangle\langle p_{k_2}\rangle S(E_{k_1} - E_{k_2}),$$
$$S(E) = \int \exp(iE\tau/\hbar)|K(\tau)|^2 d\tau\left[\int |K(\tau)|^2 d\tau\right]^{-1}. \tag{7}$$

The mean probabilities virtually coincide with those adopted in standard kinetics. According to Eq. (7), a peculiar kind of "uncertainty principle" is fulfilled: although the fluctuations of all hopping probabilities decrease with increasing ΔE, the energy range of their correlation is extended. At $\Delta E < \delta E$, the results depend on the structure (commensurability) of electronic spectra in the edges so that the level statistics should be invoked. In this extreme case, the fluctuations may

increase by one hundred percent and higher. In addition, the mean probabilities (and, hence, the current–voltage characteristics) undergo substantial noise-induced renormalization.

4. Let us consider the fluctuations of a charge carried through a contact between the terminals of an external circuit and assume that $T \gg \delta E$. Now let ΔQ denote a random variable. It consists of two parts, $\Delta Q = \Delta Q_{th} + \Delta Q_{ex}$, where the first term is the contribution from the fast thermal (shot) noise. It can easily be estimated to give $\langle \Delta Q_{th}^2 \rangle \approx 2TG\Delta t$. The second term includes the transport excess fluctuations caused by the fluctuations of transition probabilities. Statistically, ΔQ_{ex} should be defined as a conditional mean of ΔQ at a fixed p_{kq}. It is clear from thermodynamic considerations that this term coincides in sign with the external voltage U and vanishes at $U = 0$. Consequently, it can be represented as a result of "excess" unidirectional jumps:

$$\Delta Q_{ex} = e\sum_{j=1}^{n} p_{k_j}(\Delta t, U). \tag{8}$$

Here, n is the random number of active levels from which this hopping occurs. The mean n value is $N \equiv eU/\delta E$.

A "one-particle" energy distribution of active levels is specified by Fermi statistics in both contact edges:

$$W(E) = [f(E) - f(E + eU)]/eU \approx -\partial f(E)/\partial E,$$

where $f(E)$ is the Fermi distribution function. Averaging of Eq. (8) with this distribution function leads to the usual formula for tunnel current and to Eq. (1). A "two-particle" (pair) distribution that is necessary for calculating the dispersion of Eq. (8) is determined by the one-particle distribution and by the fact that two active levels cannot coincide with each other. If the levels are numbered in the order of increasing energy, then the distance between the levels $j > i$ cannot be smaller than $\approx (j - i)\delta E$. For this reason, the pair distribution function has the form

$$W_{ij}(E', E'') \approx W(E')W(E'')\vartheta(|E'' - E'| - |j - i|\delta E), \tag{9}$$

where $\vartheta()$ is the step function.

We omit the calculations of the dispersion of Eq. (8) and the corresponding fluctuations of conductance $G = \Delta Q_{ex}/U\Delta t$. For a short coherence time ("large" contact, $\Delta E > \delta E$), the results following from Eqs. (7)–(9) have the form (at $U < T/e$)

$$\delta G^2 \equiv \frac{\langle G, G\rangle}{\langle G\rangle^2} \approx \frac{\delta E}{T} D(eU),$$
$$D(X) \equiv \frac{1}{X}\int_0^X dE \int_E^\infty S(E')dE' \left[\int_0^\infty S(E)dE\right]^{-1}. \tag{10}$$

At long coherence times ("small" contacts, $\Delta E < \delta E$), the extreme situation occurs (see above) for which the fluctuations can be sizably larger than (10), up to $\delta G^2 \sim 1$.

One can see that the discreteness generally serves as a direct measure of conductance fluctuations. The factor ΔE characterizes the ambient noise and comes into operation when the effective number $eU/\Delta E$ of statistically independent electron tunneling (energy) channels exceeds unity and, according to Eq. (10), the relative fluctuations decrease approximately inversely with the number of channels.

Note that the transparency dropped out of Eq. (10). As for the ratio "excess transport noise/shot noise," it is determined by the product of the transparency and the observation time. For this reason, the excess noise inevitably dominates at long times and low frequencies. At $eU \sim T$, this occurs in time on the order of τ_t. Hence, as regards noise, the transparency is not a small parameter [the more so as the random phase $\varphi(t)$ depends on it in a complex nonperturbative manner].

5. In [25], $1/f$ noise was studied for Ni-Al_2O_3 nanocomposite films. Parameters of a typical tunneling contact between the neighboring metal grains were as follows: $\delta E \approx 0.2$ meV, $E_C \sim T$ (room temperature), $R \approx 30$ MΩ, $\tau_c \approx 1.5 \times 10^{-10}$ s, and $\tau_t \approx 3 \times 10^{-8}$ s. Conductance fluctuations with relative spectral density $S_{\delta G}(f) \approx \alpha/N_g f$ were observed for the sample, where $\alpha \approx 6 \times 10^{-3}$ and N_g was the number of grains in the sample.

This noise corresponds to the conductance fluctuations $S_{\delta G}(f) \sim \alpha/f$ for the elementary contact. Since inequality (2) is well fulfilled, we assume that this noise is caused by the mechanism under discussion. The relation between the dispersion and spectrum of stationary noise includes the logarithm of the observation time, $\delta G^2 \sim \alpha \ln(\Delta t/\tau_c)$. At $\Delta t \sim \tau_t$, this is equal to ~0.03. For $\delta E = 0.2$ meV and room temperature, Eq. (10) gives ≈0.008. The agreement is good, when it is considered that we are in the extreme situation; according to the above estimates, ΔE in this case is on the order of δE or smaller.

A remarkable observation made in [25] was that the $1/f$ noise was sensitive to the discreteness of electronic spectra in grains. When the applied bias per elementary contact exceeded $\delta E/e$, the noise intensity decreased inversely with the bias, although the current–voltage characteristic remained ohmic up to voltages higher by a factor of $T/\delta E \sim 100$. As regards this effect, the theory presented above fully agrees with experiment.

6. Level discreteness in nanocomposites is dictated by the volume of metal particles. Evidently, the δE value in a massive contact is also determined by the volume of a region that is physically accessible to hopping, i.e., by the geometry of the contact and the electron interaction and scattering in the edges. At not-too-low temperatures, the accessible volume is bounded by

the contact area A and the inelastic mean free path λ in the edges (electrodes). In other words, this is a volume where the level sparseness is on the order of level broadening due to the inelastic relaxation (of course, it would now be more appropriate to speak about levels in terms of the statistics of electronic states [26, 27]).

Thus, one can write $\delta E \sim E_F a^3/A\lambda$ for the massive metallic edges, where E_F is the Fermi energy. Making use of the relation between λ and edge conductivities, $\sigma \sim \lambda/a^2 R_0$ and $R_0 \equiv 2\pi\hbar/e^2$, one derives the following estimate from Eq. (10):

$$\delta G^2 \sim \frac{E_F}{T}\frac{a^2}{A}\frac{\sigma_{\min}}{\sigma}, \tag{11}$$

where $\sigma_{\min} \sim (aR_0)^{-1}$ is the minimum value of metallic conductivity. In particular, let the metal be pure to an extent that phonon relaxation prevails. Then, as is known [28], $\sigma \propto (T_D/T)^5$ so that one can expect that the fluctuations of contact conductance at temperatures below the Debye temperature are proportional to T^4.

For the standard E_F values, one has, by order of magnitude, $\delta G^2 \sim (a^2/A)\,(T/T_D)^4$. Using again the relationship between the dispersion and the coefficient of $1/f$ and assuming $T \sim T_D$, one arrives at the estimate $fS_{\delta G}(f) \sim 10^{-7}$ for the microcontact with area 10^{-9} cm^2 examined in [7]. This value agrees with the measurements made in [7] at 260 K. A fast increase (by approximately two orders of magnitude) in the noise, observed in [7] upon elevation of the temperature from 100 to 300 K, can also be naturally explained. It appears that two types of noise were observed: the structural noise dominated below 100 K, while the other (considered in this work) dominated above this temperature and provided the "residual" low-temperature $1/f$ component that was also observed in [7].

7. We assumed in this work that, even in the presence of noise, the result of quantum evolution is determined by the interplay of amplitudes (rather than intermediate probabilities). For this reason, the flicker character of the conductance fluctuations should be retained in a more formal theory (it is a separate problem to prove this statement).

This work was supported by the Ministry of Education and Science of Ukraine (project no. 2M/71-2000) and the Royal Academy of Sciences of Sweden.

REFERENCES

1. P. Dutta and P. Horn, Rev. Mod. Phys. **53** (3), 497 (1981).
2. F. N. Hooge, T. G. M. Kleinpenning, and L. K. J. Vandamme, Rep. Prog. Phys. **44**, 481 (1981).
3. M. B. Weissman, Rev. Mod. Phys. **60**, 537 (1988).
4. G. N. Bochkov and Yu. E. Kuzovlev, Usp. Fiz. Nauk **141**, 151 (1983) [Sov. Phys. Usp. **26**, 829 (1983)].
5. G. P. Zhigal'skiĭ, Usp. Fiz. Nauk **167**, 623 (1997) [Phys. Usp. **40**, 599 (1997)].
6. Yu. M. Gal'perin, V. G. Karpov, and V. I. Kozub, Zh. Éksp. Teor. Fiz. **95**, 1123 (1989) [Sov. Phys. JETP **68**, 648 (1989)].
7. C. T. Rogers and R. A. Buhrman, Phys. Rev. Lett. **53**, 1272 (1984).
8. V. I. Kozub, Solid State Commun. **97**, 843 (1996).
9. B. Raquet, J. M. D. Coey, S. Wirth, and S. von Molnár, Phys. Rev. B **59**, 12435 (1999).
10. A. Lisauskas, S. I. Khartsev, and A. M. Grishin, J. Low. Temp. Phys., *Proceedings of MOS-99.*
11. A. Lisauskas, S. I. Khartsev, *et al.*, Mater. Res. Soc. Symp. Proc., *Spring-99 Meeting.*
12. V. Podzorov, M. Uehara, M. E. Gershenson, and S.-W. Cheong, cond-mat/9912064.
13. J. L. Tandon and H. P. Bilger, J. Appl. Phys. **47**, 1697 (1976).
14. Yu. E. Kuzovlev and G. N. Bochkov, Izv. Vyssh. Uchebn. Zaved., Radiofiz. **26**, 310 (1983); **27**, 1151 (1984).
15. Yu. E. Kuzovlev, Zh. Éksp. Teor. Fiz. **94** (12), 140 (1988) [Sov. Phys. JETP **67**, 2469 (1988)].
16. Yu. E. Kuzovlev, Zh. Éksp. Teor. Fiz. **111**, 2086 (1997) [JETP **84**, 1138 (1997)].
17. Yu. E. Kuzovlev, Phys. Lett. A **194**, 285 (1994).
18. Yu. E. Kuzovlev, cond-mat/9903350.
19. N. S. Krylov, *Works on Foundation of Statistical Physics* (Akad. Nauk SSSR, Moscow, 1950).
20. Yu. V. Nazarov, Zh. Éksp. Teor. Fiz. **95**, 975 (1989) [Sov. Phys. JETP **68**, 561 (1989)].
21. M. H. Devoret, D. Esteve, H. Grabert, *et al.*, Phys. Rev. Lett. **64**, 1824 (1990).
22. S. M. Girvin, L. I. Glazman, M. Jonson, *et al.*, Phys. Rev. Lett. **64**, 3183 (1990).
23. I. G. Lang and Yu. A. Firsov, Zh. Éksp. Teor. Fiz. **43**, 1843 (1962) [Sov. Phys. JETP **16**, 1301 (1963)].
24. A. van Oudenaarden, M. H. Devoret, E. H. Visscher, *et al.*, Phys. Rev. Lett. **78**, 3539 (1997).
25. J. V. Mantese, W. I. Goldburg, D. H. Darling, *et al.*, Solid State Commun. **37**, 353 (1981).
26. G. Casati and B. Chirikov, *Fluctuations in Quantum Chaos*, Preprint, IyaF (Budker Inst. of Nuclear Physics, Siberian Division, Russian Academy of Sciences, 1993).
27. C. W. J. Beenakker, Rev. Mod. Phys. **69**, 731 (1997).
28. E. M. Lifshitz and L. P. Pitaevskiĭ, *Physical Kinetics* (Akad. Nauk SSSR, Moscow, 1974; Pergamon, Oxford, 1981).

Translated by V. Sakun

JETP Letters, Vol. 72, No. 11, 2000, pp. 578–582. From Pis'ma v Zhurnal Éksperimental'noĭ i Teoreticheskoĭ Fiziki, Vol. 72, No. 11, 2000, pp. 838–844.

Scaling and Crossover to Tricriticality in Polymer Solutions*

M. A. Anisimov[1], V. A. Agayan[1], and E. E. Gorodetskiĭ[1,2]

[1] *Institute for Physical Science and Technology and Department of Chemical Engineering, University of Maryland, College Park, MD 20742, USA*

[2] *Oil and Gas Research Institute, Russian Academy of Sciences, Moscow, 117971 Russia*

Received November 4, 2000

We propose a scaling description of phase separation of polymer solutions. The scaling incorporates three universal limiting regimes: the Ising limit asymptotically close to the critical point of phase separation, the "ideal gas" limit for the pure solvent phase, and the tricritical limit for the polymer-rich phase asymptotically close to the *theta* point. We have also developed a phenomenological crossover theory based on the near-tricritical-point Landau expansion renormalized by fluctuations. This theory validates the proposed scaled representation of experimental data and crossover to tricriticality. © *2000 MAIK "Nauka/Interperiodica".*

PACS numbers: 64.75.+g; 61.25.Hq; 05.70.Jk

Phase separation in solutions of polymers in low-molecular-weight (monomer-like) solvents changes dramatically with an increase in the degree of polymerization (Fig. 1) [1]. As in simple binary liquids, asymptotically close to the critical point, the coexistence curves obey a universal power law of the form

$$\phi - \phi_c = \pm B_0|\tau|^{\beta}, \qquad (1)$$

where ϕ is the volume fraction of polymer; ϕ_c is the critical volume fraction; $\tau = (T - T_c)/T$; T is the temperature, T_c is the critical temperature; $\beta = 0.326 \pm 0.001$ is a universal 3-dimensional (3D) Ising critical exponent [2]; and B_0 is a system-dependent critical amplitude. However, with an increase in the polymer molecular weight, the range of validity of the symmetric parabolic-like behavior given by Eq. (1) shrinks, yielding an asymmetric anglelike coexistence boundary near the theta point [3] (Fig. 1). Physically, it means that, in the limit of infinite molecular weight (upon approaching the theta point), the critical amplitude B_0 and the range of 3D Ising behavior vanish.

Qualitatively, the phenomenon of separation of a polymer solution into two coexisting phases was explained long ago by Flory [3]. According to the Flory theory, the dependence of the critical temperature T_c and the critical volume fraction ϕ_c of the polymer on the degree of polymerization N is $T_c = \Theta/(1 + 1/\sqrt{N})^2$ and $\phi_c = 1/(1 + \sqrt{N})$, where Θ is the theta temperature. As elucidated by Widom [4], for any value of the scaling variable $x = \frac{1}{2}\tau\sqrt{N}$ (where N is assumed to be large and τ to be small), the phase coexistence in the Flory system can be represented in terms of a scaling form. The concentration difference $\phi'' - \phi'$, where ϕ'' and ϕ' are the volume fractions of polymer in the concentrated and dilute phases, respectively, is given by

$$\sqrt{N}(\phi'' - \phi') \sim \begin{cases} 2\sqrt{6x} & (x \longrightarrow 0) \\ 3x & (x \longrightarrow \infty). \end{cases} \qquad (2)$$

Although Eq. (2) yields the anglelike coexistence in the theta point limit ($x \longrightarrow \infty$), it violates Eq. (1) in the critical-point limit ($x \longrightarrow 0$). The reason is well known: the Flory theory is essentially a mean-field theory which, just like the van der Waals theory of simple fluids, ignores critical fluctuations. It is possible to modify the Flory model to include critical fluctuations, which does indeed predict both the critical and the theta point limits correctly, as well as the crossover between them [5]. However, restrictions implied by the Flory model for the system-dependent parameters (even after incorporating the fluctuations), especially for the dependence of these parameters on the degree of polymerization, are too stringent to apply the model to real systems.

An attempt to describe the data shown in Fig. 1 by a generalized form of Eq. (2) with $\sqrt{N}$ replaced by ϕ_c^{-1}, $\sqrt{x}$ by x^{β} in the limit $x \longrightarrow 0$, and x by $(T_c - T)/(\Theta - T_c)$ in both limits, was made by Isumi and Miyake [6]. A practical disadvantage of this approach is that, when

* This article was submitted by the authors in English.

T_c is close to the theta temperature (large x), even small changes in Θ (which is not a directly obtainable parameter) cause dramatic changes in x, making the scaling representation extremely sensitive to the choice of Θ.

In this letter, we propose a general scaling description of phase separation in polymer solutions. Experiments have shown that ϕ_c does not satisfy the dependence on the degree of polymerization implied by the Flory theory [7]. The description we propose is not based on any specific molecular model and does not incorporate any particular dependence of the critical parameters on the degree of polymerization. Instead, it uses experimentally well-defined variables, namely, the reduced temperature distance to the critical point τ and the critical volume fraction ϕ_c. Furthermore, to obtain an explicit form of the scaling function, we have developed a crossover theory by incorporating fluctuations into a Landau expansion near the tricritical point. Furthermore, we will elucidate the physical nature of the crossover phenomena: very close to the critical phase-separation point, the correlation length of the concentration fluctuations becomes much larger than the polymer molecular size (radius of gyration) and the system exhibits universal 3D Ising behavior. Very close to the theta point, the radius of gyration becomes larger than the correlation length and the system exhibits tricritical mean-field behavior [8].

We assume that a polymer solution can be described by a scaling function $y(z)$ with three universal limits

$$y(z) = \begin{cases} \pm Kz^{\beta} & (z \longrightarrow 0) \\ \dfrac{1}{2}z & (z \longrightarrow \infty, \text{polymer is rich phase}) \\ 1 & (z \longrightarrow \infty, \text{solvent is rich phase}), \end{cases} \quad (3)$$

where

$$y = A(\phi - \phi_c)/B_0\phi_c^{\beta}, \quad z = C|\tau|/\phi_c, \quad (4)$$

and $K = AC^{-\beta}$, with A and C being the system-dependent coefficients. The coefficient C defines the limiting ($M_w \longrightarrow \infty$) slope of the phase-separation boundary (Fig. 1). The coefficient A can be obtained from a linear correlation between the asymptotic amplitude B_0 and $\phi_c^{1-\beta}$ (insert in Fig. 1) for high-molecular-weight polymers (small ϕ_c), so that $y = (\phi - \phi_c)/\phi_c$ in this limit. The coefficient A becomes a weak function of ϕ_c for lower molecular weights and thus allows for incorporating nonasymptotic regular effects. The Ising limit in Eq. (3) will be perfectly universal for different systems if the coefficient $K = A/C^{\beta}$ is not system-dependent. Although there is no theoretical proof for such universality, for the three polymer solutions we have analyzed, the combination $AC^{-\beta}$ turns out to be the same.

In Fig. 2 we show coexistence-curve data obtained by Dobashi *et al.* [1] for polystyrene in methylcyclohexane, by Xia *et al.* [9] for polymethylmethacrylate in 3-octanone, and by Nakata *et al.* [10] for polystyrene in cyclohexane, scaled according to Eq. (3). We see that all data points collapse onto a single master curve. In Fig. 3, a crossover from critical Ising behavior (for $z \ll 1$) to the theta behavior (for $z \gg 1$) is clearly seen. As z increases, the volume fraction ϕ' of the solvent-rich phase goes to zero (the "ideal-gas" limit), while the volume fraction ϕ''/ϕ_c of the polymer-rich phase tends to its theta limit $\frac{1}{2}z$, indicated in Fig. 3 by the dashed line. The slope of the dashed line on a double logarithmic scale corresponds to the tricritical value $\beta = 1$.

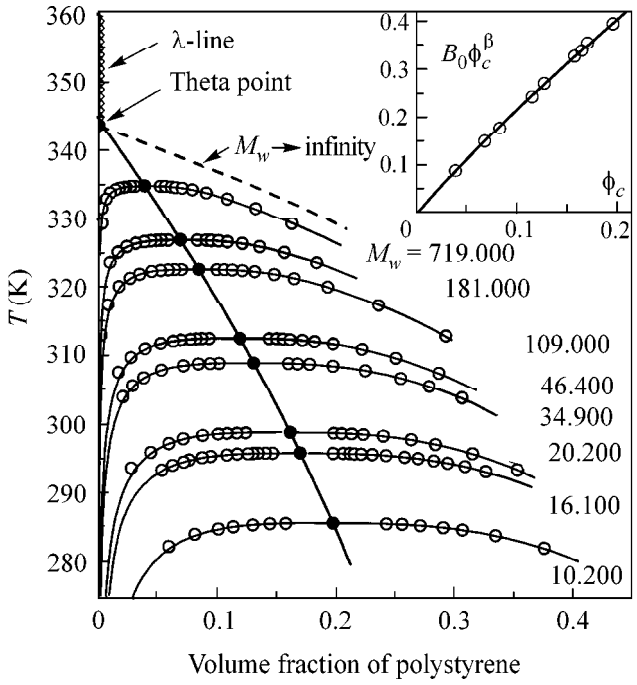

Fig. 1. Phase-coexistence curves for solutions of polystyrene of various molecular weights M_w in methylcyclohexane. Symbols indicate experimental data by Dobashi *et al.* [1]. The insert shows dependence of the critical amplitude B_0 on the critical concentration. Solid curves represent the crossover theory.

De Gennes [11] has pointed out that the theta point in the polymer–solvent system is a tricritical point. A tricritical point is a point which separates lines of second-order (λ-line) and first-order transitions. The states above the theta temperature on $\phi = 0$ (shown by the cogged line in Fig. 1) correspond to the critical-like self-avoiding-walk singularities associated with the behavior of long ($N \longrightarrow \infty$) polymer molecules at infinite dilution [11, 12]. This λ-line is associated with an n-component vector order parameter (ψ) in the limit $n \longrightarrow 0$ [11]. The field h, conjugate to the order parameter, is zero along the λ-line but it becomes nonzero for finite degrees of polymerization. The correlation length associated with the order parameter is the radius of gyration, which diverges in the limit of infinite degree

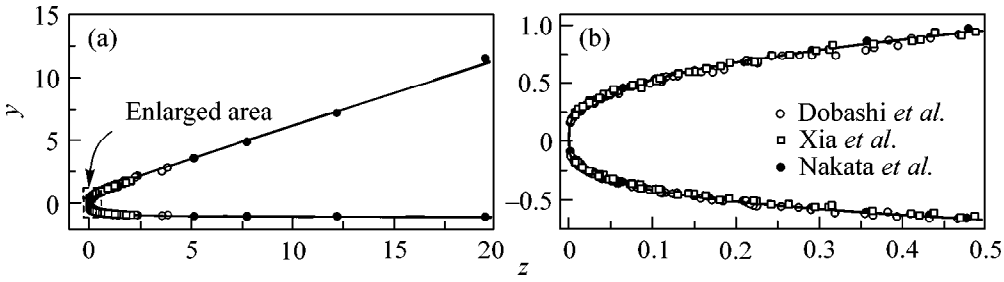

Fig. 2. Universal scaled coexistence curve of polymer solutions: (a) the entire range and (b) the critical region. Solid line is calculated from the crossover theory.

of polymerization (zero field). Below the theta (tricritical) point, the polymer order parameter exhibits a discontinuity accompanied by phase separation and by a discontinuity in the concentration of the polymer. The line of critical phase-separation points shown in Fig. 1 is a nonzero-field critical ("wing") line originating from the tricritical point. The order parameter for the fluid–fluid phase separation, associated with the concentration ϕ, and the polymer order parameter ψ belong to different classes of universality. Tricriticality emerges as a result of a coupling between these two order parameters and exhibits mean-field behavior with small logarithmic corrections [13]. Physically, ψ is proportional to the concentration of end points of the polymer chain, while the concentration ϕ is proportional to $|\psi|^2$ [11]. Therefore, a proper description of the phase separation near the tricritical point should incorporate a crossover between Ising critical behavior and (almost) mean-field tricritical behavior.

To obtain an explicit form of the proposed scaling description, we start with the Landau expansion of the critical part of the dimensionless thermodynamic potential $\Delta\tilde{\Omega}$ of a two-component system in the vicinity of the tricritical point in powers of the order parameter ψ [14]:

$$\Delta\tilde{\Omega} = \tilde{\tau}\psi^2 - \lambda\psi^4 + \nu\psi^6 - h\psi, \qquad (5)$$

where h is the ordering field; $\tilde{\tau} = a(\Delta\tilde{\mu} + b\Delta\tilde{T})$ is the temperature-like scaling field; $\Delta\tilde{T} = (T - \Theta)/T$, with Θ being the tricritical (theta) temperature; $\Delta\tilde{\mu} = \tilde{\mu} - \tilde{\mu}_\Theta$, with $\tilde{\mu} = (\mu_2/\nu_2 - \mu_1/\nu_1)/RT$ being the reduced polymer/solvent chemical potential difference, ν_2 and ν_1 the corresponding molecular volumes, and $\tilde{\mu}_\Theta$ the value of the chemical potential at the tricritical (theta) point; and $\lambda = \lambda_0\Delta\tilde{\mu}$; a, b, λ_0, and ν are system-dependent parameters. The conditions $h = 0$ and $\tilde{\tau} = 0$ determine the λ-line. At the tricritical point, the coefficient λ changes its sign, being negative along the λ-line above Θ and positive below Θ.

The equilibrium values ψ' and ψ'' of the order parameter are found from the conditions $(\partial\Delta\tilde{\Omega}/\partial\psi)_{T,h} = 0$ and $\Delta\tilde{\Omega}(\psi') = \Delta\tilde{\Omega}(\psi'')$. The concentration (volume fraction) ϕ is related to the polymer order parameter ψ by

$$\phi = \left(\frac{\partial\Delta\tilde{\Omega}}{\partial\Delta\tilde{\mu}}\right)_{T,h} = a\psi^2 - \lambda_0\psi^4. \qquad (6)$$

In the limit of infinite degree of polymerization ($h = 0$), we find for the limiting phase-separation boundary shown by the dashed line in Fig. 1

$$\phi' = 0, \quad \phi'' = \frac{\lambda_0 a}{2\nu} b|\Delta\tilde{T}|\left[1 - \frac{\lambda_0^2}{4\nu a} b|\Delta\tilde{T}|\right]. \qquad (7)$$

At nonzero h, a phase separation (wing) critical line emerges, defined by

$$\psi_c^2(h) = \frac{1}{4}\left(\frac{2h}{\nu}\right)^{2/5} \simeq \phi_c/a, \qquad (8)$$

$$T_c(h) = \Theta\left\{1 + \frac{5\nu}{\lambda_0 ab}[a\psi_c^2(h) - 3\lambda_0\psi_c^4(h)]\right\}^{-1}. \qquad (9)$$

Asymptotically, the ratio of the slopes of the limiting ($h = 0$) phase-separation boundary to the critical wing line is universal in the Landau expansion and equal to 5/2. A comparison between the results obtained from Landau expansion (5) and from the mean-field Flory model at $N \gg 1$ has shown that the ordering field h can be identified with the degree of polymerization N as $(2h/\nu)^{-2/5} \sim \sqrt{N}$. Consequently, the near-tricritical Landau model satisfies the mean-field scaling given by Eq. (2).

The Landau theory does not include fluctuations and does not recover the 3D Ising limit exhibited by real polymer systems. Therefore, we have modified expansion (5) using the crossover procedure based on the renormalization group matching method (see [5] and references therein). The details of the calculations will be published elsewhere. The key point of the approach amounts to representing the polymer order parameter as a sum of a regular ψ_0 and a "critical" $\delta\psi$ part $\psi = \psi_0 + \delta\psi$ and rewriting expansion (5) in terms of $\delta\psi$. The critical part is expressed in terms of the distance to the critical temperature (at a certain field h) $\tau = [T -$

$T_c(h)]/T$. The crossover procedure is implemented by replacing the temperature variable τ and the order parameter $\delta\psi$ in the corresponding Landau expansion with renormalized quantities $\tau_\times$ and $\delta\psi_\times$, respectively, such that [5]

$$\tau_\times = \tau Y^{-\alpha/2\Delta_s}, \quad \delta\psi_\times = \delta\psi Y^{(2\gamma-3\nu)4/\Delta_s}, \qquad (10)$$

where α, γ, ν, and Δ_s are universal critical exponents with the following 3D Ising values adopted in this work: $\alpha = 0.11$, $\gamma = 1.239$, $\nu = 0.630$, and $\Delta_s = 0.51$ [2, 5]. The crossover function Y is to be determined from the equation

$$1 - (1 - \bar{u})Y = \bar{u}[1 + (\Lambda/\kappa)^2]^{1/2} Y^{\nu/\Delta_s}, \qquad (11)$$

where $\bar{u}$, a normalized coupling constant roughly independent of h, and $\Lambda = \Lambda_0(2h/v)^{2/5}$, a dimensionless "cutoff" wavenumber assumed to be inversely proportional to the radius of gyration R_G, are two crossover parameters. The parameter κ is inversely proportional to the correlation length and serves as an effective distance to the critical point. In the simplest approximation,

$$\kappa^2 = -2c_t \tau Y^{(2\nu-1)/\Delta_s}, \qquad (12)$$

where the parameter $c_t = c_{t0}(2h/v)^{2/5}$ is associated with the amplitude $\bar{\xi}_0$ of the mean-field correlation length $\bar{\xi}$. Close to the critical point, $Y \longrightarrow (\kappa/\bar{u}\,\Lambda)^{\Delta_s/\nu} \longrightarrow 0$ and the thermodynamic properties exhibit 3D Ising asymptotic behavior. Far away from the critical point, $Y \longrightarrow 1$ and mean-field expansion (5) is recovered. The crossover temperature ("Ginzburg number") $\tau_0 \sim (\bar{u}\,\Lambda)^2/c_t = [(\bar{u}\,\Lambda_0)^2/c_{t0}](2h/v)^{2/5} \sim \phi_c$ vanishes at the theta (tricritical) point. The physical origin of the crossover to tricriticality is a competition between the radius of gyration R_G and the correlation length ξ, since $\Lambda/\kappa \sim \xi/R_G$, while the parameter $\Lambda^2/c_t \sim (\bar{\xi}_0/R_G)^2$ defines the crossover temperature τ_0. Specific N-dependences of the Ising critical amplitudes, predicted by de Gennes' scaling [7, 11], can also be obtained from our theory with the assumption $(2h/v)^{-2/5} \sim \sqrt{N}$.

We have applied the renormalized (crossover) Landau model to describe the experimental data [1, 9, 10] on phase separation in polymer systems and obtained excellent agreement (solid lines in Figs. 1–3). The description of all the systems with a variety of degrees of polymerization requires only four nonuniversal parameters, namely a, λ_0, $C = \lambda_0 a/v$, and the "bare" crossover temperature $\sim(\bar{u}\,\Lambda_0)^2/c_{t0}$, which do not depend on molecular weight. Moreover, the combination $(\bar{u}\,\Lambda_0)^2/c_{t0}$ and $AC^{-\beta}$ can be taken to be the same within the available experimental resolution not only for different molecular weight samples, but also for different substances. This feature makes the solid curves in Figs. 2 and 3 truly universal for all systems studied.

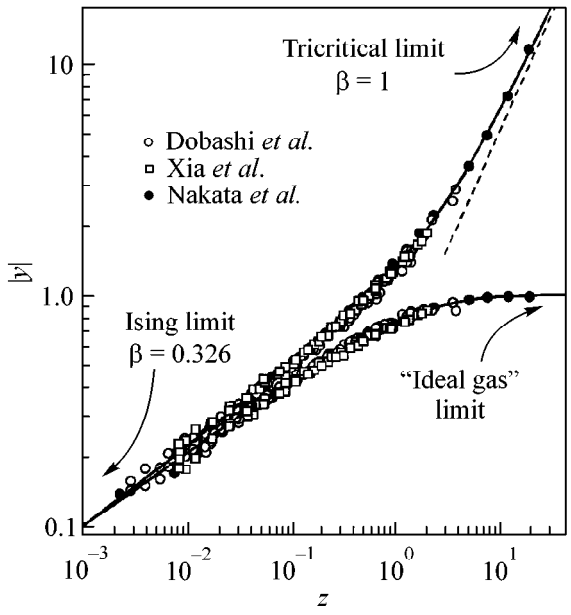

Fig. 3. Universal scaled coexistence curve of polymer solution in a log–log scale showing crossover from Ising behavior to "ideal gas" and tricritical (theta-point) behavior. Solid line is calculated from the crossover theory.

The universality demonstrated in Fig. 3 requires both τ and ϕ_c to be small. In first approximation, some nonasymptotic effects are incorporated into the universal scaling description. The slight dependence of A on ϕ_c for moderate molecular weights (at larger ϕ_c) shown in Fig. 1 absorbs nonasymptotic corrections to the critical limit. A nonasymptotic (at larger τ) nonlinearity of the phase separation boundary in the tricritical (zero-field) limit can be accounted for by a term quadratic in τ.

Renormalization group calculations [13] have shown the existence of logarithmic corrections to mean-field tricriticality: the coefficients v and λ_0 in expansion (5) are renormalized, so that the critical line has zero slope at the theta point. The resolution of the existing experimental data is not sufficient to convincingly determine the logarithmic corrections: the description is equally good with or without the corrections.

We acknowledge valuable discussions with M.E. Fisher, S.C. Greer, A.Z. Panagiotopoulos, J.V. Sengers, and B. Widom. The research at the University of Maryland was supported by DOE Grant no. DE-FG02-95ER-14509.

REFERENCES

1. T. Dobashi, M. Nakata, and M. Kaneko, J. Chem. Phys. **72**, 6685 (1980); **72**, 6692 (1980).

2. J. C. Le Guillou and J. Zinn-Justin, J. Phys. (Paris) **48**, 19 (1987).
3. P. J. Flory, *Principles of Polymer Chemistry* (Cornell Univ. Press, Ithaca, 1953), Chap. XIII.
4. B. Widom, Physica A (Amsterdam) **194**, 532 (1993).
5. A. A. Povodyrev, M. A. Anisimov, and J. V. Sengers, Physica A (Amsterdam) **264**, 345 (1999).
6. Y. Izumi and Y. Miyake, J. Chem. Phys. **81**, 1501 (1984).
7. I. C. Sánchez, J. Phys. Chem. **93**, 6983 (1989).
8. Yu. B. Melnichenko and G. D. Wignall, Phys. Rev. Lett. **78**, 686 (1997); Y. B. Melnichenko, M. A. Anisimov, A. A. Povodyrev, *et al.*, Phys. Rev. Lett. **79**, 5266 (1997).
9. K. Q. Xia, X.-Q. An, and W. G. Shen, J. Chem. Phys. **105**, 6018 (1996); K. Q. Xia, C. Frank, and B. Widom, J. Chem. Phys. **97**, 1446 (1992).
10. M. Nakata, T. Dobashi, N. Kuwahara, *et al.*, Phys. Rev. A **18**, 2683 (1978); M. Nakata, N. Kuwahara, and M. Kaneko, J. Chem. Phys. **62**, 4278 (1975).
11. P. G. de Gennes, *Scaling Concepts in Polymer Physics* (Cornell Univ. Press, Ithaca, 1979; Mir, Moscow, 1982).
12. M. E. Fisher, J. Stat. Phys. **75**, 1 (1994).
13. B. Duplantier, J. Phys. (Paris) **43**, 991 (1982).
14. L. D. Landau and E. M. Lifshitz, *Statistical Physics* (Nauka, Moscow, 1976; Pergamon, Oxford, 1980).

JETP Letters, Vol. 72, No. 11, 2000, pp. 583–592. Translated from Pis'ma v Zhurnal Éksperimental'noĭ i Teoreticheskoĭ Fiziki, Vol. 72, No. 11, 2000, pp. 845–858.

Microwave Response of High-T_c Superconducting Crystals: Results, Problems, and Prospects

M. R. Trunin

Institute of Solid State Physics, Russian Academy of Sciences, Chernogolovka, Moscow region, 142432 Russia
e-mail: trunin@issp.ac.ru

Received October 30, 2000

The results of studying temperature behavior of the microwave surface impedance $Z_s(T)$ and conductivity tensor $\hat{\sigma}(T)$ of high-T_c superconducting (HTSC) single crystals are analyzed. The emphasis is on the experimental facts that are inconsistent with the known electrodynamic concepts of conductivity mechanisms in these materials. Possible reasons for the inconsistency are discussed in the context of structural features of the HTSC crystals, and the outlook for future investigations is outlined. © *2000 MAIK "Nauka/Interperiodica".*

PACS numbers: 74.25.Nf; 74.72.-h; 74.20.De

INTRODUCTION

Despite a certain progress in elucidating the physical properties of high-temperature superconductors (HTSC), no consistent microscopic theory has been developed to date that would be capable of explaining the totality of available and firmly established experimental data even for a relatively narrow region of the phase diagram corresponding to optimum-doped HTSC materials and maximum critical temperatures T_c. A fundamental problem of type of superconducting interaction in HTSC also remains to be solved. There is much controversy over the symmetry of the order parameter, the mechanisms of quasiparticle relaxation, and the role of impurities and anisotropy in HTSC materials. Among the experimental methods of studying these problems are measurements of the linear microwave response of HTSC single crystals, i.e., studies of the temperature dependences of the surface impedance $Z_s(T) = R_s(T) + iX_s(T)$ and complex conductivity $\sigma(T) = \sigma'(T) - i\sigma''(T)$ at microwave (MW) frequencies and low (<0.1 Oe) amplitudes of ac field. It is known that the precise measurements of $Z_s(T)$ in classical superconductors proved to be quite informative: the gap Δ was derived from the temperature dependence of surface resistance $R_s(T) \propto e^{-\Delta/k_BT}$ at $T < T_c/2$, the field penetration depth $\lambda(T)$ into a superconductor was derived from the reactance $X_s(T) = \omega\mu_0\lambda(T)$ at $T < T_c$, and the electron mean free path was determined by measuring $R_s(T)$ and $X_s(T)$ in the normal state ($T \geq T_c$). The applicability of the Bardeen–Cooper–Schrieffer (BCS) theory [1] to classical superconductors was clearly demonstrated by the nonmonotonic behavior (coherence peak) of the microwave conductivity $\sigma'(T)$ at $0.8 < T/T_c \leq 1$. However, even the early studies of the impedance and conductivity of HTSC materials did not fit into the BCS theory: there was no coherence peak in $\sigma'(T)$ and, instead of exponential behavior at low temperatures, $Z_s(T)$ exhibited power law temperature dependence. A linear dependence of the penetration depth $\Delta\lambda_{ab}(T) \propto T$ at $T < 25$ K, first observed in 1993 in [2] for the *ab* plane of $YBa_2Cu_3O_{6.95}$ single crystals, has initiated wide speculation on the symmetry of the order parameter in HTSC materials.

In this work, I will focus on the fundamentals of the method for measuring impedance and the general properties and features of the $Z_s(T)$ and $\hat{\sigma}(T)$ curves in the normal and superconducting states of different HTSC crystals and discuss the phenomenological model for the description of their microwave response. Emphasis will be on the problems of residual surface resistance, unusually large change $\Delta X_s(T) > \Delta R_s(T)$ in some HTSC crystals, and conductivity anisotropy.

MEASURED QUANTITIES AND SAMPLES

In the centimeter and millimeter wavelength ranges, the surface impedance of small-sized HTSC samples with a surface area of ~1 mm^2 is measured by the so-called hot-finger method. A sample mounted on a sapphire rod was placed in the center of a cylindrical cavity made from Nb and operating at frequency $f = 9.42$ GHz in the H_{011} mode; i.e., the sample was placed in the maximum of a uniform microwave magnetic field $\mathbf{H}_\omega$ [3]. The temperature of the rod and the sample was varied from helium to room temperature without heating of the cavity, which was washed from outside by liquid helium and was always in the superconducting state. At some steady-state temperature T, the microwave power passed through the cavity was recorded as a function of frequency (resonance curve), from which was derived, in the first run, the Q factor $Q_s(T)$ and the frequency

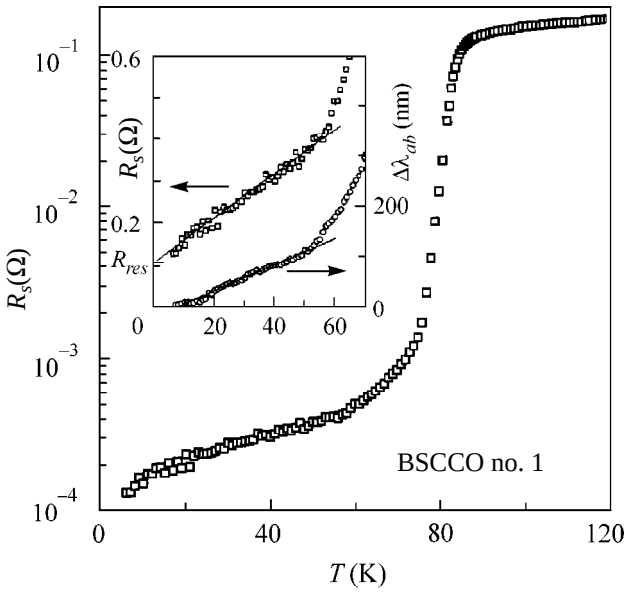

Fig. 1. Surface resistance $R_s(T)$ in the *ab* plane of BSCCO crystal no. 1 at a frequency of 9.4 GHz. Inset: $\Delta\lambda_{ab}(T)$ and $R_s(T)$ dependences at low *T*. The residual surface resistance $R_{res} \approx 120$ μΩ is indicated.

$f_s(T)$ of the cavity with the sample inside and, in the second run, $Q_e(T)$ and $f_e(T)$ of the cavity without the sample. The accuracy of measuring the Q factor ~10^7 was no worse than 1%, and the accuracy of determining the resonance frequency was ~10 Hz. The temperature dependences of the surface resistance R_s and reactance X_s of the sample are found from the relationships

$$R_s(T) = \Gamma_s\Delta(1/Q) = \Gamma_s[Q_s^{-1}(T) - Q_e^{-1}(T)], \quad (1)$$

$$X_s(T) = -2\Gamma_s\frac{\delta f}{f} = -\frac{2\Gamma_s}{f}[\Delta f_s(T) - \Delta f_e(T) - f_0], \quad (2)$$

where Γ_s is the geometric factor of the sample and δf is the frequency difference between the cavity with the sample and the cavity with an ideal conductor, identical in shape and size, into which the magnetic field does not penetrate. The δf value differs from the difference between the measured resonance frequency shifts $\Delta f_s - \Delta f_e = \Delta f$ by a constant f_0, which accounts both for frequency drift caused by the ideal conductor and for irreproducible changes in the cavity reference frequency upon putting in and taking out the sample. It follows from Eqs. (1) and (2) that, to determine the $R_s(T)$ and $X_s(T)$ values from the measured $Q(T)$ and $\Delta f(T)$ values, two quantities need to be known: Γ_s and f_0. The geometric factor Γ_s depends on the shape and size of the crystal and on its orientation about the field $\mathbf{H}_\omega$ in the cavity. The experimental and theoretical methods of determining Γ_s are known [3]; by order of magnitude, it is equal to tens of kiloohms at frequencies ~10 GHz. The f_0 constant can be determined from the measurements of the microwave response in the normal state (see below).

This work will consider the results of measuring the temperature-dependent impedance and conductivity of HTSC copper oxide crystals as platelets with transverse dimensions $a \sim b \sim 1$ mm and thickness $c \sim 0.1$ mm: $YBa_2Cu_3O_{6.95}$ (YBCO, $T_c \approx 93$ K), $Bi_2Sr_2CaCu_2O_{8+\delta}$ (BSCCO no. 1, $T_c \approx 83$ K and BSCCO no. 2, $T_c \approx 92$ K), $Tl_2Ba_2CaCu_2O_{8-\delta}$ (TBCCO, $T_c \approx 112$ K), and $Tl_2Ba_2CuO_{6+\delta}$ (TBCO, $T_c \approx 90$ K). Except for slightly overdoped BSCCO crystal no. 1, whose experimental dependences $R_s(T)$ and $\Delta\lambda_{ab}(T) = \Delta X_s(T)/\omega\mu_0$ in the *ab* plane are shown in Fig. 1, the compositions of all other crystals corresponded to the optimum doping.

Problem 1. The residual surface resistance $R_{res} = R_s(T \longrightarrow 0)$ deserves attention because it determines the quality of a crystal. Whereas the R_{res} value in classical superconductors is clearly defined as a level of the plateau in the $R_s(T)$ curve at $T < T_c/4$, no such plateau occurs in the HTSC crystals, so that by R_{res} is meant the $R_s(T = 0)$ value obtained by extrapolating the linear portion of the $R_s(T)$ curve at $T \ll T_c$ to zero temperature (inset in Fig. 1). It was experimentally established for classical superconductors that $R_{res} \propto \omega^2$ and is determined by various defects in the surface layer of the sample [4, 5]; based on this fact, it is usually agreed that the smaller R_{res} the higher the sample quality. In HTSC materials, the residual resistance also varies quadratically with frequency, but it exceeds the R_{res} value in usual superconductors by a factor of several tens even in the best crystals. When it is considered that the R_{res} value has failed to be noticeably reduced over the last 5–7 years of developing the methods of growing HTSC crystals and, in addition (see below), that the temperature behavior of conductivity $\sigma'(T)$ in the samples of identical chemical composition changes radically with changing R_{res}, then it becomes clear that elucidation of the nature of residual losses in HTSC materials is a highly topical problem.

At $T > 4$ K, the relation between the electric field and the current density in the normal and superconducting states of the HTSC materials has a local character: $j = \hat{\sigma}E$, where $\hat{\sigma}$ is the conductivity tensor which has only two components in a tetragonal crystal, i.e., the conductivity σ_{ab} in the CuO_2 *ab* plane and σ_c across the cuprate planes. In the hot-finger method, the components of the $\hat{\sigma}$ tensor can be found by measuring the microwave response for two crystal orientations about the direction of the $\mathbf{H}_\omega$ field: the transverse (T) $\mathbf{H}_\omega \| \mathbf{c}$ (Fig. 2a) and the longitudinal (L) $\mathbf{H}_\omega \perp \mathbf{c}$ (Fig. 2b) orientations.

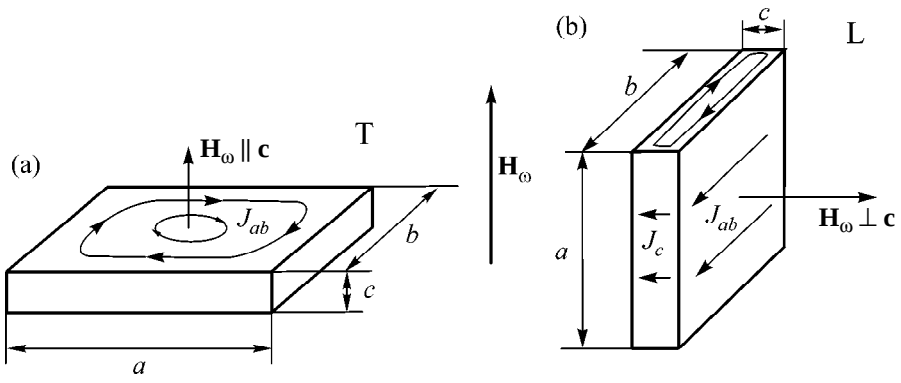

Fig. 2. (a) Transverse (T) crystal orientation, $\mathbf{H}_\omega \parallel \mathbf{c}$. Arrows indicate the direction of high-frequency currents. (b) Longitudinal (L) orientation, $\mathbf{H}_\omega \perp \mathbf{c}$.

ANALYSIS OF EXPERIMENTS WITH TRANSVERSE ORIENTATION

Surface impedance. Let us first consider the T orientation, for which the high-frequency currents circulate in the *ab* plane (Fig. 2a). At frequencies ~10 GHz, the field penetrates into the HTSC sample to a skin depth $\delta_{ab} \sim 5 \times 10^{-3}$ mm at $T \geq T_c$ and to a depth of $\lambda_{ab} \sim 10^{-4}$ mm at $T < T_c$. Since both values are much smaller than the crystal thickness *c*, one can consider the crystal impedance Z_s^{ab} in the T orientation as a coefficient in the Leontovich boundary condition [6] at any temperature and use the local relationship

$$Z_s^{ab} = R_s + iX_s = (i\omega\mu_0/\sigma_{ab})^{1/2} \qquad (3)$$

for the relation between the impedance and the conductivity σ_{ab}. If the microwave conductivity of HTSC is real at $T \geq T_c$, then the f_0 constant [see Eq. (2)] for the T orientation can be found, according to Eq. (3), from the condition that the imaginary and real parts of impedance are equal in the normal state, i.e., by fitting the temperature dependence $R_s(T)$ to $\Delta X_s(T)$ at $T \geq T_c$. This expedient was used to determine the $X_s(T)$ values for BSCCO crystal no. 2 over the entire temperature range (Fig. 3). It should be taken into account that the temperature behavior of the reactance in the T orientation may be noticeably affected by the thermal expansion of the crystal. Since the resonance frequency is determined by the volume occupied by the field, the crystal expansion is equivalent to a decrease in the penetration depth and, thus, leads to an additional frequency shift Δf_t in the square brackets in Eq. (2). It is shown in [3] that, although the contribution of Δf_t to the total frequency shift of the cavity is negligible at low temperatures, it becomes noticeable at $T > 0.9T_c$, especially for the strongly anisotropic HTSC crystals. The $X_s(T)$ dependence in Fig. 3 is constructed with allowance made for the thermal expansion of BSCCO crystal no. 2. Otherwise, i.e., without the Δf_t term in Eq. (2), the reactance curve coincides with the curve in Fig. 3 only up to $T \approx T_c$, while its slope at $T > T_c$ becomes smaller and at $T =$ 150 K the discrepancy is as large as 25 mΩ.

The condition $R_s(T) = X_s(T)$ for the normal skin effect was experimentally proved for the BSCCO [7–9], YBCO [7, 10–12], TBCCO [13], LaSrCuO [14], and BaKBiO [15] crystals at $T \geq T_c$ in the T orientation. All temperature dependences $R_s(T)$ of the HTSC crystals at $T \geq T_c$ fit the formula $2R_s^2(T)/\omega\mu_0 = \rho_{ab}(T) =$

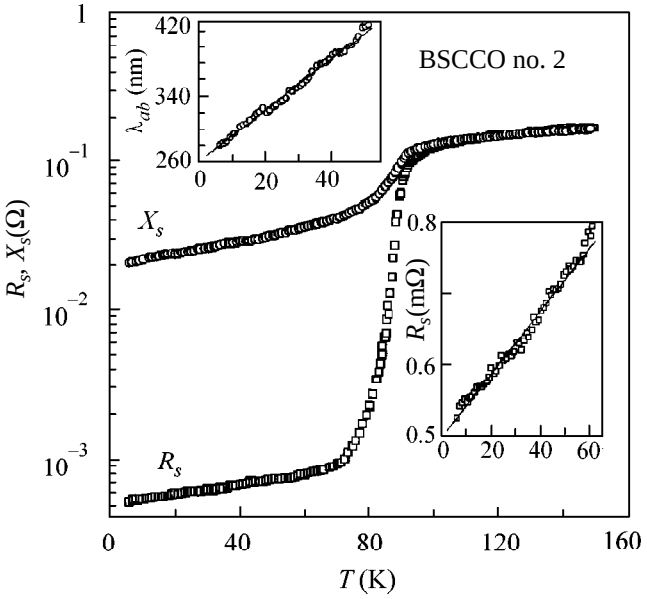

Fig. 3. $R_s(T)$ and $X_s(T)$ for T-oriented BSCCO crystal no. 2 at a frequency of 9.4 GHz. Inset: $\lambda_{ab}(T)$ and $R_s(T)$ dependences at low temperatures.

$\rho_{ab}(0) + bT$ well. For instance, $\rho_{ab}(0) \approx 13$ μΩ cm and $b \approx 0.3$ μΩ cm/K for BSCCO crystal no. 2.

Problem 2. The behavior of $Z_s(T)$ for the TBCO [16, 17] and HgBaCuO crystals is also under debate.[1] Even if one achieves coincidence between the $R_s(T)$ and $\Delta X_s(T)$ curves at $T \geq T_c$, i.e., $R_s(T) = X_s(T)$, the variation $\Delta X_s(T)$ of the reactance in the superconducting state $T < T_c$ proves to be so much larger than $\Delta R_s(T)$ that $X_s(0)$ becomes negative. In addition, the problem is complicated by the lack of literature data for the thermal expansion coefficients of the TBCO and HgBaCuO crystals. If one assumes that at $T > T_c$ the corresponding coefficient for the cuprate planes of TBCO is the same as in the BSCCO [18] or TBCCO [19] crystal and takes account of the $\Delta f_t(T)$ shift in Eq. (2), then the $R_s(T)$ and $X_s(T)$ curves in the normal state of TBCO become mutually parallel. However, an attempt at achieving coincidence through satisfying the condition for the normal skin effect leads to the $X_s(0) = \omega\mu_0\lambda_{ab}(0) < 0$ value. Therefore, the problem amounts to revealing either the cause for the appearance of a negative increment $dX_s < 0$ at $T < T_c$ that must be subtracted from the measured $\Delta X_s(T)$ curve in order to obtain the true value $X_s(T) > 0$ for the reactance coinciding with $R_s(T)$ at $T > T_c$ or the cause explaining the positive difference $X_s(T) - R_s(T)$ in the normal state of TBCO and providing a reasonable value $X_s(0) > 0$. In this respect, the following two growth and structural features of the TBCO crystals distinguish them from BSCCO. It is known that the so-called cleavage planes may crop out at the surface of the TBCO crystal, whereas the surface of the BSCCO crystal is smooth. If the traces of these planes form ridges (valleys) in the form of extended channels at the surface and if the sizes (height, width, spacing) of these roughnesses exceed the penetration depth for the field normal to the surface, then, as shown in [5], field screening by such roughnesses gives rise to a negative addition $dX_s < 0$ to the measured reactance $X_s(T)$. With a rise in temperature, the penetration depth increases and, at a certain $T^* < T_c$, reaches the roughness size. For this reason, the addition dX_s to the reactance can be ignored at $T > T^*$. Another possible reason why the measured $X_s(T)$ value is larger than $R_s(T)$ in the normal state of TBCO is the size effect in the T orientation. The unit cell of BSCCO contains two conducting CuO_2 planes, while the unit cell of TBCO, though being of approximately the same size, contains only one such plane. If the high-frequency currents mainly decay in these planes, then the screening thickness c^* of the TBCO crystal will be less than its actual thickness c and might be comparable with the skin depth. One can expect from the solution of the electrodynamic problem of field distribution in a T-oriented thin plate that, owing to the size effect, the measured effective $X_s^{\text{eff}}(T)$ value is greater than the effective $R_s^{\text{eff}}(T)$ at $T \geq T_c$.

[1] S. Sridhar, private communication.

The conductivity σ_{ab} in the superconducting state is a complex value, and, according to Eq. (3), the real R_s and imaginary X_s parts of the impedance are not equal to each other:

$$R_s(T) = \sqrt{\frac{\omega\mu_0(\varphi^{1/2} - 1)}{2\sigma''\varphi}},$$
$$X_s(T) = \sqrt{\frac{\omega\mu_0(\varphi^{1/2} + 1)}{2\sigma''\varphi}}, \quad (4)$$

where $\varphi = 1 + (\sigma'/\sigma'')^2$. Evidently, $R_s(T) < X_s(T)$ at $T < T_c$. For $\sigma' \ll \sigma''$, which is the case in the temperature range not too close to T_c, one has from Eq. (4)

$$R_s \simeq \frac{(\omega\mu_0)^{1/2}\sigma'}{2(\sigma'')^{3/2}} = \frac{1}{2}\omega^2\mu_0^2\sigma'\lambda^3,$$
$$X_s \simeq \left(\frac{\omega\mu_0}{\sigma''}\right)^{1/2} = \omega\mu_0\lambda. \quad (5)$$

The linear dependence of the reactance $\Delta X_s(T) \propto \Delta\lambda_{ab}(T) \propto T$ and the linear dependence of the surface resistance $\Delta R_s(T) \propto T$ at frequencies ~10 GHz and below are the regularities common to all HTSC crystals at $T \ll T_c$ (see Figs. 1, 3 and reviews [3, 20–22] and references therein). The slopes of the $\Delta\lambda_{ab}(T)$ straight lines at $T \ll T_c$ are different. For example, in the YBCO crystals prepared by different methods, the slopes for $\Delta\lambda_{ab}(T)$ may diverge by approximately an order of magnitude [12, 23, 24]. The $Z_s(T)$ curves for the BSCCO, TBCCO, and TBCO crystals with tetragonal lattice also differ from those for the orthorhombic YBCO crystals. Whereas the linear dependence $\Delta R_s(T) \propto T$ at frequencies ~10 GHz for the first of them may extend up to $T_c/2$ (Figs. 1, 3), in YBCO it terminates at $T < T_c/3$ and gives way to a broad peak in $R_s(T)$ (Fig. 4). With an increase in frequency, the peak shifts to higher temperatures and its amplitude decreases. It is also known that the higher the quality of the YBCO crystal the larger the peak amplitude and the lower the temperature of its occurrence [25]. Finally, the $\lambda_{ab}(T)$ [12, 23] and $R_s(T)$ [23] curves for single crystal YBCO show some features in the intermediate temperature range $T \sim T_c/2$.

Complex conductivity. The $\sigma'(T)$ and $\sigma''(T)$ components are not determined directly from the experiment but can be found from Eq. (4) after measuring, according to Eqs. (1) and (2), the $R_s(T)$ and $X_s(T)$ values:

$$\sigma' = \frac{2\omega\mu_0 R_s X_s}{(R_s^2 + X_s^2)^2}, \quad \sigma'' = \frac{\omega\mu_0(X_s^2 - R_s^2)}{(R_s^2 + X_s^2)^2}. \quad (6)$$

It should be emphasized that, to determine the conductivity components, it is necessary to know the $R_s(T)$ and $X_s(T)$ values in absolute units. At temperatures not too close to T_c, $R_s(T) \ll X_s(T)$ for the HTSC crystals. Consequently, the $\sigma''(T)$ curves are determined solely by the $X_s(T) = \omega\mu_0\lambda(T)$ function and reflect the main features of the temperature behavior of the penetration depth, namely, its linear temperature dependence at low temperatures for all high-quality HTSC crystals and the features observed for YBCO in the intermediate temperature range. The shape of the $\sigma'_{ab}(T)$ curve depends on the residual surface resistance R_{res}. It follows from Eq. (6) that $\sigma'_{ab}(T)$ has a maximum at $T < T_c$ if [22]

$$R_{res} < \frac{X_s(0)}{3}\frac{dR_s(T)}{dX_s(T)}\bigg|_{T\to 0}. \qquad (7)$$

As R_{res} increases, the peak in the $\sigma'_{ab}(T)$ curve shifts to lower temperatures and disappears when R_{res} reaches the value equal to the right-hand side of Eq. (7). If the R_{res} value for the crystal is such that inequality (7) breaks, the conductivity $\sigma'_{ab}(T)$ becomes a monotonically decreasing function of temperature at $T < T_c$. Figure 5 demonstrates both possible shapes of the $\sigma'_{ab}(T)$ curves at a frequency of 9.4 GHz, namely, the peak for BSCCO crystal no. 1 (Fig. 5a, $R_{res} \approx 120$ μΩ) and its absence for BSCCO crystal no. 2 (Fig. 5b, $R_{res} \approx$ 500 μΩ). The higher the crystal quality, the more pronounced the conductivity peak at $T < T_c$. The $\sigma'_{ab}(T)$ curve in Fig. 6 corresponds to the $R_s(T)$ dependence obtained for the YBCO crystal at a frequency of 1.14 GHz (Fig. 4, $R_{res} \sim 1$ μΩ). Beginning with a steep linear portion, the $\sigma'_{ab}(T)$ curve rapidly reaches its maximum value, which always markedly exceeds the conductivity $\sigma'(T_c)$ in the normal state. As the frequency increases, the peak in $\sigma'_{ab}(T)$ shifts to higher temperatures and its amplitude decreases. At temperatures close to T_c, the $\sigma'(T)$ curve for the HTSC materials is shaped like a narrow peak with width virtually coinciding with the width of the superconducting transition in the $R_s(T)$ curve.

Modified two-fluid model (MTM). A simple way of describing all the observed $Z_s^{ab}(T)$ and $\sigma_{ab}(T)$ dependences was suggested in [15, 26] and further developed in [3, 21, 22, 27, 28]. The idea consists in the extension of a Gorter–Casimir (GC) two-fluid model [29] to the HTSC materials, which are characterized by high T_c values. In metals, the quasiparticle inelastic scattering at such temperatures becomes essential and, hence, the GC model should be naturally modified by incorporating the temperature-dependent relaxation time τ for the quasiparticles of a "normal fluid." Assuming that the scattering processes in this fluid are

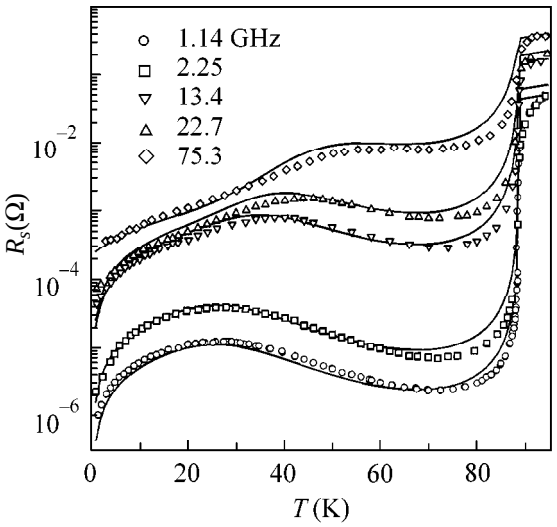

Fig. 4. Symbols correspond to the $R_s(T)$ values measured in the *ab* plane of YBCO crystal at different frequencies [25]. Solid lines correspond to the calculations by Eqs. (4), (8), and (9) with $\kappa = 9$ and experimentally determined $\tau(T_c) = 10^{-13}$ s, $\beta = 0.005$, and $n_s(T)/n = \sigma''(T)/\sigma''(0)$. To the $R_s(T)$ value calculated for the upper curve (75.3 GHz) $R_{res} = 0.3$ mΩ was added.

similar to those occurring in normal metals, we used the Bloch–Grüneisen formula (electron–phonon scattering) for the function $\tau(T)$ in the normal and superconducting states of HTSC and retained the temperature-independent impurity relaxation time $\tau(0)$, which is present in the standard GC model:

$$\frac{1}{\tau} = \frac{1}{\tau(0)}\left[1 + \frac{t^5 \mathcal{J}_5(\kappa/t)/\mathcal{J}_5(\kappa)}{\beta}\right],$$
$$\mathcal{J}_5(\kappa/t) = \int_0^{\kappa/t} \frac{z^5 e^z dz}{(e^z - 1)^2}, \qquad (8)$$

where $t \equiv T/T_c$; $\kappa = \Theta/T_c$ (Θ is the Debye temperature); and β is a numerical parameter equal, according to Eq. (8), to $\tau(T_c)/[\tau(0) - \tau(T_c)]$. Following the formal analogy to metals, one can state that β characterizes the "degree of purity" of HTSC material: $\beta \approx \tau(T_c)/\tau(0) \ll 1$ if $\tau(0) \gg \tau(T_c)$. It is shown in [22] that the parameter β can be derived from the measured $R_s(T)$ and $X_s(0)$ values and the dR_s/dT and dX_s/dT slopes at $T \ll T_c$. The Θ temperature for HTSC is estimated at several hundred degrees. At $T < \Theta/10$ ($\kappa > 10t$), the second term in the square brackets in Eq. (8) is proportional to T^5 and at $T > \Theta/5$ ($\kappa < 5t$), it is proportional to T. Therefore, at $\beta < 1$, the inverse relaxation time (coefficient of quasiparticle decay) equals $1/\tau(0)$ in the range $T \ll T_c$ and monotonically increases with temperature following a power law from $\propto T^5$ to $\propto T$ near T_c, thereby providing the linear temperature dependence $\Delta\rho_{ab}(T) \propto 1/\tau(T) \propto T$ at $T > T_c$.

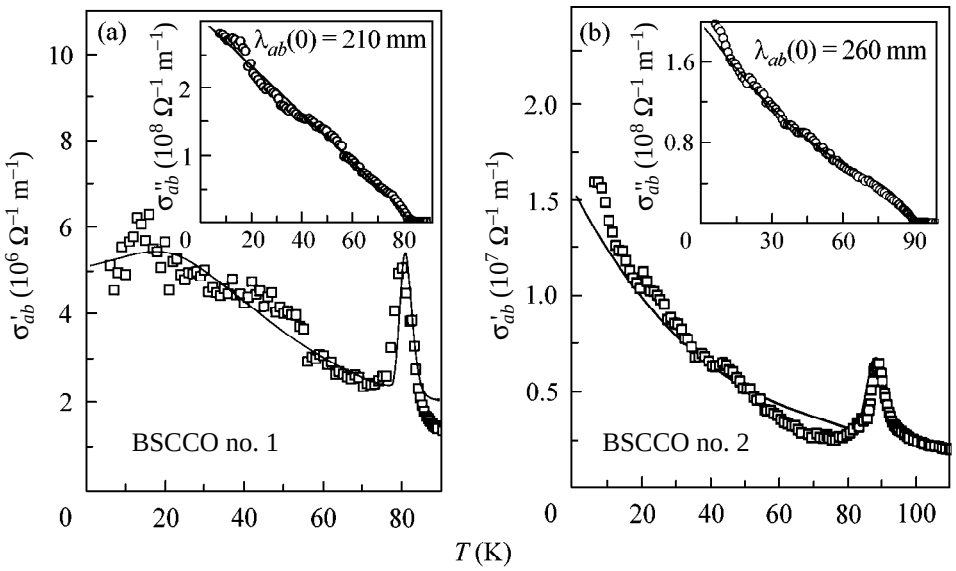

Fig. 5. Symbols correspond to $\sigma'_{ab}(T)$ and (inset) $\sigma''_{ab}(T)$ determined for BSCCO crystal nos. 1 and 2 by Eq. (6) using the measured $R_s(T)$ and $X_s(T)$ values. Solid lines correspond to the calculations by Eqs. (8) and (9) with $\kappa = 2$ for BSCCO crystal no. 1 and $\kappa = 3$ for no. 2 and experimental values $T_c = 83$ K, $\delta T_c = 2.5$ K, $\omega\tau(T_c) = 7 \times 10^{-3}$, $\beta = 0.3$, $\alpha = 1$, and $R_{res} = 120$ μΩ for BSCCO no. 1 and $T_c = 92$ K, $\delta T_c = 4.5$ K, $\omega\tau(T_c) = 9 \times 10^{-3}$, $\beta = 2$, $\alpha = 2$, and $R_{res} = 500$ μΩ for BSCCO no. 2.

Despite the fairly simplified form of $\tau(T)$ chosen for HTSC materials with a complex band structure, it turns out that all common and specific features of the $R_s(T)$ and $\sigma'_{ab}(T)$ curves are adequately described by the MTM with only one fitting parameter κ in Eq. (8). Indeed, the conductivity components are

$$\sigma' = \frac{n_n e^2 \tau}{m} \frac{1}{1 + (\omega\tau)^2},$$
$$\sigma'' = \frac{n_s e^2}{m\omega}\left[1 + \frac{n_n}{n_s}\frac{(\omega\tau)^2}{1 + (\omega\tau)^2}\right], \quad (9)$$

where $n_n(T)$ and $n_s(T)$ are the densities of the normal and superconducting carriers, respectively (both have the same charge e and mass m); the total concentration $n = n_n + n_s$ is equal to the concentration of charge carriers in the normal state and is independent of T. Making use of the measured dependence $n_s(T)/n = \sigma''(T)/\sigma''(0) = \lambda^2(0)/\lambda^2(T)$ and, hence, determining the function $n_n(T)/n = 1 - n_s(T)/n$, one can chose the κ parameter for the sample of interest using Eqs. (8) and (9) to describe, first by Eq. (4), all the above-mentioned experimental $R_s(T)$ curves and, next by Eq. (6), the real part $\sigma'_{ab}(T)$ of the conductivity for the T-oriented HTSC crystal. The solid lines in Figs. 4–6 are examples of a comparison between the experimental and MTM curves.

Here, I should enlarge upon two important points that have not yet been discussed but were implicitly used in the calculations. First, account was taken of the inhomogeneous broadening δT_c of superconducting transition near T_c. This was done using the approach that was suggested in [21, 22] and gave rise to a maximum of the effective conductivity $\sigma'(T)$ at temperature $T_m = T_c - \delta T_c$ close to the critical temperature. The relative amplitude of this peak $[\sigma'(T_m) - \sigma(T_c)]/\sigma(T_c)$ is inversely proportional to the frequency and decreases with decreasing width (δT_c) of the superconducting transition [22].

Second, when comparing with the experimentally measured surface resistance, the temperature-independent R_{res} value was taken from the same experiment and added to the $R_s(T)$ value calculated using general Eq. (4). That is why the $\sigma'_{ab}(T)$ curves calculated by Eq. (6) do not turn to zero at $T \longrightarrow 0$ in Fig. 5, although the two-fluid model assumes that the density $n_n = 0$ at $T = 0$ and, according to Eq. (9), the conductivity $\sigma'(0) = 0$. The R_{res} value was not taken into account when comparing with the data in Figs. 4 (except for the upper curve) and 6 because the corresponding $R_{res}/R_s(T)$ ratios are very small (less than 10^{-3}). In most HTSC crystals, $R_{res}/R_s(T_c) > 10^{-3}$, so that the effect of the residual surface resistance becomes noticeable at $T \ll T_c$. One more reason for the inclusion of R_{res} is that the ratio $R_{res}/R_s(T_c) \propto \omega^{3/2}$ increases with frequency and becomes appreciable for the upper curve in Fig. 4.

Problem 1 (continued). The question of the nature of the residual losses remains open for HTSC materials. In some works (see, e.g., [30]), the origin of these losses was explained by the presence of a certain

amount n_0 of unpaired carriers in the sample at $T = 0$. The R_{res} value was estimated by using Eq. (5) with nonzero conductivity $\sigma'(0) = n_0 e^2 \tau(0)/m$ [Eq. (9) at $(\omega\tau)^2 \ll 1$]. However, it can easily be shown that the R_{res} values thus determined must satisfy inequality (7); otherwise, as it may occur for the HTSC crystals (see Fig. 5b), the n_0 value would exceed the total carrier concentration n. In many works developing the traditional approach assigning the residual resistance to various surface imperfections, the losses were explained by the presence of weak links [31–33], twin boundaries [33, 34], normally conducting clusters [35], etc. However, estimates show that the contribution from such losses is small compared to the R_{res} values measured in the HTSC materials. In addition, the residual surface resistance is approximately the same in perfect HTSC copper oxide crystals prepared by different methods or having different chemical compositions, containing twins or not, and with a freshly cleaved surface or as-grown surface: $R_{res} \sim 100$ μΩ at a frequency of 10 GHz. This fact indicates that the origin of residual losses has an "intrinsic" character and is inherent in all high-quality HTSC crystals. It is most likely associated with the structural features of these materials, namely, with the pronounced layered structure of these compounds. In other words, the current in the surface layer of HTSC crystals may flow in a nonsuperconducting part of the layer possessing a finite resistivity ρ_n. In the model under discussion, this additional contribution can be taken into account as a circuit element ρ connected in parallel to the two-fluid circuit characterized by Eq. (9), i.e., as a resistance $\rho = 1/\sigma'$ shunted by a kinetic inductance $l = 1/\omega\sigma''$ (parallel connection of ρ and l corresponds to the coupling adopted between current and field in the two-fluid model). Evidently, the complex circuit impedance consists of the imaginary part $iX_s = i\omega\mu_0\lambda$ at $T < T_c$ and the sum of two real terms: R_s from Eq. (5) and $R_0 = \omega^2\mu_0^2\lambda^3/2\rho_n$. At $T = 0$, when $R_s(0) = 0$, the latter can play the role of a residual surface resistance R_{res} proportional to ω^2, as it follows from the experiments. At a frequency of 10 GHz and for the $R_{res} \approx 100$ μΩ and $\lambda(0) \approx 0.2$ μm values typical of HTSC crystals, one obtains a typical metallic value $\rho_n(0) \approx 25$ μΩ cm. According to the above-mentioned procedure of comparison with the experimental $R_s(T)$ curves, one must also require that R_0 be independent of temperature at $T \ll T_c$. This is possible if $\rho_n(T) \propto \lambda^3(T)$; i.e., $\rho_n(T)$ should vary linearly with temperature at $T \ll T_c$: $\rho_n(t) = \rho_n(0)(1 + 1.5\alpha t)$, where α is the slope of the $\sigma''(t)$ curve at $t \ll 1$ in this sample:

$$\sigma''(t)/\sigma''(0) = \lambda^2(0)/\lambda^2(t) \simeq (1 - \alpha t). \qquad (10)$$

The coefficients $\rho_n(0)$ and $1.5\alpha\rho_n(0)/T_c$ in BSCCO crystal no. 2 are approximately equal to the coefficients $\rho_{ab}(0)$ and b in the expression $\rho_{ab}(T) = \rho_{ab}(0) + bT$ for the resistivity of this sample in the normal state; i.e., $\rho_n(T) \approx 2R^2(T)/\omega\mu_0$, where $R(T)$ is the continuation of the $R_s(T)$ line at $T > T_c$ (Fig. 3) to the superconducting region $T < T_c$ (down to $T = 0$).

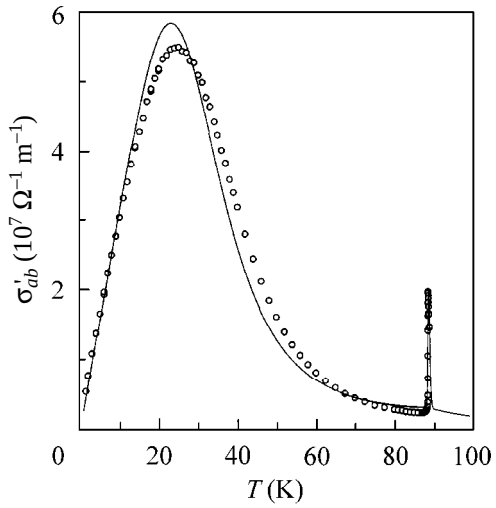

Fig. 6. (Circles) $\sigma'_{ab}(T)$ for YBCO crystal at a frequency of 1.14 GHz [25] and (solid line) the calculation by Eqs. (8) and (9) with $\kappa = 9$, $\tau(T_c) = 10^{-13}$ s, $\beta = 0.005$, and $\delta T_c = 0.4$ K.

It would be appropriate to close the discussion of the MTM by writing formulas describing the experimental data $n_s(T)/n = \sigma''(T)/\sigma''(0)$, which were used for calculating $R_s(T)$ and $\sigma'_{ab}(T)$ in the T orientation. There are several variants of such empirical formulas [3, 21, 22, 26, 27]. All of them have the form of Eq. (10) at $T \ll T_c$, because all $\sigma''_{ab}(T)$ curves for HTSC single crystals are characterized by the linear dependence at low temperatures.

Thus, the model based on Eqs. (8)–(10) adequately describes the general properties of the $Z_s(T)$ and $\sigma_{ab}(T)$ curves for high-quality HTSC crystals. It follows from these formulas that all curves have a linear portion at $t \ll 1$: $\sigma' \propto \alpha t/\beta$, because $n_n/n \approx \alpha t$ and $\tau \approx \tau(0) \approx \tau(T_c)/\beta$; $\Delta\sigma'' \propto -\alpha t$; $R_s \propto \alpha t/\beta$ according to Eq. (5); and $\Delta X_s \propto \Delta\lambda \propto \alpha t/2$. As the temperature increases, the $\sigma'(t)$ function passes through a maximum at $t < 0.5$ if the residual surface resistance R_{res} is so small that inequality (7) is fulfilled. This peak arises from the superposition of two opposite effects: a decrease in the number of normal carriers with decreasing temperature at $t < 1$ and an increase (terminating at $t \sim \beta^{1/5}$) in the relaxation time. If Eq. (7) is not fulfilled, $\sigma'(t)$ monotonically decreases with temperature elevation. This model also describes the temperature dependences of the surface impedance and the complex conductivity of YBCO single crystals grown by different methods. The postulates and consequences of the MTM are analyzed in recent works [21, 22] from the viewpoint of modern microscopic theories of the microwave response of HTSC materials.

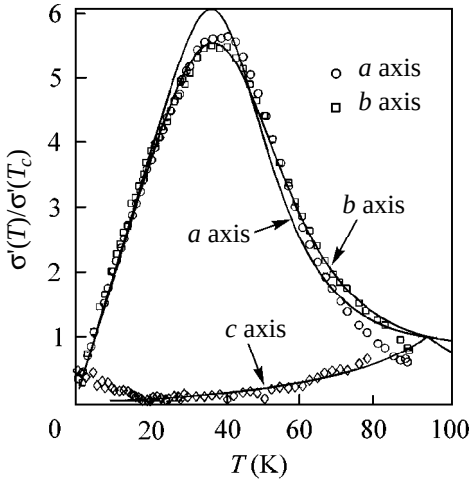

Fig. 7. (Symbols) components of the conductivity tensor $\hat{\sigma}'(T)/\hat{\sigma}(T_c)$ for YBCO at a frequency of 22 GHz [40] at $T < T_c$. (Solid lines) calculations [28] by Eqs. (8) and (9).

CONDUCTIVITY OF HTSC CRYSTALS ALONG THE *c* AXIS

Problem 3. Let us now consider the L orientation of a crystal with respect to the $\mathbf{H}_\omega$ field in the cavity, $\mathbf{H}_\omega \perp \mathbf{c}$ (Fig. 2b). In the superconducting state, the high-frequency currents flowing in the *ab* planes decay at a depth of λ_{ab}, while the *c*-directed currents decay at a depth of λ_c. At $T < 0.9T_c$, these values are small compared to the characteristic sizes of the crystal, allowing one to introduce the effective impedance Z_s^{ab+c} for the L orientation, defined as a surface-averaged value $Z_s^{ab+c} \simeq (bZ_s^{ab} + cZ_s^c)/(b + c)$, where the superscripts on Z_s indicate the directions of screening currents. By measuring $Z_s^{ab}(T)$ in the T orientation and Z_s^{ab+c} in the L orientation, one can determine the losses $R_s^c(T)$ and a change $\Delta\lambda_c(T) = \Delta X_s^c(T)/\omega\mu_0$ [8, 10, 14, 36–39]. To determine $\lambda_c(T)$, one is forced to invoke the results of independent measurements of $\lambda_c(0)$. The literature data on the low-temperature behavior of $\Delta\lambda_c(T)$ are controversial. Both linear dependence $\Delta\lambda_c(T) \propto T$ at $T < T_c/3$ [36, 39] and quadratic dependence [40] were observed even for the most extensively studied YBCO single crystals. In BSCCO crystals, the behavior of $\Delta\lambda_c(T)$ depends on the level of doping with oxygen: in the crystals with maximal $T_c \simeq 90$ K the linear dependence $\Delta\lambda_c(T)$ [8, 9, 38] converts into quadratic [38] as the oxygen content increases.

In recent work [40], detailed measurements of the impedance anisotropy were carried out and the conductivity components along the crystallographic axes were found for the optimum-doped untwinned YBCO crystals. In [28], we undertook an attempt at applying the MTM to the totality of experimental data obtained in [40]. For the real parts of the conductivity tensor, the comparison is shown in Fig. 7 [28]. The peak in $\sigma_c'(T)$ is absent because the temperature dependence of the relaxation time of normal quasiparticles along the *c* axis is very weak at $T < T_c$; i.e., $\tau_c(T) \approx$ const and $\beta_c \gg 1$ in Eq. (8). Moreover, since the inductive losses due to the large λ_c value markedly exceed the active losses (small R_s^c and σ_c' values), it is likely that the microwave *c*-response is mainly caused by the tunneling of Cooper pairs between the CuO_2 planes. Note that, according to the measurements in [40], the surface resistance $R_s^c(T) < R_s^{ab}(T)$ in the range $10 < T < 65$ K. However, in all previous works, the loss measurements

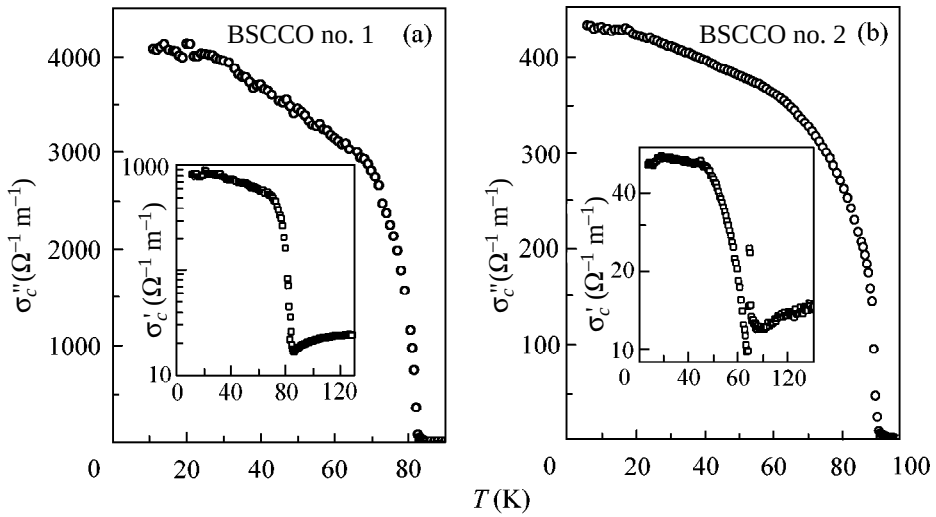

Fig. 8. Conductivity components $\sigma_c''(T)$ and $\sigma_c'(T)$ for BSCCO crystal nos. 1 and 2.

for the optimum-doped HTSC crystals gave the reverse relation $R_s^c(T) \gg R_s^{ab}(T)$ at $T < T_c$.

The aforementioned approach to studying the impedance anisotropy for HTSC crystals at $T < T_c$ gives no way of determining the $\lambda_c(T)$ value from the measurements of the Q factor and the resonance frequency shift in the L orientation and, in addition, cannot be extended to higher temperatures. The point is that the size effect becomes significant at $T > 0.9T_c$ in the L orientation and is the cause of the divergence between the temperature behavior of the effective $R_{s,\,\mathrm{eff}}^{ab+c}(T)$ value measured in the normal state and the $\Delta X_{s,\,\mathrm{eff}}^{ab+c}(T)$ value; as a result, the f_0 constant in Eq. (2) cannot be determined, as it was done previously. Recently [9], we suggested a new procedure for the determination of the f_0 value in the L orientation and, hence, the conductivity components $\sigma_c'(T)$ and $\sigma_c''(T)$ along the c axis. The procedure is based on the known formulas [41] allowing for the size effect in the field distribution in a long anisotropic strip with size $a \gg b, c$ (Fig. 2b). The $\sigma_c'(T)$ and $\sigma_c''(T)$ dependences obtained for BSCCO crystal nos. 1 and 2 using this procedure are shown in Fig. 8 [42]. The $\lambda_c(0)$ value proved to be equal to approximately 50 μm for sample no. 1 and 150 μm for sample no. 2, in agreement with the results of our measurements of $\lambda_c(0)$ in these crystals by other methods [43, 44]. One can see from Fig. 8 that the conductivity $\sigma_c'(T)$ in both samples grows with decreasing temperature at $T < T_c$, despite the fact that the $\sigma_{ab}'(T)$ dependences in these crystals are different (Fig. 5). The formal reason for this growth is clear: the residual losses R_{res}^c along the c axis of BSCCO crystal nos. 1 and 2 are large enough so that inequality (7) breaks. At the same time, the $\sigma_c'(T)$ dependences measured for BSCCO crystals by other techniques [45, 46] showed semiconductor behavior at $T < T_c$.

CONCLUSION

The results of measuring the surface impedance and the complex conductivity of the T-oriented ($\mathbf{H}_\omega \parallel \mathbf{c}$) optimum-doped samples of different chemical composition are systematized and described within the framework of the MTM. The common feature of the experimental $Z_s^{ab}(T)$ and $\sigma_{ab}(T)$ curves obtained for HTSC single crystals is that the conductivity components $\sigma_{ab}'(T)$ and $\sigma_{ab}''(T)$, the reactance $\Delta X_s(T) \propto \Delta\lambda_{ab}(T) \propto T$, and the surface resistance $\Delta R_s(T) \propto T$ linearly depend on temperature at $T \ll T_c$. In terms of the MTM, such behavior of the microwave response of HTSC materials is caused by the linear decrease in the density $n_s(T)$ of superconducting carriers with a rise in temperature at $T \ll T_c$. A broad peak at $T < T_c$ in the $R_s^{ab}(T)$ curve is the distinctive feature of the YBCO crystals. In the MTM, the presence or absence of this peak is governed by a change in $\tau(T)$ in the temperature range $0 < T < T_c$: whereas the $\tau(T_c) \approx 10^{-13}$ s value is approximately the same for all high-quality HTSC crystals at $T = T_c$, the $\tau(0)$ value in YBCO is greater than $\tau(0)$ in other compounds by a factor of ten and more at $T \ll T_c$. The reason why the change in the reactance $\Delta X_s(T)$ exceeds the change in the surface resistance $\Delta R_s(T)$ of TBCO crystals remains to be clarified. The origin of residual losses in HTSC is among the hottest problems because the behavior of real components $\hat{\sigma}'(T)$ of the conductivity tensor is governed at $T < T_c$ by this quantity. The anisotropy of high-frequency conductivity of HTSC materials also calls for detailed study.

I am grateful to all participants (I.E. Batov, A.A. Zhukov, G.V. Merzlyakov, Yu.A. Nefedov, A.T. Sokolov, G.É. Tsydynzhapov, A.F. Shevchun, and D.V. Shovkun) of project nos. 97-02-16836 and 00-02-17053 of the Russian Foundation for Basic Research for collaboration and activity. Discussions with V.F. Gantmakher, A.A. Golubov, and E.G. Maksimov were very useful. I appreciate fruitful collaboration with foreign colleagues A. Agliolo-Gallitto, N. Bontemps, A. Buzdin, I. Ciccarello, H. Fink, J. Halbritter, M. Li Vigni, S. Sridhar, and T. Tamegai and the support of the CNRS-RAS (grant no. 4985), CLG NATO, Coll. Int. Li Vigni, and RFFI-NNIO (project no. 00-02-04021).

REFERENCES

1. J. Bardeen, L. N. Cooper, and J. R. Schrieffer, Phys. Rev. **108**, 1175 (1957).
2. W. N. Hardy, D. A. Bonn, D. C. Morgan, *et al.*, Phys. Rev. Lett. **70**, 3999 (1993).
3. M. R. Trunin, Usp. Fiz. Nauk **168**, 931 (1998) [Phys. Usp. **41**, 843 (1998)]; J. Supercond. **11**, 381 (1998).
4. J. P. Turneaure, J. Halbritter, and H. A. Schwettman, J. Supercond. **4**, 341 (1991).
5. F. F. Mende and A. A. Spitsyn, *Surface Impedance of Superconductors* (Naukova Dumka, Kiev, 1985).
6. L. D. Landau and E. M. Lifshitz, *Course of Theoretical Physics*, Vol. 8: *Electrodynamics of Continuous Media* (Fizmatlit, Moscow, 1982; Pergamon, New York, 1984).
7. T. Shibauchi, A. Maeda, H. Kitano, *et al.*, Physica C (Amsterdam) **203**, 315 (1992).
8. T. Jacobs, S. Sridhar, Q. Li, *et al.*, Phys. Rev. Lett. **75**, 4516 (1995).
9. D. V. Shovkun, M. R. Trunin, A. A. Zhukov, *et al.*, Pis'ma Zh. Éksp. Teor. Fiz. **71**, 132 (2000) [JETP Lett. **71**, 92 (2000)].
10. H. Kitano, T. Shibauchi, K. Uchinokura, *et al.*, Phys. Rev. B **51**, 1401 (1995).
11. D. Achir, M. Poirier, D. A. Bonn, *et al.*, Phys. Rev. B **48**, 13184 (1993).

12. M. R. Trunin, A. A. Zhukov, G. A. Emel'chenko, *et al.*, Pis'ma Zh. Éksp. Teor. Fiz. **65**, 893 (1997) [JETP Lett. **65**, 938 (1997)].
13. A. A. Zhukov, M. R. Trunin, A. T. Sokolov, *et al.*, Zh. Éksp. Teor. Fiz. **112**, 2210 (1997) [JETP **85**, 1211 (1997)].
14. T. Shibauchi, H. Kitano, K. Uchinokura, *et al.*, Phys. Rev. Lett. **72**, 2263 (1994).
15. M. R. Trunin, A. A. Zhukov, G. É. Tsydynzhapov, *et al.*, Pis'ma Zh. Éksp. Teor. Fiz. **64**, 783 (1996) [JETP Lett. **64**, 832 (1996)].
16. J. R. Waldram, D. M. Broun, D. C. Morgan, *et al.*, Phys. Rev. B **59**, 1528 (1999).
17. N. Hakim, Yu. A. Nefyodov, S. Sridhar, *et al.*, unpublished.
18. C. Meingast, A. Junod, and E. Walker, Physica C (Amsterdam) **272**, 106 (1996).
19. M. Hasegawa, Y. Matsushita, and H. Takei, Physica C (Amsterdam) **267**, 31 (1996).
20. D. A. Bonn and W. N. Hardy, in *Physical Properties of High Temperature Superconductors V*, Ed. by D. M. Ginsberg (World Scientific, Singapore, 1995), p. 7.
21. M. R. Trunin and A. A. Golubov, in *HTSC Spectroscopy*, Ed. by N. M. Plakida (Gordon and Breach, London, 2001) (in press).
22. M. R. Trunin, Yu. A. Nefyodov, and H. J. Fink, Zh. Éksp. Teor. Fiz. **118**, 923 (2000) [JETP **91**, 801 (2000)].
23. H. Srikanth, B. A. Willemsen, T. Jacobs, *et al.*, Phys. Rev. B **55**, R14733 (1997).
24. S. Kamal, R. Liang, A. Hosseini, *et al.*, Phys. Rev. B **58**, R8933 (1998).
25. A. Hosseini, R. Harris, S. Kamal, *et al.*, Phys. Rev. B **60**, 1349 (1999).
26. H. J. Fink, Phys. Rev. B **58**, 9415 (1998).
27. H. J. Fink and M. R. Trunin, Physica B (Amsterdam) **284**, 923 (2000); H. J. Fink, Phys. Rev. B **61**, 6346 (2000).
28. H. J. Fink and M. R. Trunin, Phys. Rev. B **62**, 3046 (2000).
29. C. S. Gorter and H. Casimir, Phys. Z. **35**, 963 (1934).
30. M. Hein, T. Kaiser, and G. Müller, Phys. Rev. B **61**, 640 (2000).
31. T. L. Hylton and M. R. Beasly, Phys. Rev. B **39**, 9042 (1989).
32. A. M. Portis and D. W. Cooke, Supercond. Sci. Technol. **5**, S395 (1992).
33. J. Halbritter, J. Appl. Phys. **68**, 6315 (1990); **71**, 339 (1992).
34. O. G. Vendik, A. B. Kozyrev, and A. Yu. Popov, Rev. Phys. Appl. **25**, 255 (1990).
35. O. G. Vendik, L. Kovalevich, A. P. Mitrofanov, *et al.*, Sverkhprovodimost: Fiz., Khim., Tekh. **3**, 1573 (1990).
36. J. Mao, D. H. Wu, J. L. Peng, *et al.*, Phys. Rev. B **51**, 3316 (1995).
37. D. A. Bonn, S. Kamal, K. Zhang, *et al.*, J. Phys. Chem. Solids **56**, 1941 (1995).
38. T. Shibauchi, N. Katase, T. Tamegai, *et al.*, Physica C (Amsterdam) **264**, 227 (1996).
39. H. Srikanth, Z. Zhai, S. Sridhar, *et al.*, J. Phys. Chem. Solids **59**, 2105 (1998).
40. A. Hosseini, S. Kamal, D. A. Bonn, *et al.*, Phys. Rev. Lett. **81**, 1298 (1998).
41. C. E. Gough and N. J. Exon, Phys. Rev. B **50**, 488 (1994).
42. I. E. Batov, Yu. A. Nefyodov, M. R. Trunin, *et al.*, unpublished.
43. M. R. Trunin, Yu. A. Nefyodov, D. V. Shovkun, *et al.*, J. Supercond. (in press).
44. H. Enríquez, N. Bontemps, A. A. Zhukov, *et al.*, Phys. Rev. B (in press).
45. H. Kitano, T. Hanaguri, and A. Maeda, Phys. Rev. B **57**, 10946 (1998).
46. M. B. Gaifullin, Y. Matsuda, N. Chikumoto, *et al.*, Phys. Rev. Lett. **83**, 3928 (1999).

Translated by V. Sakun